Efficient Electrocatalysts Based on Nitrogen-doped Carbon Nanostructures for Energy Applications

Tiva Sharifi

Department of Physics
Umeå University
Umeå 2015

This work is protected by the Swedish Copyright Legislation (Act 1960:729)
ISBN: 978-91-7601-214-7
Electronic version available at http://umu.diva-portal.org/
Printed by: Print & Media
Umeå, Sweden 2015

To Alireza

Abstact

Carbon nanostructures have emerged as a key material in nanotechnology and continuously find new areas of applications. Particularly, they are attractive due to their excellent properties as support for catalyst nanostructures leading to highly efficient composite materials for various electrochemical applications. The interest in these structures is further increased by the possibility to alter their electronic and structural properties by various methods. Heteroatom doping of carbon nanostructures is one of the approaches which may induce intrinsic catalytic activity in these materials. In addition, such introduction of guest elements into the hexagonal carbon skeleton provides strong nucleation sites which facilitate the stabilization of nanostructures on their surface. In this thesis we present detailed studies on the nitrogen incorporation into carbon nanostructures, particularly carbon nanotubes and reduced graphene oxide. Due to the high impact of nitrogen configuration on the intrinsic electrocatalytic properties of carbon nanostructures, we investigated the nitrogen functionalities using X-ray photoelectron spectroscopy and Raman spectroscopy. Based on our achievements we could assign the most electrocatalytic active nitrogen site in nitrogen-doped carbon nanotubes (NCNTs) for catalytic oxygen reduction reaction (ORR) which is an important reaction in energy conversion systems such as fuel cells. We then used nitrogen-doped carbon nanostructures as a key component to manufacture hybrid material, where the nitrogen doped nanostructures has a role of both stabilizing the nanostructures and to work as conductive additive to assist the charge transfer from the other constituents suffering from inherently poor conductivity. Our hybrid material comprising transition metal oxides (Fe_2O_3 and Co_3O_4) anchored on nitrogen-doped carbon nanostructure were used to both manufacture an exotic type of graphene nanoscrolls, as well as studied and evaluated as an electrocatalyst in various electrochemical reactions. We show that the self-assembled electrodes exhibited better performance and higher stability compared to when the same material was loaded on common current collectors such as fluorine tin oxide (FTO) coated glass and glassy carbon electrode, with both higher current densities, more efficient charge transfer and lower overpotentials for oxygen evolution and hydrogen evolution reactions, the two important processes in a water splitting device. Our NCNTs-based electrodes showed further excellent performance in lithium ion batteries with high cyclability and capacity. The thesis gives insight into processes, materials, and methods that can be utilized to manufacture an efficient water splitting device, based on earth-abundant self-assembled materials. It further represents a significant advancement of the role of nitrogen in heteroatom-doped nanostructures, both regarding their intrinsic catalytic activity, as well as their role for stabilizing nanostructures.

Sammanfattning

Kolnanostrukturer såsom grafen och kolnanorör är ett av de viktigaste materialen inom nanoteknologin och de finner ständigt nya områden för tillämpningar. En av de speciellt attraktiva egenskaperna är deras förmåga att fungera som substrat för katalytiska nanopartiklar, vilket leder till högeffektiva kompositmaterial för olika elektrokemiska tillämpningar. Möjligheten att förändra kolmaterialens egenskaper ytterligare, i synnerhet deras struktur och elektroniska egenskaper, genom olika metoder har ytterligare spätt på det stora intresset för dessa strukturer. Dopning av gästatomer i strukturerna är en metod att åstadkomma detta och i visa fall kan det inducera ”interna” katalytiska egenskaper i de dopade kolnanostrukturerna vilket innebär möjligheten att skapa metallfria katalysatorer. Förutom dessa katalytiska egenskaper, kan introduktionen av gästatomer i det hexagonala kolskelettet också ge upphov till förankringspunkter som kan stabilisera andra nanostrukturer på deras yta.

I denna avhandling presenteras en detaljerad studie av kvävedopning i kolnanostrukturer, i synnerhet av kolnanorör och reducerad grafenoxid. På grund av att de elektrokatalytiska egenskaperna är starkt beroende av typen av kvävedefekt i kolnanostrukturerna, undersöktes dessa defekter i detalj med röntgenfotoelektronspektroskopi och Raman spektroskopi. Baserat på vår studie kunde vi tillordna katalytiska egenskaper för de enskilda kvävedefekterna i dopade kolnanorör, och fastslå vilken som var mest aktiv för syrereduktion (ORR). Denna process är mycket viktig i exempelvis bränsleceller. Vi använde vidare de kvävedopade kolnanostrukturerna som en nyckelkomponent i olika hybridmaterial, med rollen att både stabilisera andra nanostrukturer, såsom nanopartiklar av järnoxid och koboltoxid, på ytan av dessa material, samt för att förbättra laddningsöverföringen från transitionsmetalloxiderna till elektroden. Våra hybridmaterial, uppbyggda av transitionsmetalloxider (Fe_2O_3 och Co_3O_4) förankrade på kvävedopade kolnanostrukturer, kunde både leda till formation av en ny typ av exotiska grafennanorullar, men studerades och utvärderades även som elektrokatalysatorer för olika elektrokemiska processer. Vi visar att hybridmaterialen uppvisar en bättre prestanda och stabilitet jämfört med när samma typ av material appliceras på vanliga strömkollektorer såsom fluortennoxid (FTO) belagt glas eller “glassy carbon”, Våra hybridmaterial ger högre strömdensitet, effektivare laddningsöverföring och lägre överpotentialer för OER (oxygen evolution reactions) och HER (hydrogen evolution reactions), vilket är de två processerna som drivs i en vattenspjälkande komponent. Våra kvävedopade kolnanorör visar vidare utmärkta egenskaper som elektroder i litiumjonbatterier, med hög cyklisk stabilitet och kapacitans. Avhandlingen ger viktig inblick och kunskap om

processer, metoder och material som kan användas för att framställa vattenspjälkande komponenter baserade av lättillgängliga material som kan tillverkas i storskaliga processer. Den innebär också ett tydligt kunskapssprång för egenskaperna hos kvävedefekterna i kvävedopade kolnanostrukturer, både vad gäller deras katalytiska egenskaper samt deras förmåga att stabilisera externt förankrade nanostrukturer.

Table of Contents

Table of Contents i
Most commonly used abbreviations iii
List of publications iv
1. Introduction 1
2. Carbon nanostructures 3
2.1. Carbon nanotubes 3
2.2. Graphene and graphene oxide 4
2.3. Nitrogen doping of carbon nanostructures 5
2.4. Synthesis of carbon nanostructures 6
2.4.1. Synthesis of pristine and doped carbon nanotubes 6
2.4.1.1. Chemical vapor deposition 6
2.4.2. Synthesis of graphene oxide, reduced graphene oxide and nitrogen-doped reduced graphene oxide 7
2.5. Hybrid materials 8
3. General aspects of Catalytic electrochemical processes 9
3.1. Oxygen reduction reaction 9
3.1.1. Kinetics of ORR 10
3.1.2. Electrocatalysts for ORR 11
3.1.3. ORR on doped carbon materials 12
3.2. Water electrolysis 12
3.2.1. Carbon based direct electrode for water electrolysis 14
3.3. Li-ion batteries 15
4. Experimental methods 18
4.1. Synthesis of pristine and nitrogen-doped carbon nanotubes by chemical vapor deposition method 18
4.2. Synthesis of hybrid graphene nanoscrolls by adsorption of γ-Fe_2O_3 (maghemite) nanoparticles 18
4.3. Synthesis of hybrid iron oxide/nitrogen-doped carbon nanotubes 19
4.4. Synthesis of bifunctional 3D electrode based on Co_3O_4/nitrogen-doped carbon nanotubes 19
5. Characterization 20
5.1. Electron microscopy 20
5.1.1. Transmission electron microscopy 20
5.1.2. Scanning electron microscopy 21
5.2. Raman spectroscopy 21
5.3. X-ray photoelectron spectroscopy 23
5.4. Thermogravometric analysis 23
5.5. Electrochemical testing 24
5.5.1. Linear sweep voltammetry 24
5.5.2. Cyclic voltammetry 25

5.5.3. Rotating disk and rotating ring disk electrode measurement 25
5.5.4. Electrochemical impedance spectroscopy 26
5.5.5. Li-ion battery test 27
6. Results and discussion 28
6.1. Pristine and nitrogen-doped carbon nanotubes 28
6.2. Nitrogen functionalities in NCNTs 28
6.3. Transformation of nitrogen functionalities in NCNTs 33
6.4. Configuration of catalytically active site in NCNTs for ORR 35
6.5. Hybrid graphene nanoscrolls by adsorption of ϒ-Fe_2O_3 (maghemite) nanoparticles 37
6.6. Advanced negative electrodes based on hybrid iron oxide/nitrogen-doped carbon nanostructures 43
6.6.1. Hierarchical NCNTs and hybrid NCNTs/hematite electrode material for LIBs 44
6.6.2. Hierarchical hybrid NCNTs/maghemite electrode material for electrochemical water oxidation 50
7. Bifunctional 3D electrode for efficient water electrolysis in alkaline medium 54
7. Conclusion and outlook 57
8. Summary of appended articles 60
9. Acknowledgements 64
10. References 66

Most commonly used abbreviations

CNT	Carbon nanotube
CP	Carbon paper
CV	Cyclic voltammetry
CVD	Chemical vapor deposition
GOx	Graphene oxide
HER	Hydrogen evolution reaction
HRTEM	High resolution transmission electron microscopy
K-L plot	Koutecky-Levich plot
LSV	Linear sweep voltammetry
MWCNT	Multi-walled carbon nanotube
NCNT	Nitrogen-doped carbon nanotube
N-rGOx	Nitrogen-doped reduced graphene oxide
OER	oxygen evolution reaction
ORR	Oxygen reduction reaction
PV	Photovoltaic
rGOx	Reduced graphene oxide
SEM	Scanning electron microscopy
SQUID	Superconducting quantum interference device
SWCNT	Single-walled carbon nanotube
TEM	Transmission electron microscopy
TGA	Thermogravimetric analysis
TMO	Transition metal oxide
XPS	X-ray photoelectron spectroscopy

List of publications

This thesis is focused on the following publications:

I. Nitrogen doped multi walled carbon nanotubes produced by CVD-correlating XPS and Raman spectroscopy for the study of nitrogen inclusion
T. Sharifi, F. Nitze, H. R. Barzegar, C.W Tai, M. Mazurkiewicz, A. Malolepszy, L. Stobinski, T. Wågberg, Carbon 2012, 50 (10), 3535-3541.

II. Formation of active sites for oxygen reduction reaction by transformation of nitrogen functionalities in nitrogen-doped carbon nanotubes
T. Sharifi, G. Hu, X. Jia, and T. Wågberg, ACS Nano 2012, 6 (10), 8904-8912.

III. Formation of nitrogen-doped graphene nanoscrolls by adsorption of magnetic γ-Fe_2O_3 nanoparticles
T. Sharifi, E. Gracia-Espino, H.R. Barzegar, X. Jia, F. Nitze, G. Hu, P. Nordblad, C.W. Tai, T. Wågberg, Nat Commun 2013, 4.

IV. Hierarchical self-assembled structures based on nitrogen-doped carbon nanotubes as advanced negative electrodes for Li-ion batteries and 3D microbatteries
T. Sharifi, M. Valvo, E. Gracia-Espino, R. Sandström, K. Edström, T. Wågberg, Journal of Power Sources 279 (2015) 581-592

V. Efficient electrochemical water oxidation by maghemite nanorods anchored on a 3D nitrogen-doped carbon electrode
T. Sharifi, W.L. Kwong, H-M Berends, C. Larsen, J. Messinger, T. Wågberg, Submitted

VI. Earth-abundant bifunctional 3D electrode for efficient water electrolysis in alkaline medium
Tiva Sharifi, Xueen Jia, Robin Sandström, Thomas Wågberg, Submitted

Other works which are not directly connected to this thesis:

i. Simple Dip-Coating Process for the Synthesis of Small Diameter Single-Walled Carbon Nanotubes-Effect of Catalyst Composition and Catalyst Particle Size on Chirality and Diameter

H.R. Barzegar, F. Nitze, **T. Sharifi**, M. Ramstedt, C.W. Tai, A. Malolepszy, L. Stobinski, T. Wågberg, J. Phys. Chem. C 2012, 116, 12232–12239

ii. Phase-transfer synthesis of amorphous palladium nanoparticle-functionalized 3D helical carbon nanofibers and its highly catalytic performance towards hydrazine oxidation
G. Hu, **T. Sharifi**, F. Nitze, H.R. Barzegar, C.W. Tai, T. Wågberg, Chemical Physics Letters 543 (2012) 96–100

iii. Palladium nanocrystals supported on helical carbon nanofibers for highly efficient electro-oxidation of formic acid, methanol and ethanol in alkaline electrolytes
G. Hu, F. Nitze, H.R. Barzegar, **T. Sharifi**, A. Mikolajczuk, C.W. Tai, A. Borodzinski, T. Wågberg, Journal of Power Sources 209 (2012) 236–242

iv. Self-assembled palladium nanocrystals on helical carbon nanofibers as enhanced electrocatalysts for electro-oxidation of small molecules
G. Hu, F. Nitze, **T. Sharifi**, H.R. Barzegar, T. Wågberg, J. Mater. Chem., 2012, 22, 8541

v. Nitrogen Doping Mechanism in Small Diameter Single-Walled Carbon Nanotubes : Impact on Electronic Properties and Growth Selectivity
H.R. Barzegar, E. Gracia-Espino, **T. Sharifi**, F. Nitze, T. Wågberg, J. Phys. Chem. C 2013, 117, 25805–25816

vi. Synthesis of Palladium/Helical Carbon Nanofiber Hybrid Nanostructures and Their Application for Hydrogen Peroxide and Glucose Detection
X. Jia, G. Hu, F. Nitze, H.R. Barzegar, **T. Sharifi**, C.W. Tai, T. Wågberg, Appl. Mater. Interfaces 2013, 5, 12017–12022

vii. Small palladium islands embedded in palladium-tungsten bimetallic nanoparticles form catalytic hotspots for oxygen reduction
G. Hu, F. Nitze, E. Gracia-Espino, J. Ma, H.R. Barzegar, **T. Sharifi**, X. Jia, A. Shchukarev, L. Lu, C. Ma, G. Yang, T. Wågberg, Nat Commun 2014, 5

viii. Reduction free room temperature synthesis of a durable and efficient Pd/ordered mesoporous carbon composite electrocatalyst for alkaline direct alcohols fuel cell

G. Hu, F. Nitze, X. Jia, **T. Sharifi**, H.R. Barzegar, E. Gracia-Espino, T. Wågberg, RSC Adv., 2014, 4, 676

1. Introduction

In order to match modern society's increasing demands of energy and concurrently limit the effects of global heating and pollution, the future energy scenario needs to be based on renewable energy sources. Hydrogen is one of the most important fuels and can be utilized for example in fuel cells. Hence, hydrogen production and storage from sustainable sources are widely considered. Utilizing green sources such as solar, wind and hydroelectric power for hydrogen production not only increases the efficiency but also reduces the price. Among many approaches, water electrolysis powered by solar energy is an attractive approach. In water electrolysis reaction, water is converted to hydrogen and oxygen *via* two half reactions by applying external energy. The process can be optimized by employing suitable electrocatalysts to overcome the chemical reaction barriers. Due to the extensive challenges involved in the development of efficient electrodes comprising photocatalysts to directly harvest the solar energy and the subsequent conversion to chemical fuels by phoelectrochemical water splitting,[1] intensive research has also been focused on photovoltaic (PV)-driven water electrolysis.[2-3] In such process the electrocatalysts can be optimized separately for oxygen evolution and hydrogen evolution half reactions (OER & HER). Finally, to provide the thermodynamic driving force of water electrolysis (1.23 eV) plus the practical overpotential, more than one conventional solar cell must be connected in series. The energy barrier to drive OER is often higher than the other in the electrochemical cell. Hence, the nature, morphology and structure of the anodic material strongly influence the rate and efficiency of the cell reaction. Different catalytic materials for this reaction have been proposed, from noble metal oxides to their alternatives such as organic materials, transition metal oxides or their composites.[4-5] Among noble metal oxides, RuO_2 and IrO_2 are accepted as the most efficient electrocatalyst for OER in alkaline condition.[6] Nevertheless, energy conversion based on these low-abundant electrocatalysts keeps the commercial systems prohibitively expensive. New technologies need to be developed for electrode fabrication with high balance of efficiency and system costs.

To achieve this, during my Ph.D. I tried to focus on developing an inexpensive, scalable, durable and efficient electrode material which can be used directly in the energy conversion process. To reduce the price, I focused on all organic carbon based materials and its combination with transition metal oxides (TMOs) such as iron oxide and cobalt oxide, which are among the most earth abundant elements. The carbon material (in the form of carbon nanotubes and reduced graphene oxide) was intentionally doped with nitrogen to increase both the intrinsic electrocatalytic activity and the nucleation sites for the formation of metal oxide nanostructures on the surface. The final electrode was fabricated by tailoring this hybrid material to the current collector. Combining the metal oxides with the carbon support not only solves their inherent conductivity problem by providing a

conductive bridge to the current collector but also inhibits the agglomeration of nanostructured metal oxides which is a common problem for nano-sized structures. This bottom-up design of the electrode was based on the knowledge we acquired during studying each component of the hybrid material separately. Specifically, formation of nitrogen functionalities and the adsorption energy of each functionality for iron oxide nanoparticles were studied in different projects. The fabricated electrodes were capable of addressing major drawbacks of commercial electrodes in different electrocatalytic reactions.

Besides studying OER and HER which are the energy consuming reactions in water electrolysis, the role of nitrogen functionalities in nitrogen doped carbon nanotubes (NCNTs) towards oxygen reduction reaction (ORR) was also studied. ORR is the most important reaction in energy converting systems such as fuel cells. In proton exchange membrane (PEM) fuel cells, ORR is the cathodic reaction which is kinetically a slow process.[7-9] NCNTs are reported to have intrinsic catalytic activity to catalyze ORR[9] but the catalyzing mechanism regarding the role of each nitrogen functionality is still a matter of debate. If NCNTs with a major portion of catalytic active site(s) are synthesized, the overall intrinsic catalytic activity of NCNTs can be further enhanced. By firmly anchoring this “green” and all organic catalyst on the surface of a substrate, the electrode could be used directly as the cathode in fuel cell.

As current collector for our electrodes, we have chosen a low cost, conductive carbon substrate. Carbon paper (CP) is capable of up-scaling with a large surface area and by synthesizing NCNTs that are firmly attached to the fibers of carbon paper, we can further enhance both the surface area as well as significantly reduce the charge transport resistance from NCNTs to the current collector (CP).

Additionally, considering the growing power-supply requirements, we have also tested our hybrid material for rechargeable lithium-ion batteries which are key devices for electricity storage. Since the main challenges in this field, beside achieving high capacity and optimum cycling performance,[10] is electrode fabrication, our binder free direct electrodes comprising only NCNTs or hybrid NCNTs/iron oxide, tightly attached to CP current collector, meet these requirements to a high extent.

In the following, I will give a brief introduction to the different materials that I have used and synthesized in my work (chapter 2), the theoretical aspects of different catalytic electrochemical processes (chapter 3), the techniques that I have used to characterize our material (chapter 4), the methods to synthesize them (chapter 5) and then the detailed achievements are presented in chapter 6.

2. Carbon nanostructures

In the mid-1980s Smalley and co-workers[11] discovered fullerenes (C_{60}) which are molecules composed of only carbon atoms with hexagonal and pentagonal faces. C_{60} resembles a football composed of twenty hexagons and twelve pentagons. The study of fullerenes led to the discovery of a new structure by Iijima in 1991 today known as carbon nanotubes.[12] Nanotubes are divided into two main types, single walled carbon nanotubes (SWCNTs) and multi walled carbon nanotubes (MWCNTs). A SWCNT can be visualized by rolling a graphene sheet up into a cylinder in such a way that the thickness of the cylinder wall is only one carbon atom. A MWCNT is a collection of concentric cylinders like a Russian doll. The circumference of the inner cylinder has usually a small number of carbon atoms (10-40). The length along the axis is usually of the order of microns and can be up to millimetres.[13-14] Bamboo structured CNTs are a sub type of MWCNTs which are made of several cones of graphene sheets on top of each other.[15] Helical CNTs[16] and helical nano fibres[17] are some other interesting graphitic based nanostructures (see figure 1). More recently, graphene has joined the carbon nanostructure family, having a similar graphitic based structure.[18] Although the idea to isolate a single graphite layer (corresponding to a graphene layer) has existed for long time, graphene is the youngest member in the carbon allotrope family, being successfully isolated first in 2004.[19] The extraordinary physical properties of carbon nanostructures such as high strength, unique electrical properties and high conductivity have raised large interest on this group of material.

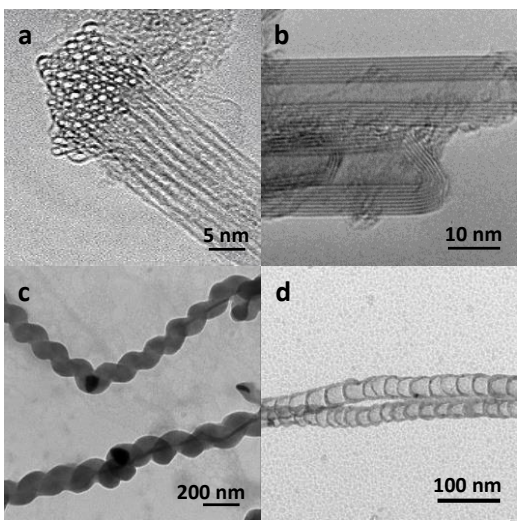

Figure 1. TEM images of a) single-walled, b) multi-walled, c) helical and d) bamboo structured CNTs

2.1. Carbon nanotubes

When describing CNTs, it is important to understand the atomic structure of nanotubes by looking at an opened graphitic sheet. A SWCNT is defined in regard to its chirality, or helicity. The chirality is defined by the chiral vector

and its angle, c_h and θ respectively according to:[20]

$$C_h = na_1 + na_2 \equiv (n, m) \qquad (1)$$

where a_1 and a_2 are unit vectors of the carbon honeycomb lattice (corresponding to a graphene sheet). The two indices, n and m indicate the number of unit vectors. The tube may be twisted with respect to the a_1 direction with the angle θ as shown in figure 2. Depending on the value of θ, so called zigzag (θ=0°), armchair (θ=30°) and chiral (0°<θ<30°) tubes can be defined. In the family of carbon nanostructures, MWCNTs are of special interest for the industry due to the possibility to scale up their production, while keeping their attractive properties. It consists of rolled-up multiple layers of graphite forming tubular shape. Since MWCNTs consist of a number of concentric SWCNTs, the chirality cannot be defined.

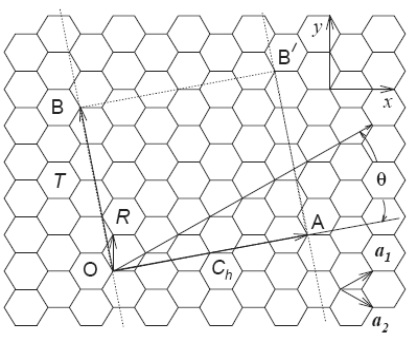

Figure 2. The unrolled honeycomb of a (2, 4) single walled

2.2. Graphene and graphene oxide

The carbon atoms in graphene form a honeycomb lattice due to their sp^2 hybridization. It can be visualized as a single atomic layer of graphite. A large scale synthesis of single layer graphene is challenging and hence fabrication of few layer graphene which ideally exhibit the extraordinary properties of single layer graphene to a high extent has been considered.[21-22]

Graphene oxide (GO_x) is a defective 2D graphite-based material resembling few layer graphene[23] which forms by oxidizing and exfoliating graphite. Formation of C-O bonds mainly causes the exfoliation of graphite and concurrently introduces defects in the structure of graphene oxide. Due to the ability of GO_x to remain as single sheet with high dispersability in water, it is widely used in thin film technologies. GO_x can be reduced to form a similar structure that are relatively similar to graphene but which contains more defects, leading to a conductivity that are at best one tenth of ideal graphene.[24-25] Nevertheless it has been frequently used in electronic and composite applications. The formation mechanism[26] and electronic properties[27] of GO_x have been well studied and the reduced form of GO_x (rGO_x) is considered as an alternative for graphene in large scale applications.[28-29]

2.3. Nitrogen doping of carbon nanostructures

The performance of carbon nanostructures can be improved by altering their physio-chemical properties. Particularly, doping of CNTs and rGO_x can extend their intrinsic properties to enable their use in electronic devices[30] or as catalyst support materials.[31-33] One efficient method to adjust the physio-chemical properties is to introduce heteroatoms such as nitrogen into the carbon structure.[34-35] This alters the local electron density in these materials, and can thereby lead to significant modifications of the material properties. Depending on the technique, the precursor, and the synthesis conditions, various amounts and types of nitrogen functionalities are achieved in the final material.[36-38] Nitrogen can be present in CNTs and rGO_x in different forms based upon the neighbouring environment including the replacement of carbon by nitrogen in either a 6-membered ring or a defective 5-membered ring, in the bulk or at the edge of the graphitic structure as shown in figure 3. There are three well-known nitrogen functionalities in the graphitic carbon framework.[39-40] Pyridinic-N (shown by blue in figure 3) replaces a carbon in a 6-membered ring at the edge of a vacancy in the structure. Pyridinic-N contributes one p-electron to the aromatic π-system while having a lone electron pair. Pyrrolic-N refers to the nitrogen which shares two p-electron to the π-system and hence it can replace a carbon in a 5-membered ring or a carbon bonded to hydrogen in a 6-membered ring at the edge of a vacancy (shown by green in figure 3). Graphitic-N is a member of the quaternary nitrogen (N-Q) group. Graphitic-N forms when nitrogen replaces a carbon in the bulk of the graphitic framework (black in figure 3). The configuration of other member(s) of N-Q is still under investigation.

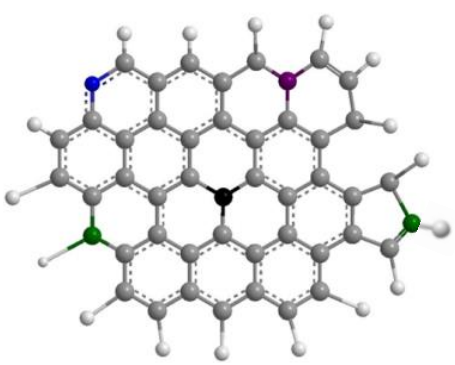

Figure 3. nitrogen functionalities localized in different sites of graphitic carbon framework

Our detailed study on the precise assignment of the members of this group based on X-ray photoelectron spectroscopy (XPS) is presented in paper II and will be described later in results section. Understanding the properties of different nitrogen functionalities is of great interest due to dissimilar behaviour of each functionality regarding electrocatalytic activity, and chemical stability. The main obstacle to study these issues is the difficulty in recognizing the accurate location of the nitrogen in the carbon framework. A vast effort has focused on the recognition of nitrogen substitution mechanism[41] for further understanding the role of substituted nitrogen in real use.[42]

2.4. Synthesis of carbon nanostructures

Due to the rapid development of carbon based materials since 1980s, several different techniques have been employed to synthesize the featured morphology of these structures. The synthesis strategies include chemical vapour deposition (CVD), sol-gel process, pyrolysis, self-assembly processes and many other techniques.[43] Here I focus on the synthesis of carbon nanotubes and reduced graphene oxide which are widely used throughout the thesis.

2.4.1. Synthesis of pristine and doped carbon nanotubes

There are three well developed methods to synthesize CNTs; arc discharge, laser ablation and chemical vapour deposition (CVD). Despite that the synthesis principle in all the mentioned methods are rather similar, the appearance and purity of the resulting material may differ. The arc-discharge method was one of the earliest developed methods to initially produce C_{60}s, but it has later been widely used to synthesize CNTs as well. The advantage with this method is that it can produce large amounts of highly crystalline CNTs, but since it usually results in a number of different complexes a further purifying step is usually needed.[44] Laser ablation method is a commonly used method having a different source of energy (dual-pulsed laser) and the product has much higher purity compared to arc discharge method.[45] CVD method is another widely used method with the potential to produce bulk amounts of high quality CNTs. Due to the slightly lower synthesis temperature than in the two former methods, the level of impurities is lower but the product is more defective.

2.4.1.1. Chemical vapour deposition

The principle of the chemical vapour deposition (CVD) process involves a thermal and/or catalytic decomposition of hydrocarbon over a solid substrate in the presence of a catalyst. There is a generally accepted formation model for catalytic growth of CNTs. This model can be summarized in three steps; (1) adsorption and decomposition of hydrocarbon gases, (2) diffusion of released carbon atoms in or over the catalyst particle and (3) precipitation of the graphitic-like layers.[46-47] The growth of CNTs can be either base or tip growth. In former the tube forms in a way that the catalyst particles remain in the base of tubes and in the latter the catalyst particles are encapsulated in tips of the tubes. Two different categories of CVD can be distinguished, (1) those involving pre-deposited catalyst films or particles on a support substrate (figure 4a) and (2) those utilizing in-situ decomposition of catalyst and carbon precursors (figure 4b).

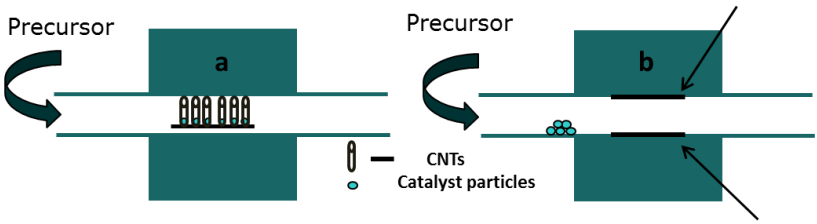

Figure 4. schematic of chemical vapour deposition (CVD) system

In the first category, catalyst particles or a film of catalyst material (*e.g.* iron, nickel, cobalt or a mixture of metals) is deposited on the surface of the substrate with a defined thickness and pattern by various methods such as thermal or electron beam evaporation, sputtering and lithography.
In the second category, the catalyst precursor-in powder form-are brought to its decomposition temperature and enters the reaction chamber along with the carbon precursor. It is possible also to inject a solution of carbon precursor and a metal composite (*e.g.* ferrocene) directly into the reactor. The metal composite decomposes and the released metal atoms agglomerate into particles which can then act as catalyst.

Diffusion of dissociated carbon in or over the catalyst particles is considered as a probable rate determining step in the growth process of CNTs. This highlights the importance of the catalyst material which has a direct impact on the final product. It can influence not only the morphology of the growth product but also the growth rate and hence the length and purity of the CNTs.[48] Catalyst particles with sizes larger than 3 nm are usually reported to result in the growth of MWCNTs, while smaller particles lead to SWCNTs growth.[49-50] Mixed and particularly bimetallic compounds are shown to significantly enhance the CNT growth.[51]

Nitrogen can be incorporated into the structure of CNTs either during the growth or by post synthesis modification with nitrogen-containing organic molecules.[52] In the most reliable approach, nitrogen-containing precursor is used and nitrogen might become incorporated into the graphitic lattices during the growth.[53]

2.4.2. Synthesis of graphene oxide, reduced graphene oxide and nitrogen-doped reduced graphene oxide

Single and few layer graphene were first synthesized by mechanical exfoliation of graphite.[19] Even though the synthesized graphene is pure it is not suitable for large-scale manufacturing. Instead exfoliated sheets of rGO_x are considered as an alternative for graphene where large scale quantities are more imperative than the supreme morphology and conductivity of graphene. This is especially relevant for energy storage applications. Chemical routes are among the best approaches for bulk production of

graphene material.[54] To date, chemical efforts to exfoliate graphite have focused on oxidizing graphite by strong acids and then exfoliate them by either thermal or ultrasonic methods.[55-57] The most common method to synthesize GO_x is the Hummer's method[58] which is usually modified to fit the demands of the experiment. GO_x which is the product of oxidizing graphite is a non-conductive hydrophilic carbon based material. The interlayer spacing of the lattice is increased from 0.335 nm for graphite to 0.625 nm for GO_x.[59] One of the strongest advantages of the GO_x is its water dispersability[60] which extends the possibility to apply graphene oxide in many different areas. The produced GO_x can be reduced further to form rGO_x[61-62] with a conductivity and carrier mobility which lag behind graphene [27] but still good enough to be used widely.

Similar to CNTs, the properties of graphene (and rGO_x) can be altered and modified by introducing guest heteroatoms such as nitrogen into its structure. To synthesize nitrogen-doped rGO_x (N-rGO_x), GO_x is usually mixed and annealed with a nitrogen-containing precursor before the reduction step. The material is then reduced and doped simultaneously in a reduction step similar to the reduction step to form pristine rGO_x.[63] Another approach is to use a nitrogen containing reducing agent such as hydrazine instead, which usually results in a lower nitrogen doping level.[64-65]

2.5. Hybrid materials

Carbon nanostructures (CNS) possess large surface area, high conductivity and long charge transport capability. Hence, they have been widely considered as building blocks in the design of hybrid materials. When added to form hybrid material, apart from contributing by their own intrinsic properties they can also modify the shortcomings of the other components of the respective hybrid material. When mixed with metal oxide for instance, they can be considered as a conductive additive which makes up for the poor conductivity of metal oxides[66-67] and concurrently are capable of hindering the large agglomeration affinity of metal oxide nanoparticles. Due to this, CNS-based hybrid materials are merging quickly to the field of electrode fabrication.[68-71] Although nowadays CNTs, graphene and their mixture are the most common materials as the carbon component of CNS-based hybrid materials[68, 72-76] other CNSs such as Vulcan,[77] carbon onion[78] and nanoporous carbon[79] are employed extensively as well.

3. General aspects of the catalytic electrochemical processes

3.1. Oxygen reduction reaction

Oxygen is the third most abundant element on earth, and is vital to all living organisms. Furthermore, the so called oxygen reduction reaction (ORR) is an important reaction for energy conversion in both technical applications as well as in biological respiration (schematically shown in figure 5). Recently, its essential role in fuel cells and lithium-air batteries has attracted researchers to understand the mechanism of this reaction.

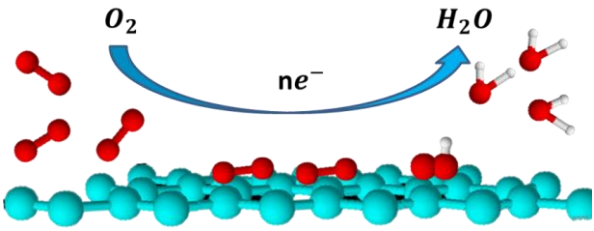

Figure 5. Schematic of ORR on the surface of the material

ORR is a complex electrochemical reaction that involves breaking a double O-O bond and formation of O-H bonds *via* several steps producing intermediate species. The number of electron transfer in the step that precedes the O-O bond breaking defines the mechanism of ORR. Despite significant theoretical and experimental efforts, the exact mechanism of the reaction is unclear. This arises from the shortcomings of our devices to detect reaction intermediates as well as the high overpotential needed to drive this reaction which limits the study of electron transfer mechanism.[80] There are two accepted pathways for ORR based on the electron transfer number. In the direct 4-electron pathway four electrons are involved in the reduction of O_2 to H_2O, while in 2-electron pathway H_2O_2 is formed as an intermediate step.[81] The pathway is depending on the electrolyte condition and the nature of electrode catalyst material. A summary of electrochemical ORR is given in table 1 which is categorized based on the type of electrolyte.
Depending on the application, different processes have their unique significance. In fuel cells for instance, 4-electron process is highly preferred due to absence of the intermediate step in which hydrogen peroxide (H_2O_2) is produced. On the other hand, it is obvious that in the hydrogen peroxide industry the 2-electron process is favored.

Table 1. A summary of electrochemical ORR categorized based on the condition of electrolyte

Electrolyte	ORR
Acidic aqueous solution	$O_2 + 4(H^+ + e^-) \rightarrow 2H_2O$
	$O_2 + 2(H^+ + e^-) \rightarrow H_2O_2$ $H_2O_2 + 2(H^+ + e^-) \rightarrow 2H_2O$
Alkaline aqueous solution	$O_2 + H_2O + 4e^- \rightarrow 4OH^-$
	$O_2 + H_2O + 2e^- \rightarrow HO_2^- + OH^-$ $HO_2^- + H_2O + 2e^- \rightarrow 3OH^-$

3.1.1. Kinetics of ORR

For ORR it is desirable that it proceeds at a potential satisfactorily close to the reversible electrode potential (1.23 V). In addition, rate of reaction should be high enough to achieve an optimum efficiency. According to Butler-Volmer equation (eq. 2), the electrical current on both cathode and anode is related to the electrode potential as follows:

$$j = j_0 \left[\exp(\frac{n\alpha_a F\eta}{RT}) - \exp(-\frac{n\alpha_c F\eta}{RT})\right] \qquad (2)$$

Where j is the electrochemical current density, j_0 is the exchange current density, n is the electron transfer number in the rate determining step, α_a and α_c are anodic and cathodic transfer coefficient, F is faraday constant, R is the gas constant and η is called the overpotential of the reaction. The overpotential is the potential difference between the theoretically determined thermodynamic reaction potential and the potential at which the reaction proceed experimentally. Exchange current density is the current density measured when no electrochemical reaction occur or the current density measured at zero overpotential. It represents the electrochemical reaction rate in equilibrium. The magnitude of the exchange current density shows how fast the electrochemical reaction proceeds. The electrode material has strong effect on the rate of reaction. So by means of a careful choice of electrode material (with the help of a suitable catalyst for example) we can direct the electrochemical process to proceed faster and we see this effect by calculating the exchange current density. If we consider the reaction going in anodic direction then eq. 2 reduces to:

$$j = j_0 \exp\left(\frac{n\alpha_a F\eta}{RT}\right) \qquad (3)$$

The linear region in the plot of η *vs*. log j (Tafel plot) has the slope of $\frac{2.303RT}{\alpha_a nF}$ which is called the Tafel slope. From the Tafel plot one can describe the kinetics of the electrochemical reaction. One of the methods to calculate the electron transfer number is by solving the Tafel slope. The major difficulty then is to find the reaction coefficient α which is determined experimentally and can have different values based on the material and experimental condition.[82-83] Due to this unambiguity, the electron transfer number calculated by this method is not accurate enough. The other method, which is more accurate, is to use rotating disk electrodes which will be explained later.

The Tafel slope is directly related to the rate of reaction, meaning that slower reactions (rate determining step) exhibit smaller Tafel slopes. The slow, sluggish kinetics of ORR is indeed a severe limitation which constrains the performance and efficiency of practical applications. Due to this, efficient electrocatalyst materials are utilized and "thought-out" to improve the kinetics of the reaction. While under acidic electrolyte platinum-based (Pt-based) electrocatalysts are the main materials, in alkaline condition non-noble elements and particularly their oxides are widely used.[47, 84] Due to the high performance of Pt as an electrocatalyst for ORR *via* a 4-electron process, it has historically been frequently used in commercial systems. However, due to the very large cost correlated to its low abundance in earth's crust the identification of alternative materials for Pt (and other noble metal catalysts) is essential. Both metal free all organic materials and transition metals (and specially their oxides, TMOs) are among the best and promising candidates.[9, 85-87]

3.1.2. Electrocatalysts for ORR

To simultaneously reduce the cost and increase the efficiency of the systems where ORR is involved, three approaches are being pursued: i) reducing the Pt loading, ii) development of metal-free or all organic catalysts and iii) considering non-noble metals as alternative catalyst. A common and successful strategy to decrease the Pt loading is to use nanostructure/ particles of Pt which are usually loaded on a carbon support forming a hybrid material.[88-89] Another approach to reduce the Pt-loading is by forming alloys of Pt with a non-noble metal,[90-91] core shell structures[92-93] and Pt islands.[94] Metal-free electrocatalysts usually consist of carbon materials which in most of cases are doped with selected elements such as N, B, P and S.[95-96] This type of material has shown promising ORR activity, high stability and higher tolerance for CO poisoning compared to Pt/C.[97-100] The last approach is using non-noble metal electrocatalyst instead of Pt. Even though these materials have shown a better tolerance to fuel poisoning compared to Pt, the

electrocatalytic activity is in most cases substantially lower than that of Pt catalyst.[101-104]

While all these approaches are being considered widely and have been discussed in many studies by our group, I will explain more in detail the ORR mechanism on doped carbon material which has been one of the main subjects of my thesis.

3.1.3. ORR on doped carbon materials

Doped carbon materials are heterogeneous materials containing carbon and a guest element such as nitrogen, boron or phosphorous. In the recent years, nitrogen doping of CNTs and graphene has attracted a great interest due to their excellent performance in different electrocatalytic reactions as an all organic catalyst.[100, 105-108] Owing its extra electron in the delocalized π-orbital of carbon framework, nitrogen is a beneficial defect in the structure of carbon material. Even though the surface adsorption of oxygen molecules is an accepted starting point of ORR, the exact mechanism and the role of nitrogen in this process is still a matter of debate. As mentioned briefly in chapter 2.3, the nitrogen can localize differently in the carbon framework depending on the experimental conditions. It is interesting to note that there are controversial studies on the active site for ORR on nitrogen-doped carbon materials, in particular on the type of nitrogen functionality which displays the highest activity towards oxygen reduction.[109-112] The main problem regarding these studies is the difficulty to characterize and identify the actual type of nitrogen functionality itself. Mismatching nitrogen functionalities leads to wrong conclusion about the electrocatalytic efficiency of the active sites. In addition, it is believed that other properties such as amount of carbon edge sites, total nitrogen content, the surface area, and presence of metallic nanoparticles also can affect the activity of the material towards ORR. By nitrogen inclusion in the carbon framework, the oxygen adsorption energy on the carbon adjacent to nitrogen reduces.[109] The adsorption energy is dissimilar for carbons sitting next to different nitrogen functionalities. In addition, in the special case of graphene and graphite it is believed that the ORR activity differ on the basal plane in comparison to the edge plane.[113-114]

3.2. Water electrolysis

Production of oxygen and hydrogen gases from electrolysis of water is a well-known principle. When a certain potential difference between electrodes is reached, hydrogen gas starts to evolve at the negatively biased electrode (cathode) and oxygen at the positively biased electrode (anode). The following reactions occur on electrodes in neutral water:

$$2H_2O \rightarrow 4H^+ + O_2 + 4e^- \qquad (9)$$

$$2H_2O + 2e^- \rightarrow H_2 + 2OH^- \quad (10)$$

The reactions are slightly different in acidic and basic water. The overall water electrolysis reaction is as follows:

$$2H_2O \rightarrow O_2 + 2H_2 \quad (11)$$

The open cell voltage for the water electrolysis is 1.23 V in standard condition which is the minimum energy needed for this reaction to evolve. However, for the reaction to get started some activation energy should be overcome. The activation energy can be reduced by using catalyst on the surface of the electrode or the electrodes with electrocatalytic activity such as Pt.

The life on earth is maintained upon conversion of solar energy to chemical energy by photosynthesis which is carried out by plants and bacteria.[115] In a similar way as mentioned above, the sunlight (and water and carbon dioxide) is converted to oxygen and protons. However, instead of forming hydrogen, the plants are using the hydrogen for carbon chemistry to build organic building materials and fuel. The water electrolysis in photosystem II is catalyzed by $CaMn_4O_x$ containing cluster with high turnover frequency at low overpotential.[116-117] Huge efforts have been directed to mimic the natural photosynthesis artificially with high efficiency as a feasible alternative to store the solar energy as fuel. Natural biological systems are however difficult to reproduce and use under normal lab operating conditions, and even more difficult to implement in a commercial device. Efficient and scalable photoelectrochemical water splitting systems requires innovations considering several important criteria. Light absorption should be managed simultaneously with the photogenerated carrier collection. Concurrently, as the catalyst material needs to be a good light absorber it also should be sustainable in the water electrolysis reaction.

In addition, ion transport and gas collection need to be considered and hence extensive efforts are required to design such a cell. Despite intensive efforts to develop efficient photoelectrodes and devices for solar hydrogen generation,[1, 118-122] it is still a challenge regarding to both the cost and efficiency. Recently, the powering of electrochemical water electrolysis reaction by photovoltaic (PV) devices has been suggested as a solution to address the problems related to photoelectrochemical devices[123]. In such systems the solar to fuel conversion are achieved by connecting two suitable electrocatalyst loaded electrodes to a PV material. The four electron process of water oxidation to oxygen, the so called oxygen evolution reaction (OER) and two electron process of hydrogen evolution reaction (HER) are then carried out separately on the anode and the cathode. In this category of devices the photovoltaic cell can be varied independent of the catalyst

material,[1, 3] and vice versa the OER and HER catalyst can be optimized separately to drive the water splitting reaction efficiently. As mentioned earlier, a minimum voltage of 1.23 V is needed to drive the water splitting but practically larger voltage is required. Commercial electrocatalysts operate at around 1.8 to 2 V.[124] Since it is difficult to achieve a single PV cell with such high open voltage, the electrolysis is often driven by tandem PV cells. Multi-junction solar cells such as triple junction silicon, III-V-based and CIGS as well as perovskite solar cells have been successfully used to drive the electrochemical splitting of water.[2, 125-127] Since the OER on anode causes the major energy loss, the kinetic and mechanism of electro-oxidation of water to oxygen have been studied widely.[128-129]

Even though noble metals such as Pt, Ru, Ir and their oxides (RuO_2 and IrO_2) catalyze OER efficiently, their high cost and low abundance have obstructed their use in commercial applications.[6, 130-131] As an alternative, TMOs containing highly oxidized redox couples such as $Co^{3+/4+}$, $Ni^{3+/4+}$, $Fe^{3+/4+}$ have shown great potential as earth-abundant and low cost catalysts for OER.[132-135] Increasing the surface area by nanostructuring and tailoring composite materials to increase synergy effects are important approaches to reduce the overpotential and hence optimize the efficiency. Stabilizing nanostructured TMOs on carbon provides a conductive support to transport the produced electrons efficiently and enhances the durability of the electrode performance.[79, 136] In a water electrolysis device, the overall water splitting reactions (OER and HER) should be utilized in the same electrolyte. This is a great challenge in electrocatalyst development due to activity of earth-abundant catalysts in different electrolytes. For instance, while MoS_2 exhibit high activity as HER electrocatalyst in acidic condition, it is not active in alkaline electrolytes. TMOs on the other hand are highly active for catalyzing OER in alkaline condition. Hence, acquiring a bifunctional electrocatalyst with high activity for HER and OER in the same electrolyte is an important step toward the development of a photo-electrochemical water splitting device.

3.2.1. Carbon based direct electrode for water electrolysis

Apart from the catalytic properties of the electrocatalyst material itself, the electrode fabrication is also a crucial step. A high performance of catalyst is essential to reduce overpotential, increase the kinetics of reaction and hence improving the energy efficiency but often the practical activity is limited by issues related to assemble the catalyst materials into a working electrode. For commercial use, such issues are sometimes even more important than the catalyst material synthesis. Most of the reported electrodes for water splitting are fabricated by depositing a thin film or an agglomerate of catalyst particles (noble metal, transition metal oxide or non-metal catalyst) on a glassy carbon, Ni foam, fluorine tin oxide (FTO) coated glass or any other

conductive substrate.[137-140] However, the electrode preparation in this way is both time consuming and difficult to control. Also, scientifically the measured activities are difficult to compare due to in homogeneities in morphology. Electrodes prepared in such ways usually also suffer from limited durability since the coated material easily peels off during the evolution of gases. To overcome such problems the use of additives and binders are common, but these add "dead weight" to the system and limit a good conduction between the active catalyst material and the conductive substrate. Recently a new generation of electrode materials has been considered in which the active material is grown directly on the surface of the current collector.[141-144] This type of electrode is beneficial in water electrolysis cells because the firm attachment of the electrocatalyst to the surface of the current collector enhances the stability of the electrode during evolution of gaseous oxygen and hydrogen and also allows for up-scaling.

To address the poor conductivity of the TMOs, hybrid materials based on carbon/TMOs are suggested, and significant improvement in the electrode properties for OER has been achieved by anchoring nanostructured metal oxides such as Co_3O_4 or iron oxide on carbon materials such as mesoporous carbon,[145] graphene[146-147] and carbon nanotubes.[74, 148] By proper choice of conductive carbon support also synergistic effects which raise the overall catalytic efficiency of the system can be gained. For example nitrogen-doped carbon nanomaterials have shown intrinsic catalytic activity for OER[140, 149-150] and the combination of nitrogen-doped carbon structures with catalytically active TMO structures has shown to give rise to interesting synergy effects.[146] Thus the growth of NCNTs on a conductive substrate and the anchoring of nanostructured metal oxides on the surface of the grown NCNTs opens up for a hybrid material that can be tailored directly as an electrode in a bottom-up process.

The above stated approach is discussed in paper IV, V and VI. We have investigated the anchoring of the active catalyst materials to NCNTs and the beneficial effect in the electrocatalytic performance of the electrode have been studied in detail.

3.3. Lithium-ion batteries

Despite of the impressive progress in harvesting sustainable energy in recent years, the development of efficient storage devices are still lagging far behind. The design and development of systems being able to store the produced energy in an environmentally sound process, which still allows for long cycling life, and high stability is an imperative challenge for researchers in materials science and electrochemistry. Lithium ion batteries (LIBs) represent one of the most promising systems to achieve a good energy density and cycling life.[10] Commercial LIBs consist of layered structure of graphite as the anode material and lithiated metal oxides (Li_xMO_2 such as

$LiCoO_2$) as the cathode material. Nowadays, Graphite-$LiCoO_2$ based LIBs power most of the portable devices. A basic scheme of LIB cell is illustrated in figure 6.

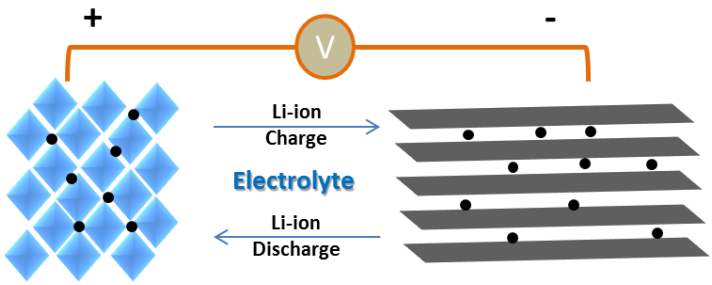

Figure 6. Schematic illustration of charge and discharge in a lithium ion battery

The source of lithium in these cells is the cathode material which is a lithium metal oxide with a higher level of safety compared to the previously used bare lithium metal. The practical use of a battery involves several key steps; the first step is the charging process which is the oxidation (and hence delithiation) of the lithium metal oxide. The lithium ions then transfer to the anode *via* an ion conductive electrolyte and lithiate the anode material. During the initial cycling, an electrically insulating, but ionically conducting layer forms on the surface of electrode. This layer is known as the solid electrolyte interphase (SEI). SEI acts as a protective layer which does not interrupt the battery function during charge/discharge cycling. For graphite the reaction with lithium can reach the stage of LiC_6 formation according to the following reaction:

$$C_6 + Li^+ + e^- \leftrightarrow LiC_6 \qquad (12)$$

This reaction on the electrode gives a theoretical specific capacity of ~372 $mAhg^{-1}$.[151] If higher-capacity anode materials with lower volumetric changes (due to Li diffusion) replace the graphite, the specific capacity and energy of LIBs can be improved. Enormous efforts focus on the innovation and synthesis of new generation anode material to achieve more efficient LIBs with lower cost and improved cycling ability.[152-153] TMOs are proved to undergo reversible conversion reaction in the presence of Li-ions,[154] and by using TMOs such as CoO, CuO and Fe_2O_3 as anode material a capacity 2-3 times higher than in graphite (600-1000 $mAhg^{-1}$) can be achieved. However the main trade-off for these materials is the extreme expansion/contraction caused by ion insertion/withdrawing. This limits the lifetime of the electrodes due to crack formation or pulverization.[155-156] Other drawbacks are rather poor reaction kinetics and large hysteresis of charge/discharge voltage due to the high energy to break M-O bonds, Nevertheless, TMOs remain as

promising anode materials because of their high charge storage capacity. The challenge lies in how to properly design hybrid composites which addresses the mentioned issues. One of the strategies which have been suggested to increase the cycling ability of the anode material is size confinement which aims to reduce the path length of charge carriers, increase the surface area, facilitate the Li insertion and hence inhibit the electrode disintegration. However, as discussed previously agglomeration is a major problem for nanoparticles and nanostructures. Here, special architecture based on nanotubes and nanowires have proven to be more stable than nanoparticles, and if vertically grown on the current collector, the three dimensional (3D) electrode facilitates the charge transport more efficiently. In such a structure the energy density raises due to the direct wiring of the active material to the current collector. In this manner, utilizing the binders and additives can be avoided and the electrode fabrication turns out to be easier and scalable.

The excellent properties of carbon based materials such as graphene, CNTs, and carbon fibers as conducting support for Li-storage materials are further strengthened by their intrinsic capacity for Li-storage. Reversible charge capacity of 540 $mAhg^{-1}$ has been reported for graphene,[157] and recently, NCNTs have attracted attention as an alternative material to graphite, due to their unique Li storage properties. The presence of nitrogen atoms form extrinsic defects that act as preferential adsorption sites for Li^+ ions, thus increasing the capacity.[158-159] Li-ions are also able to penetrate the defective tube walls and can be stored progressively in the inter-wall regions.[160] The spaces between the tube walls are thus available for Li insertion, enabling the use of their inner interfacial areas, which previously were not accessible.

On the other hand as mentioned before, nitrogen defects on the carbon material create sites that can interact better with metallic nanoparticles providing nucleation sites to stabilize the nanoparticles.[161-162] Accordingly, a combined hybrid material based on TMOs/C is an excellent material to be used as anode material in LIBs. Nitrogen doped CNTs/graphene improve the electrochemical properties of nanostructured TMOs such as iron oxide. A detailed LIBs cycling performance study on the combined effect of nitrogen doping of CNTs having iron oxide (hematite) anchored to this carbon support is presented in paper IV. Fe_2O_3 undergoes a reversible conversion reaction which involves the formation of Fe nanoparticles embedded in a Li_2O matrix:[154]

$$Fe_2O_3 + 6Li^+ + 6e^- \leftrightarrow 3Li_2O + 2Fe \qquad (13)$$

This electrode assembly addresses the short carrier diffusion length, the interfacial resistance and thereby improves the capacity retention at high cycling rates.[163-164]

4. Experimental methods

4.1. Synthesis of pristine and nitrogen-doped carbon nanotubes by chemical vapour deposition method

Depending on the necessity of having tubes which are grown vertically aligned on the substrate or in the powder form, either regular CVD or floating catalyst CVD method (FCCVD) was used. In the regular CVD a layer of the catalyst metal (Fe or Fe/Co) was thermally evaporated on the substrate (silicon wafer or carbon paper). The growth temperature was set to 700-800 °C and ammonia pre-treatment was done prior to growth. It is believed that the ammonia treatment helps the catalyst nanoparticle formation and enhances the growth condition.[165] We observed that without this step, growth was limited for Si substrate and completely inhibited in the case of carbon paper (CP) substrate. The precursor was introduced in combination with varigon™ as carrier gas. Except in one of the early projects, pyridine was injected into the reaction chamber using a syringe.

Addition of a buffer layer underneath the catalyst layer is beneficial to grow a denser forest of NCNTs on Si substrate and for the carbon substrates (CP) a buffer layer was crucial[166-167] since otherwise the catalyst diffuse into the carbon , and do not contribute to the growth of CNTs. We used titanium (Ti) as the buffer material in accordance with the previous reports.[168-169] 10 nm of Ti buffer layer was evaporated on the substrate prior to deposition of catalyst layer. In our second approach when NCNTs in powder form was desired, we utilized a FCCVD process. In this approach the catalyst precursor (ferrocene in our case) was placed at the entrance of the reaction chamber just outside of the hot zone of the oven. The temperature of this part reached to the decomposition temperature of ferrocene when the temperature in the growth zone reached the set temperature. In this way, the Fe particles meet the carbon atoms in vapour phase. After growth, the resulting tubes could be scratched and collected from the inner part of the reaction chamber.

4.2. Synthesis of hybrid graphene nanoscrolls by adsorption of γ-Fe_2O_3 (maghemite) nanoparticles

The synthesis of N-rGO_x was started by first synthesis of graphene oxide (GO_x) by a modified Hummers' method[170]. Then GO_x was dispersed in mili-Q water by ultrasonication and then melamine ($C_3H_6N_6$) was added to the suspension. When the agglomeration was observed, the dispersion was dried slowly at 80 °C in air. The resulted solid material was finely grinded using a mortar. The GO_x–melamine complex was pyrolysed at 750 °C for 45 min under an Ar atmosphere to obtain N-rGO_x. In the next step, the N-rGO_x nanoscrolls were synthesized by adding iron(III) chloride ($FeCl_3$), tungsten hexacarbonyl ($W(CO)_6$), polyvinylpyrrolidone (PVP) and hydrazine (N_2H_4) into a N-rGO_x/methanol dispersion, followed by heating under reflux for 24 h. The self-assembly formation of either maghemite or hematite

nanoparticles on N-rGO$_x$ was achieved by slight variation in the solution condition. While using a pure methanol solution led to the formation of maghemite nanoparticles, replacing a part of the methanol by water in 1:1 ratio (volume ratio) resulted in the formation of hematite nanoparticles.

4.3. Synthesis of hybrid iron oxide/nitrogen-doped carbon nanotubes

NCNTs were grown on a conductive carbon paper by CVD method. The growth process was the same as described in section 4.1, where carbon paper (CP-SIGRACET®GDL 10AA from Ion power, GmbH) with the resistivity below 15 mΩcm was used as substrate. The resulting material which we call NCNTs/CP was kept for further testing. A piece of material was used in the next step in which iron hydroxide nanorods were grown on NCNTs in a hydrothermal process. For that, a solution of iron trichloride hexahydrate ($FeCl_3.6H_2O$-0.15 mol/l) and sodium nitrate ($NaNO_3$-1 mol/l) in a mixture of deionized water/methanol (1:1) was prepared and poured into a 30 ml autoclave. A piece of NCNTs/CP was placed vertically in the autoclave and maintained at 80 °C for 18 h. The last crucial step defined the phase of iron oxide in the final product. By thermal annealing of the as grown material at 450 °C hematite nanorods were formed, while a short annealing at 350 °C for 15 min resulted in the formation of maghemite nanorods.

4.4. Synthesis of bifunctional 3D electrode based on Co_3O_4/nitrogen-doped carbon nanotubes

NCNTs/CP support electrode was prepared as described in section 4.1. In the next step, 0.545 g of cobalt nitrate hexahydrate ($Co(NO_3)_2.6H_2O$, 1.9 mM) was dissolved in 30 ml deionized water/ethylene glycol (1:1) mixture and then poured into a 30 ml autoclave. Then a sheet of NCNTs/CP was placed in the autoclave and maintained at 160° C for 16 h. The resulting material was washed in water and ethanol separately and then treated at 300 °C for 2h. In this step as synthesized cobalt carbonate hydroxide hydrate nanospheres which had formed on NCNTs, transformed to Co_3O_4 nanospheres.

5. Characterization

5.1. Electron microscopy

Limitation of human eyes in resolving objects, has led to the development of optical and electron microscopes. However, due to the Rayleigh criterion, which correlates the resolving ability of the detection method to the wavelength of the imaging process, the resolution of nanoscale objects is however far beyond the capability of light microscopes. By using an incident radiation with smaller wavelength than visible light the resolution can be improved. Electrons are ideal particles which meet this requirement since they are significantly smaller than atoms and if accelerated to some hundreds kV, the electron beam has a wavelength about one million times shorter than light waves. The electron microscopy is based on the simple scattering of electrons when passing through or reflecting from the material. Depending on the mode of operation, sophisticated information can be gained. The imaging mode of operation gives magnified view of the material morphology. The diffraction mode displays the local crystal structure and the analytical mode gives information on the elemental composition. Based on the type of the scattered electrons that are detected, different types of electron microscopy are categorized as explained below.

5.1.1. Transmission electron microscopy

Transition electron microscopey (TEM) produces images by detecting the electrons that are transmitted through the sample within a high vacuum chamber. To increase the resolution and to allow more electrons to pass through the samples, a thin specimen should be used (see figure 7a and 7b).

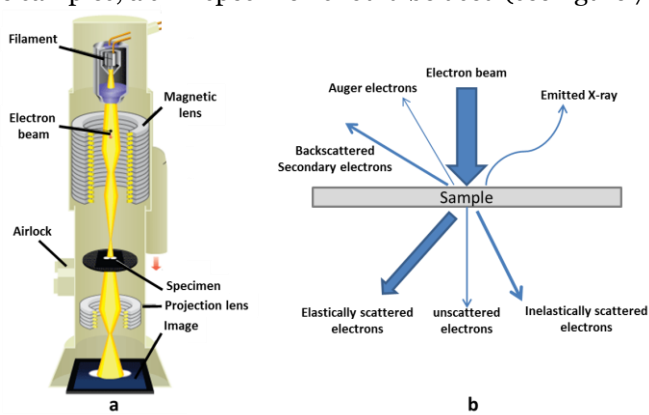

Figure 7 a) Schematic image of the working principle of TEM and b) different interactions of electron beam with the material

In TEM, the appearance of the transmitted electrons is highly dependent on the properties of the examined specimen such as density, thickness, crystalinity and composition. Since the transmitted electrons are analyzed and detected, a thick part of the specimen scatters the electrons more than the thin parts and a porous material will pass more electrons than a dense material. The type of image obtained is termed a mass and thickness contrast image, which allows detecting differences between heavy and light elements, but still not a full map of elemental composition. The obtained contrast image is magnified and projected by magnetic lenses on a fluorescence screen. The analog images of electron density variations can be captured with the help of a CCD camera.

In our studies we have widely used TEM and high resolution TEM (HRTEM) to charachterize the morphology of our synthesized material. TEM and HRTEM studies were carried out on a JEOL JEM-1230 and JEOL 2100F, respectively.

5.1.2. Scanning electron microscopy

Scanning electron microscopy (SEM) technique gives a high magnification image with a good depth of field. Similar to TEM high energy electrons are used, but here usually the secondary and the backscattered electrons ejected from the surface of the material are detected and analyzed. SEM signal does not only give information about the surface morphology in 3D but also the chemical composition. The chemical composition can be analyzed by using the closely related technique of energy dispersive X-ray microanalysis (EDX) in which the generated characteristic X-rays during electron-material interaction is analyzed. The kinetic energy of backscattered electrons holds information about the binding energy of the electrons to the nucleus and will therefore lead to an image which gives composition contrast. The secondary electrons are low energy electrons (<50 eV), meaning that only those ejected from surface atoms are able to escape from the material. Hence, the study of secondary electrons gives information about the surface and not from the interior part of the sample. Since the SEM detector can detect the ejected electrons in different directions, a 3D image can be obtained.

The morphology and composition of our material were characterized using a Zeiss Merlin FEGSEM microscope.

5.2. Raman spectroscopy

Raman spectroscopy is based on the analysis of the inelastic scattering of monochromatic light interacting with the material. During this scattering process, energy is exchanged between the photons of the incident light and the molecules of the sample. As the consequence of this interaction, the scattered photons have either higher or lower energy compare to the incident photons. The energy difference between the incident and scattered photons

is made up by a change in the rotational and vibrational energy of the molecule. There are two distinguishable Raman scattering processes. If the material absorbs energy from the incident photons, the emitted photons have lower energy than the incident one and the process is referred to as Stokes Raman scattering. On the other hand, if the photons are emitted with energy higher than the incident photons, the process is then referred to as anti-stokes Raman scattering. In other words, the Stokes process is referred to as phonon emission process while phonon absorption causes anti-Stokes radiation. Different light scattering processes considering energy levels are schematically shown in figure 8.

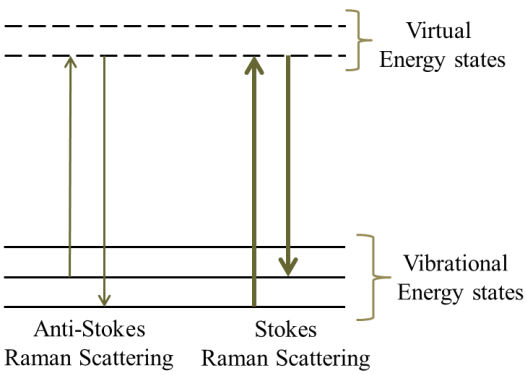

Figure 8. Scattering processes of light including Stokes and anti-stokes Raman scattering

The intensity of Stokes radiation is generally higher, because anti-Stokes radiation can occur only when the molecule is already in an excited state (vibrational or rotational). This is less probable compared to the probability of molecules being in the ground state, as described by the Boltzmann distribution. Therefore, it is more common to study the Stokes Raman scattering during the Raman spectroscopy. The resulting Raman spectrum is then a plot of the intensity of the scattered light *vs*. the frequency downshift. The commonly accepted energy scale is to plot the intensity *vs*. the energy in terms of wave numbers (cm^{-1}), where 8 cm^{-1} corresponds to 1 meV. Since the phonon energies of atoms and molecules vibrating in a structure differs depending on their chemical environment, Raman spectroscopy is a very powerful tool to investigate binding configurations and structural phases of materials.

In our work we have used Raman spectroscopy mainly to gain information on the configuration of the synthesized material directly after being synthesized and then to track the success of phase transformation to metal oxides (including Fe_2O_3 and Co_3O_4) after different type of treatments. Raman spectroscopy was also used to gain information on local structure in carbon nanostructured materials. The Raman spectroscopy was conducted on a

Renishaw InVia Raman spectrometer with a charge-coupled device detector. As excitation source, the most commonly used was a He-Ne laser with the wavelength of 633 nm.

5.3 X-ray photoelectron spectroscopy

When a photon impinges on an atom three types of process may occur: 1) the photon passes the atom without any interaction, 2) the photon can scatter with partial energy loss due to interaction with electrons in the atomic orbitals and 3) the photon energy may transfer completely to the electron, leading to electron emission. The latter describes the emission process which is the base of X-ray photoelectron spectroscopy (XPS). In XPS, the sample is illuminated by X-rays of energies in the KeV range. This causes the ejection of core (inner shell) electrons, due to photon absorption by atoms of the sample. The energy of each emitted electron is a function of its binding energy which is an elemental property. The emission process is extremely fast (on the order of 10^{-6} s) and can be described based on the Einstein equation:

$$E_B = h\vartheta - KE \qquad (14)$$

Where E_B is the binding energy of the electron, $h\vartheta$ is the energy of the incoming X-ray and KE is the kinetic energy of the emitted electron. So by detecting the kinetic energy of the emitted electrons, the electron binding energy can be calculated (since the core electron is ejected). This binding energy is the elemental "fingerprint" and hence the XPS spectrum gives a full description about the surface elemental composition of the examined material. However since the binding energy of the core electrons are also influenced by the chemical environment to which the atom is bound, information can also be gained about the chemical environment around the atoms, as well as charge states of the atoms and ions in the structure. To derive such information, the resolution in energy needs to be "fine-tuned" around the energy of the element of interest, and therefore this technique is often referred to as high resolution XPS.

5.4. Thermogravometric analysis

In a thermogravometric analysis (TGA) measurement the weight variation of a material is measured either as a function of temperature or isothermally as a function of time in different environments such as air, oxygen, nitrogen or in vacuum. In a typical measurement an appropriate amount of material (few milligrams) is loaded in the TGA crucible and heated to a set temperature (usually between 250 °C and 1000 °C). Thereafter the mass variation is monitored as a function of temperature and time when the material is burnt (oxidized) or evaporated. Since phase transformations

require energy, without changing the mass, such processes can also be detected by using a constant heat flow in the chamber.

5.5. Electrochemical testing

Electrochemistry is the study of reactions in the interface of a metallic phase (electrode) and a conductive solution (electrolyte solution). Thus, in electrochemistry the interaction between electrical energy and chemical reaction is studied. Electrochemistry focuses on chemical reactions in which electron transfer between species are involved. These particular chemical reactions are called oxidation-reduction or red-ox reactions. In the reduction process, the oxidizing agent is reduced by recieving an electron when it reaches to the vicinity of the electrode while in the oxidation process the reaction evolve by loss of electron. By the electron transfer from/to the electrode, current is generated. If the rate of reaction is the same in both red-ox directions, the system is at equilibrium and the measured current is known as the exchange current (i_o). Potential can be applied to the system to direct the reaction and concurrently the generated current can be measured. Since it is not possible to measure the potential difference of the metal and solution (electrolyte solution), the potential difference between two electrodes which are immersed in the same solution is measured. It is even more useful to immerse the electrodes in different solutions and measure the sum of "half cell" potentials-the so called galvanic cell. In most of the electrochemical testing, the reaction on one of the electrodes (half reaction) is of interest. Since we need to monitor both the current and voltage on the electrode of interest (working electrode), we need some standard reference electrode. Examples of common reference electrodes are silver chloride (Ag/AgCl), standard hydrogen electrode (SHE) and saturated calomel electrode (SCE). However, the reference electrode should not be used as a current carrying electrode since by doing this its potential would change. Therefore a third electrode is used as a counter electrode. This type of setup is known as a three electrode system and is used to study the electrochemical behaviour of electrode materials in electrochemical transient techniques such as linear sweep voltammetry (LSV) and cyclic voltammetry (CV).

5.5.1. Linear sweep voltammetry

In LSV, a fixed range of potential is chosen and the voltage is scanned from the lower voltage limit to upper voltage and the generated current is recorded at predefined potential steps. From the C-V plot extractracted from LSV measurement, it is possible to determine the onset potential of reactions and hence the overpotential needed for the reaction to occur. If the potential is scanned slowly (less than 5 mV/s), the data can be used to generate Tafel plot which enables to derive the exchange current density as explained in

section 3.1.1. The later give valuable information about the kinetics of reaction.

5.5.2. Cyclic voltammetry

CV is similar to LSV in the sense that the voltage is swept between two fixed pre-defined values (*i.e.* V_1 and V_2) at a fixed rate. The difference is that in the case of CV the current is recorded when the voltage is scanned from V_1 to V_2 but also when it is reversed and swept back to V_1. The forward scan provides identical information as recorded in LSV. In the forward scan the electrode material is oxidized, while it is reduced in the backward scan. By acquiring CV measurement, the cathodic and anodic currents can be obtained in one scan and the peak potentials can be defined. In addition, it gives qualitative information about the presence of intermediates in the red-ox process and the reversibility of the reactions.

5.5.3. Rotating disk and rotating ring disk electrode measurement

In a regular CV measurement, the current signal can be easily influenced or disturbed by the bulk diffusion. For steady-state experiments, it is therefore preferred to force the solution to move in a well-defined and controlled manner. Rotating disk and rotating ring disk electrodes (RDE and RRDE) are two types of working electrodes which are used in such hydrodynamic systems. In this way, it is possible to take advantage of the steady-state laminar flow conditions close to the RDE or RRDE to collect useful information about electrode reaction kinetics. The rotation of the electrode facilitates a steady stream of material from the bulk of the solution to the electrode surface. The diffusion of the solution towards a RDE was first modelled by Benjamin Levich given in the form of the following equation:

$$i_{a/c} = 0.2\, nFA(D_{O/R})^{2/3} v^{-1/6} C_{O/R} \omega^{1/2} \qquad (15)$$

Where $i_{a/c}$ is the anodic/cathodic limiting current, n is the electron transfer number, F is Faraday constant, A is the electrode area, v is the viscosity of the solution, $D_{O/R}$ and $C_{O/R}$ are the diffusion coefficient and concentration of the oxidized/reduced species and ω is the angular rotation rate of the electrode. It is common to study the kinetics of the reaction by studying Koutecky-Levich plots (K-L plot) for which a series of voltagramms are acquired on the rotating disk electrode over a range of different rotation speeds. Then the reciprocal of achieved currents are plotted against the square root of the rotation speed. Based on Koutecky-Levich equation:

$$\frac{1}{i} = \frac{1}{i_k} + \left(\frac{1}{0.2\ nFAD^{\frac{2}{3}}v^{-\frac{1}{6}}C}\right)\omega^{-\frac{1}{2}} \qquad (16)$$

Figure 9. Ring-disk geometry of RRDE

i_k (the kinetic current) can be calculated from the intercept of the linear K-L plot with the x-axis. The kinetic current is the current that can be measured in the absence of the mass transport limitation. Furthermore the electron transfer number for the electrochemical reaction can be calculated from the slope of the curves in K-L plots. The main idea behind developing the "ring-disk" geometry for the working electrode (shown in figure 9) is to detect the stream of generated half reaction products at the disk electrode, while passing the ring electrode. The onset potential of the reaction can be precisely extracted from CV voltagramms recorded at RRDE.

5.5.4. Electrochemical impedance spectroscopy

In electrochemical impedance spectroscopy (EIS), the electrochemical impedance is measured by applying a small AC excitation signal to the system and then measuring the current through the cell. By applying a small signal, the response of the system would be in the same nature (say we apply a sinusoidal potential excitation and the response is also sinusoidal with the same frequency) but shifted in phase. If the excitation signal has the form:

$$E_t = E_0 \sin(\omega t) \qquad (17)$$

Where E_t is the potential at time t, E_0 is the amplitude of the signal and ω is the radial frequency. The response signal then has the form:

$$I_t = I_0 \sin(\omega t + \varphi) \qquad (18)$$

Where φ is the phase shift. Then the impedance of the system can be calculated from eq. 6:

$$Z = \frac{E_t}{I_t} = \frac{E_0 \sin(\omega t)}{I_0 \sin(\omega t + \varphi)} = Z_0 \frac{\sin(\omega t)}{\sin(\omega t + \varphi)} \qquad (19)$$

Using the Euler relationship, the impedance can be represented as a complex number:

$$Z(\omega) = Z_0(\cos\varphi + j\sin\varphi) \qquad (20)$$

If the real part of impedance is plotted on x-axis and the imaginary part on y-axis we get the "Nyquist plot" in which the impedance can be represented as a vector of length$|Z|$. The Nyquist plot is ideally a semicircle with the origin on the x-axis but often only a portion of the semicircle is seen and in some cases more than one semicircle is obtained. More details in this matter are discussed in the results section and in paper V.

EIS is a powerful tool to characterize voltage losses and hence to diagnose the limitations of the electrochemical cell and particularly the electrode materials and its constituents. By fitting a suitable equivalent circuit model based on the Nyquist plot, the charge transfer and different interfacial resistances can be characterized.

5.5.5. Li-ion battery test

Battery tests include both voltammetric and galvanostatic measurements. The voltammetric measurement is the same as mentioned in previous sections. The galvanostatic measurement refers to an electrochemical polarization technique in which the electrode is maintained at a constant current and then the cathodic and anodic behaviours are observed. The cyclic charge/discharge technique is a standard galvanostatic method to test the performance and cycle life of the electrodes. Usually the charge of each cycle is measured and then the capacitance is calculated using eq. 21:

$$C = \frac{Q}{E} \qquad (21)$$

Where C is the capacitance, Q is the measured charge and E is the cell potential. In practice, charge value is used instead of capacity with the unit of ampere-hour (Ah) where 1 Ah is 3600 coulombs. The capacity is then plotted *vs*. the cycle number and the plot gives information about the stability of the electrode upon cycling.

The performance of a battery is usually expressed as the energy density which is a measure of the energy of the battery in comparison to either its weight or volume. The efficiency of a rechargeable battery can be stated as coulombic and energy efficiencies. Coulombic efficiency of a battery is the fraction of stored charge during cycling to the recoverable charge during discharge. This can be calculated from the charge/discharge cycle. The energy efficiency is then the ratio of the output energy and the input energy and is usually lower than the coulombic efficiency.

6. Results and discussion

6.1. Pristine and nitrogen-doped carbon nanotubes

Pristine carbon nanotubes (CNTs) and nitrogen-doped CNTs (NCNTs) were grown on Fe (or Fe/Co) catalyst by chemical vapour deposition (CVD) using either acetylene or pyridine as C or C/N precursor as described in section 4.1. Figures 10a-c show TEM images of the synthesized NCNTs in which the bamboo structure and highly defective parts are clearly seen. We have established that the structure, purity, dimensions and nitrogen doping level of the tubes are time dependent. Pure and smaller tubes were attained with short growth time while there was an optimized growth time to achieve highest level of doping. Both pristine and doped tubes were grown in bamboo shaped morphology. There are several studies explaining the growth mechanism of bamboo shaped CNTs.[171-173]

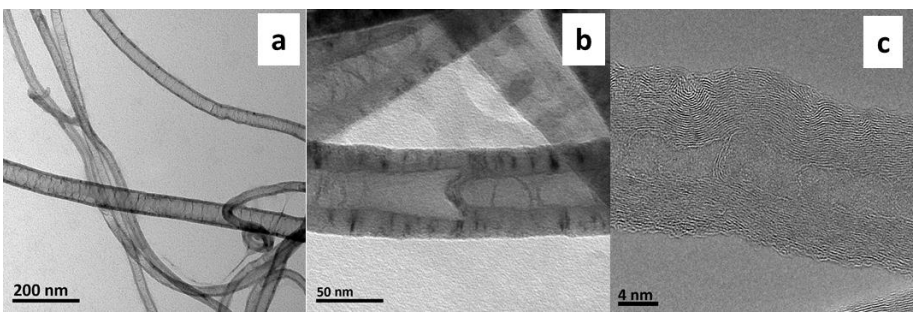

Figure 10. TEM (a and b) and HRTEM (c) of the synthesized NCNTs showing the bamboo shaped morphology and defective walls of MWCNTs

SEM images of NCNTs on different substrates are shown in figure 11a and b. It is clear that NCNTs are highly aligned when they are grown on silicon substrates but that they grow much denser on the fibers of CP. Depending on the diffusion permittivity of the catalyst, the growth mechanism can be defined. Even though it is not possible to explain the growth mechanism based on a single growth parameter, it is clear that the catalyst material and composition have distinct effect on the morphology of the product.[174] Beside this, addition of nitrogen during the growth process results in a curved structure and hence formation of bamboo-like structure.[52]

6.2. Nitrogen functionalities in NCNTs

It is well established that nitrogen can be incorporated in the structure of CNTs in different configurations and with different properties. The detailed studies of the growth of NCNTs and configuration of nitrogen functionalities in the structure of CNTs are presented in paper I and II.[166, 175]

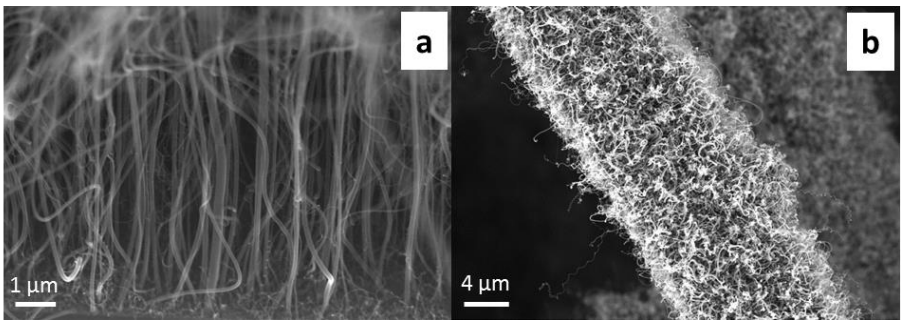

Figure 11. SEM images of NCNTs grown on a) silicon wafer and b) fibers of carbon paper (CP)

It has been proved that the catalytic properties of nitrogen can be varied depending on its position in the carbon framework.[176-177] This is rationalized on the dissimilar environment of nitrogen when it is located at different sites. There is increasing number of studies investigating the intrinsic electrochemical properties of NCNTs particularly towards catalytic electrochemical reactions such as oxygen reduction reaction (ORR)[178-179] or oxygen evolution reaction (OER)[140, 150] in water electrolysis. There are two main problems facing such studies; large controversy regarding the assignment of nitrogen functionalities as well as the catalytic activity of various functionalities. Without overcoming the first problem, *i.e.* thoroughly assigning the types of nitrogen functionalities present in the samples, the correlation between catalytic efficiency and type of nitrogen functionality is not feasible. XPS is a strong tool to characterize and assign the nitrogen functionalities present in NCNTs. As mentioned before, by studying the XPS spectrum we are actually looking at the binding energy of each element to its neighboring elements. However, the interpretation and assignment of nitrogen functionalities in carbon nanostructures is not straightforward and depends on a number of factors.

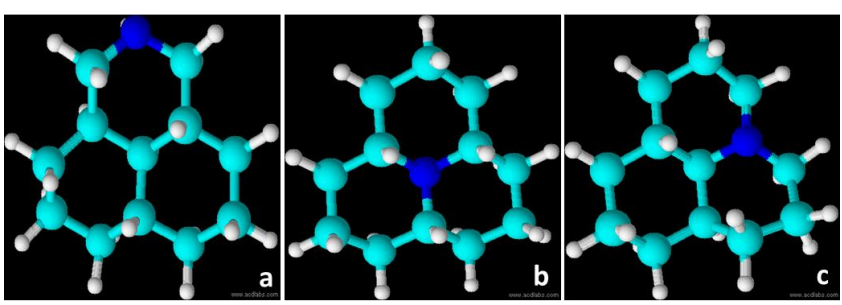

Figure 12. Some probable nitrogen functionalities in the carbon framework-nitrogen atoms are shown by blue circles

First of all, XPS is a surface characterization technique and does not give a complete picture of the bulk composition of the elements which are present in the material. Second, the binding energies related to different nitrogen functionalities are in many cases very close and thus very difficult to resolve and distinguish. Calculation of the charge contributed to nitrogen in its different locations gives useful information about the type of functionality.[39] The charge contribution of three nitrogen configurations shown in figure 12 has been investigated and it is shown that the positive charge on the nitrogen atoms increases from a to c.

The corresponding view of these functionalities in a carbon framework (from either the outer cylinder of a multiwalled carbon nanotube or a graphene sheet) is presented in figure 13. N1 nitrogen is calculated to be the least positively charged nitrogen and usually is referred to as pyridinic nitrogen in literature. The name comes from the similarity between the configuration of nitrogen in the carbon skeleton and pyridine.

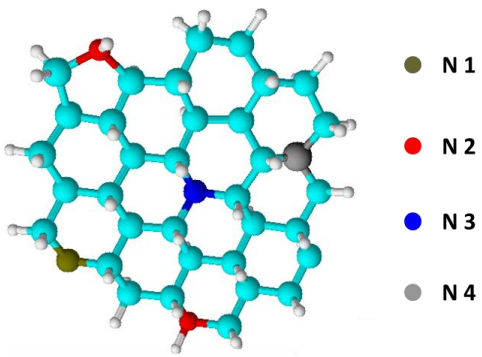

Figure 13. Different nitrogen functionalities in a graphitic sheet; N1, N2, N3 and N4 represent pyridinic, pyrrolic, N-Q_{centre} (graphitic) and N-Q_{valley}

As mentioned in section 2.3, pyridinic-N refers to nitrogen atoms which contribute to the π-system with one p-electron and a well-defined peak centered at the binding energy of ~398 eV is assigned to this functionality in XPS spectrum.[180] The so called Pyrrolic-N (N2) contributes to the π-system with two p-electrons and hence has higher binding energy. Substitution of C by N either in a six-membered ring or a defective five-membered ring leads to formation of pyrrolic-N (note the two different configurations in figure 13). The binding energy of this functionality is different in multiwalled and single walled CNTs, due to the higher curvature in the latter. In the XPS spectrum of multiwalled NCNTs it appears at around 400.3 eV.[181] A typical wide XPS spectrum of NCNTs is shown in figure 14a with an inset of the high resolution N 1s peak.

The N 1s peak in XPS spectrum usually also contains a broad peak with the center around 401 eV with full width half maximum (FWHM) of 3 eV. Therefore this peak (usually referred to as quaternary-N peak, N-Q) needs to be deconvoluted to several peaks assigned to several nitrogen functionalities. The assignment of these functionalities is still under debate but analysis of model compounds has assisted in their identification. According to the calculations by Pels *et al.*[39] the nitrogen substituted in the place of a carbon in the bulk of carbon framework (not at the edge) is slightly less positively

charged than the nitrogen replacing a carbon in the valley site at the edge (N3 *vs.* N4 in figure 13). Due to this, these two functionalities which we call them N-Q_{center} and N-Q_{valley}, differ in binding energy by around 1 eV.

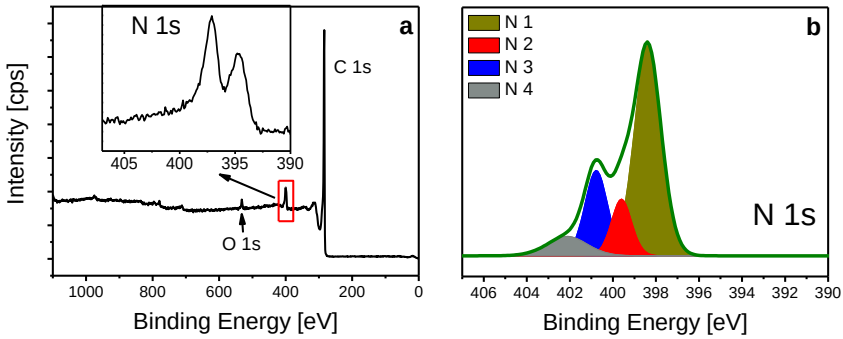

Figure 14. a) Typical XPS spectrum of NCNTs with assigned peaks, inset) high resolution N 1s peak and b) deconvolution of a typical N 1s peak to four distinct peaks

The peak centered at ~401 eV is assigned to N-Q_{center} while the N-Q_{valley} exhibit a peak at ~402.3 eV (see figure 14b). The N-Q_{center} peak is a well-addressed functionality in the literature, and is usually called graphitic-N, while the peak attributed to N-Q_{valley} is often misinterpreted. In addition to these four main peaks, it is common that also peaks at higher binding energies are observed. The assignment of these peaks is under some controversy, and it has been suggested that they can be assigned to both molecular nitrogen and nitrogen oxide groups. Even though, it was not clear for us in the beginning, we now believe that the appearance of the peak at the binding energy of ~403 eV is due to π-π interaction, which is typically observed in carbon systems, but the strength of these can be very different depending on sample properties.

Nitrogen doping level and type of nitrogen functionalities depend strongly on synthesis conditions but is not easily controllable.[166, 182-183] By investigating nitrogen functionalities in NCNTs with different levels of nitrogen doping, we observed that (paper I) the type of nitrogen inclusion changes in relation to the total amount of nitrogen incorporated to the NCNTs. We studied NCNTs with the doping level from 1 % to 9.2 %.

Based on the results shown in figure 15a, at low doping level the pyrrolic-N is dominant but around 4-5% there is a transition in nitrogen type. Pyridinic-N starts to incorporate faster and become dominant in such a way that at high nitrogen level the atomic concentration of pyridinic-N is almost two times of the pyrrolic-N. We observed that, dissimilar to pyridinic-N, the increasing rate of pyrrolic-N is not in line with the increasing rate of nitrogen inclusion.

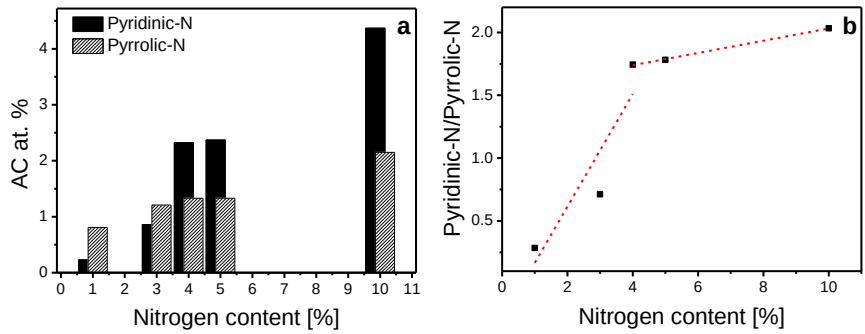

Figure 15. a) Relative abundance behavior of pyridinic and pyrrolic-N as a function of nitrogen content and b) ratio of pyridinic-N to pyrrolic-N incorporation as a function of nitrogen content.

This can be seen easier by plotting the ratio of the atomic concentration of these functionalities *vs.* the total nitrogen content as shown in figure 15b. The results from the XPS can be further correlated with Raman spectroscopy. In line with expectations, the Raman spectrum of NCNTs contains more defective related features than pristine CNTs. A typical Raman spectrum of NCNTs is shown in figure 16a. The spectrum shows a strong first order feature at ~1560 cm^{-1} (G-band) which can be seen in all graphitic carbon structures.

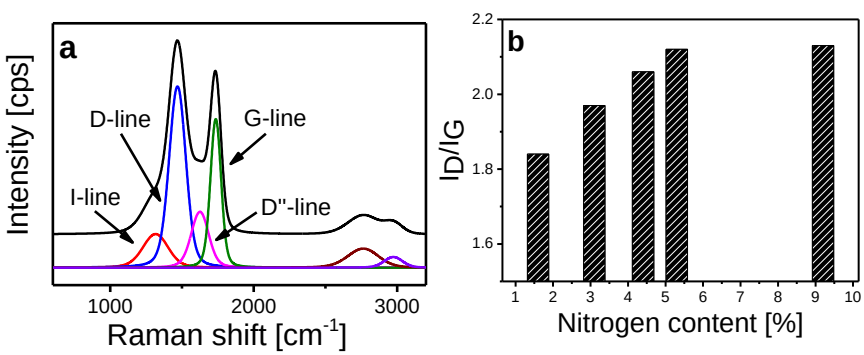

Figure 16. a) Typical Raman spectrum of NCNTs fitted by Voigtian functions and b) the respective ID/IG as a function of nitrogen content

The appearance of an additional feature at ~1350 cm^{-1} (D-band) in the Raman spectrum is indicative for a defective carbon structure. Such peak is in principle present to some extent in all carbon nanotube samples, both single-walled carbon nanotubes as well as multi-walled carbon nanotubes, but the appearance of this peak differ between samples with different type of defects. As seen in figure 16a we have fitted several peaks in the main peak envelope. By analyzing these peaks we can thus get information on the types

of structural disorder in the structure.[20] We used a 4-peak model to fit D and G bands of the Raman spectra of NCNTs and by this, D-band could be deconvoluted to 3 lines. These features are all defect related but with different origins.[184] Beside the main D-line, the defect related feature at lower frequency, called I-line, is usually seen in nitrogen-doped or heavily disordered carbon structures.[185] The other defect related feature at comparatively higher frequency (~1470 cm^{-1}) is referred to as D″-line and is used as an indicator of stacking defects in graphene layers.[186] This feature can exhibit high intensity in NCNTs due to an increase in the turbostratic character in graphene layer stacking.[187] The defective structure of NCNTs can be characterized by measuring the integrated area ratio of D to G band intensities; I_D/I_G. In figure 16b, I_D/I_G is plotted against the total amount of nitrogen in order to correlate the data with those shown in figure 15b. I_D/I_G increases up to the nitrogen content of about 4-5 % and thereafter remains unchanged. This transition in behavior of I_D/I_G occurs at the same nitrogen content as in the nitrogen functionalities ratio (pyridinic-N/pyrrolic-N). From this study one can conclude that the nitrogen incorporation differs in the low nitrogen content from that at high content and that the transition point is at around 5%. The further main aim of our studies was to gain more knowledge on the role of nitrogen functionalities in catalytic activity of NCNTs in electrochemical reactions such as in ORR. By a firm assignment of nitrogen functionalities from the XPS data, one of the main obstacles in such a study could be overcome.

6.3. Transformation of nitrogen functionalities in NCNTs

In our study which is presented in paper II, we aimed to find out the most catalytic active site for ORR and therefore we needed different samples with a variety of nitrogen functionalities. To attain a more reliable conclusion, instead of controlling the type of nitrogen functionalities in the growth process we tried to transform the nitrogen functionalities into other types in the already synthesized set of sample. Thus, a post treatment step was applied to the grown NCNTs. A batch of NCNTs was synthesized using FCCVD (the powder form product) as described in section 4.1 which gives considerably homogeneous nitrogen content throughout the material. Then a simple heat treatment approach was used. The material was annealed in argon for a pre-defined time at different temperatures. The nitrogen functionalities were scanned for different treatment temperatures ranging from 500 °C to 1000 °C.

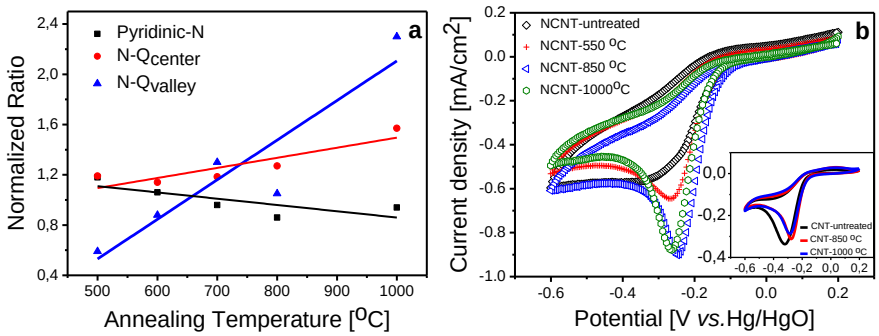

Figure 17. a) Normalized ratio of nitrogen functionalities calculated from eq. 22 vs. annealing temperature and b) Cyclic voltammograms in oxygen-saturated 1 M KOH for pristine CNTs and NCNTs annealed at different temperatures

The as-synthesized NCNTs before any thermal treatment have a distribution of nitrogen functionalities which is determined from XPS. To be able to analyze the response of nitrogen functionalities to thermal treatment, we normalized the atomic concentration of each nitrogen functionality to its original concentration before heat treatment using eq. 22:

$$Normalized\ ratio = \frac{I(N\ 1s)\ of\ specific\ N\ functionality_{treated\ at\ temperature\ T}}{I(N\ 1s)\ of\ specific\ N\ functionality_{before\ heat\ treatment}} \qquad (22)$$

Where I(N 1s) is the integrated area of specific nitrogen functionality obtained from deconvolution of N 1s signal of XPS spectrum. Figure 17a shows the response of three main nitrogen functionalities in our sample to heat treatment. It should be mentioned that pyrrolic-N (N2) which was present in the as synthesized material decreases rapidly and disappears completely after annealing at temperatures higher than 500 °C in agreement with earlier reports.[188] The fast decrease in pyrrolic-N is concurrent with a slow decrease in pyridinic-N and a rapid increase in N-Qs ($N\text{-}Q_{center}$ and $N\text{-}Q_{valley}$) as shown in figure 17a. We explain this observation by a "condensation reaction" as suggested by Pels *et al.*,[39] in which the appearance of $N\text{-}Q_{center}$ and $N\text{-}Q_{valley}$ is the consequence of the rearrangement of the rings in such a way that pyrrolic-N and pyridinic-N disappear partially (see figure 18a and 18b).

Our results indicate that pyridinic-N functionalities are more stable than pyrrolic-N but that both are transformed to N-Qs when a sufficient temperature is provided.

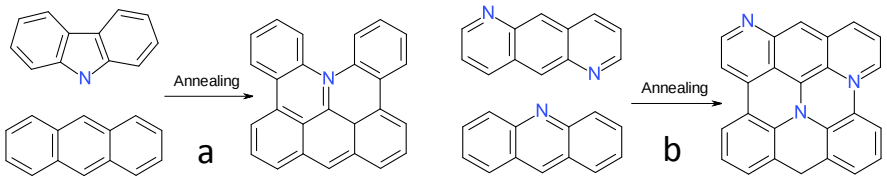

Figure 18. Condensation reactions by annealing a) from pyrrolic-N (N2) to N-Q_{valley} (N4) and b) from pyridinic-N (N1) to N-Qs (N-Q_{center} and N-Q_{valley})

We show that while having the same starting material, by a simple treatment at high temperature the material converts to a sample containing more N-Qs. After annealing at 1000 °C, the ratio of N-Q_{valley} is almost 2.5 times higher than that in the starting material. By attaining high diversity of nitrogen functionalities in different samples, electrochemical testing was performed using these materials as an all organic catalyst material for ORR which will be presented in the following sections.

6.4. Configuration of catalytically active site in NCNTs for ORR

The treated NCNTs at different temperatures were tested toward ORR and compared with the original sample. To get a reference sample, enabling us to rule out differences originating from non-nitrogen effects on the electrochemical performance, pristine CNTs were synthesized and thermally treated at the same condition as for NCNTs. Figure 17b shows the electrocatalytic performance of heat treated NCNTs (and untreated) loaded glassy carbon electrode towards ORR in 1 M KOH. The inset shows the response of heat treated pristine CNTs (and untreated) modified electrodes which were prepared and tested under the same condition.

It is clear from the obtained results that the thermal annealing does not significantly affect the ORR properties of the pristine CNTs. In agreement with previous reports, the ORR current density of untreated NCNTs is two times higher than CNTs.[189-190] The distinct influence of thermal annealing of NCNTs on ORR properties can be seen in figure 17b in which the current density attains its maximum value for the sample treated at 850 °C. The obtained current density is 1.7 times higher than the untreated NCNTs. By correlating the ORR measurements with the XPS analysis presented in figure 17a, we suggest that the increasing of N-Q_{valley} sites in high temperature treated samples lead to the sharp increase in ORR current density. High catalytic efficiency of quaternary nitrogen has been shown before[191-192] but separate contributions of N-Qs (N-Q_{center} and N-Q_{valley}) have not been considered. To obtain more information on the kinetics of ORR, different electrodes were prepared using similar materials for rotating disk electrode (RDE) and rotating ring disk electrode (RRDE) measurements. To get a

better insight about the mechanism of ORR on our material the electron transfer number was calculated for all the electrodes using two methods based on the RRDE measurement. The first method was to obtain "n" using eq. 23 at the potential of -0.6 V:

$$n = \frac{4I_D}{I_D + \frac{I_R}{N}} \qquad (23)$$

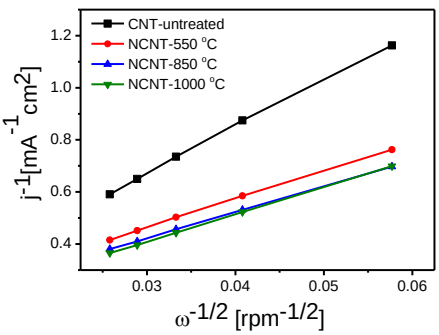

Figure 19. Koutecky–Levich plots of ORR at different potentials on CNTs and heat treated NCNTs-modified electrodes

where I_D is the Faradaic disk current, I_R is the Faradaic ring current, and N=0.4 is the collection efficiency. The electron transfer number can be calculated using the K-L plot which is based on the RDE current at different rotation rate of electrode. K-L plot for as synthesized pristine CNTs and treated NCNTs modified electrodes are shown in figure 19. In this method, "n" can be calculated from the slope of K-L plots (B) using eq. 24:

$$B = 0.2nF(D_O)^{2/3}v^{-1/6}C_O \qquad (24)$$

where F is the Faraday constant, D_O is the diffusion coefficient of O_2 in electrolyte, v is the kinetic viscosity and C_O is the bulk concentration of O_2. Taking the average of values calculated for "n" from these two methods, electron transfer number measured over four tested electrodes are 1.9±0.3, 2.7±0.1, 3.0±0.1 and 2.9±0.2 for bare CNT, NCNT-550, NCNT-850 and NCNT-1000. It is clear that we have gone from a process dominated by two-electron pathway for ORR on CNT modified electrode to the ORR process dominated by four-electron process on NCNTs modified electrode. However the highest electron transfer number that we could calculate is 3; the thermal annealing has a minor effect on this value. It is believed that ORR proceeds *via* four-electron pathway on nitrogen edge defects (such as pyrrolic, pyridinic and N-Q_{valley} sites) while on bulk nitrogen defects (such as N-Q_{center}) it proceeds through a two-electron pathway (*via* production of H_2O_2).

We rationalize our results based on the fact that the steep increase in N-Q_{valley} by heat treatment is concurrent with the decrease in pyridinic-N and slight increase in N-Q_{center}. N-Q_{valley} and pyridinic-N are edge defects and catalyze the ORR process *via* four-electron pathway but N-Q_{center} is a bulk defect and ORR on this site proceeds *via* a two electron pathway. The

coincident variation of nitrogen functionalities in the mentioned process gives rise to an unaffected electron transfer number by heat treatment.
By understanding the nitrogen inclusion mechanism and its intrinsic electroactivity, we started to develop hybrid catalyst materials based on nitrogen-doped carbon nanostructures including NCNTs and N-rGO$_x$ for electrochemical reactions. The achievements are presented in next sections.

6.5. Hybrid graphene nanoscrolls by adsorption of γ-Fe_2O_3 (maghemite) nanoparticles

Graphene nanoscrolls and in particular rGO$_x$ nanoscrolls are new members in the graphene family which are predicted to retain the high conductance of a single graphene sheet.[193] The appropriate layer spacing of nanoscrolls might allow for energy storage and battery applications.[194-196] In paper III,[197] we have studied the synthesis mechanism of the hybrid graphene nanoscrolls starting from N-rGO$_x$, and in detail characterized the material. The symmetric N-rGO$_x$ nanoscrolls (with the nitrogen atomic concentration of ~13%) are obtained by decorating N-rGO$_x$ with magnetic iron oxide particles in the form of maghemite (γ-Fe_2O_3). We show further that a similar decoration by less magnetic hematite (α-Fe_2O_3) never leads to any rolling. The experimental details are given in section 4.2 and are schematically illustrated in figure 20.

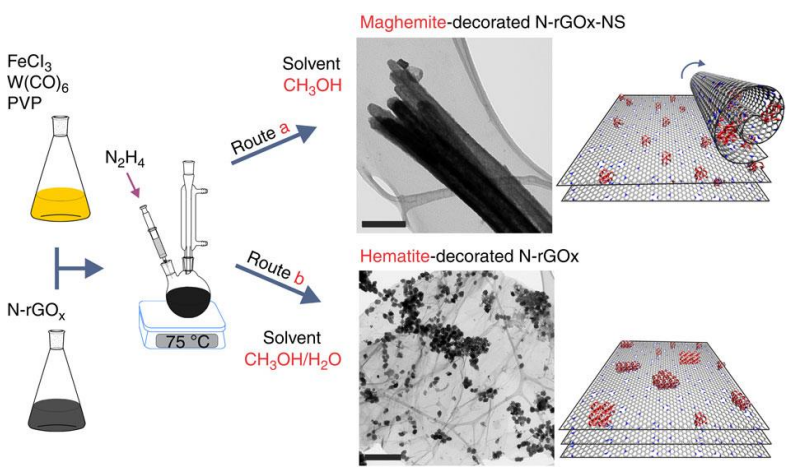

Figure 20. Schematic process for the adsorption of iron oxide nanoparticles; route a) Maghemite-decorated nitrogen-doped reduced graphene oxide (M-N-rGO$_x$) nanoscrolls, and (route b) hematite-decorated N-rGO$_x$ sheets (H-N-rGO$_x$)

From TEM images shown in figure 20, *route a* results in the formation of N-rGO$_x$ nanoscrolls with diameters of about 38 nm (by statistical analysis of more than 100 nanoscrolls). The nanoscrolls tend to arrange in bundles with up to 20 scrolls in each bundle. Maghemite nanoparticles are in the range of

3–5 nm, whereas the hematite nanoparticles on the N-rGO$_x$ sheets are in the range of 25–40 nm. Similar dimensions can be derived from XRD measurements for maghemite and hematite nanoparticles by using the Sherrer formula. By bearing in mind the measured maghemite particle size and considering the carbon-iron bond length and van der Waals interaction of adjacent graphene layers, we assume that a single graphene sheet is rolled approximately 3-5 turns. It should be mentioned here that, the presence of tungsten hexacarbonyl in the process is crucial for the rolling. Even though the actual role of tungsten is not clear, we do note that due the capability of tungsten to shift the isoelectric point of iron oxide particles towards higher pH, it is plausible that tungsten modifies the interaction of iron oxide nanoparticles by charging the nitrogen doped graphene sheets negatively.

Both maghemite and hematite have Raman active vibrational modes and hence their identification is possible by Raman spectroscopy.[198] Figure 21a shows the Raman spectra of maghemite decorated N-rGO$_x$ (M-N-rGO$_x$) and hematite decorated N-rGO$_x$ (H-N-rGO$_x$) which are products of *routes a,* and *b*. The high wave number regions of the spectra show similar features corresponding to the nitrogen-doped carbon structures.[166] The low frequency region of H-N-rGO$_x$ is deconvoluted into several peaks shown in figure 21b which are characteristic features of hematite[199-200] with the largest peaks corresponding to A_{1g} and E_g vibrational modes at 224 cm^{-1} and 289 cm^{-1}. The observed features in the Raman spectrum of M-N-rGO$_x$ (see figure 21c) match with the Raman active modes of maghemite. Several other features (denoted by "*") were observed which fits well with the W-O vibrational modes.[201]

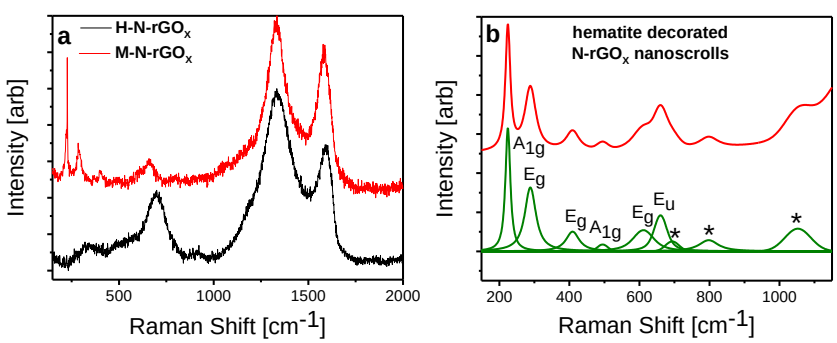

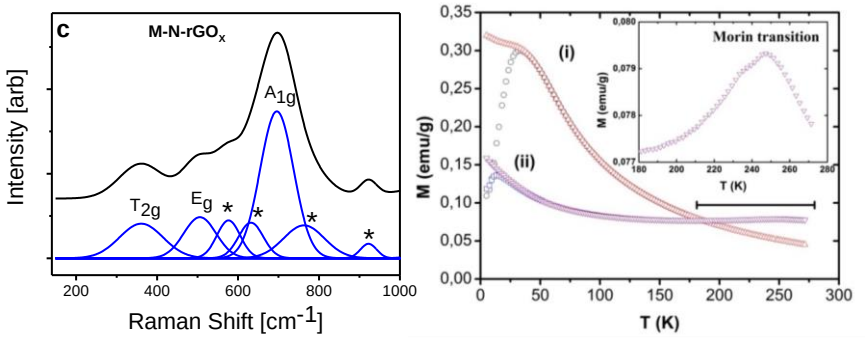

Figure 21. a) Typical Raman spectra of maghemite and hematite decorated N-rGO$_x$, Peak-fitted and assigned spectrum of b) maghemite-decorated rolled N-rGOx nanoscrolls, c) hematite-decorated N-rGOx (peaks originating from W-O vibrational modes are assigned with '*') and d) Magnetization *vs.* temperature at H=1,000 Oe of (i) maghemite-decorated N-rGOx nanoscrolls at ZFC conditions (black open circles) and at FC conditions (red up-triangles), and (ii) hematite-decorated N-rGOx sheets at ZFC conditions (blue open squares) and at FC conditions (purple down-triangles). Inset shows an enlargement of the high temperature region for hematite-decorated N-rGOx sheets.

We investigated the magnetic moment of maghemite and hematite by probing SQUID magnetization experiments on M-N-rGO$_x$ and H-N-rGO$_x$. The M *vs.* T at zero field cooled (ZFC) and field cooled (FC) conditions is shown in figure 21d. A significantly stronger magnetization of the maghemite nanoparticles compared to hematite was observed from these measurements. Beside this, based on the data from ZFC curves a characteristic super paramagnetic behavior was observed for both maghemite and hematite containing samples, showing a maximum at the blocking temperature, T_B.

T_B is observed to be higher for maghemite particles which is due to the larger interaction between nanoparticles and a smaller average size compared to the hematite particles.[202] For the small hematite particles we observe a characteristic Morin transition (inset in figure 21d) as expected for small hematite nanoparticles. The large magnetic interaction between the maghemite nanoparticles could thus be a reasonable cause of the formation of the nanoscrolls when the N-rGO$_x$ was decorated with maghemite nanoparticles. Having this in mind, we tried to monitor the rolling steps by observing the early stages of rolling. We stopped the process of rolling at different stages; 1) one minute after adding hydrazine by quenching the synthesis in an ice bath, b) refluxed for 5 h, and c) refluxed for 24 h. TEM images of these samples with the schematic images of each step are shown in figure 22a-f.

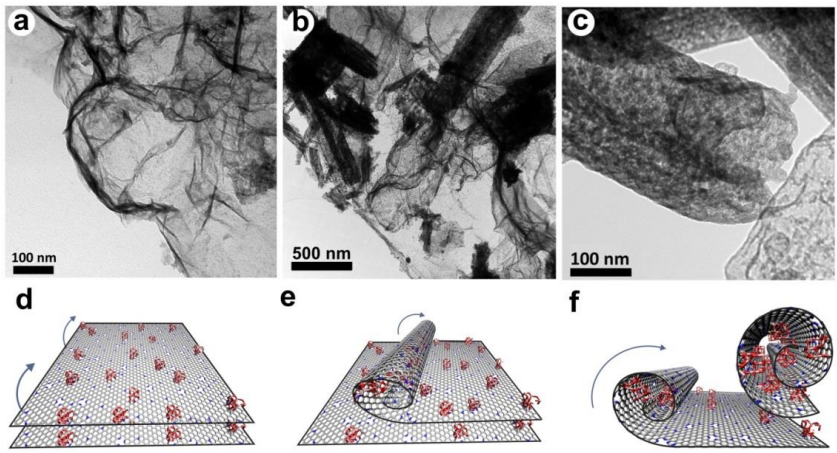

Figure 22. TEM micrographs of different stages of nanoscrolls synthesis (a-c) and corresponding time sequence scheme of scroll formation (d-f)

As can be seen from the TEM images the rolling process starts by decoration of the upper layer graphene by maghemite nanoparticles. When a sufficient loading is achieved, the upper layer rolls away and thereby exposing the underneath layer to decoration. This mechanism could also explain the formation of nanoscroll bundles. In our study we also found that a high nitrogen loading level is crucial for the rolling. Nitrogen defects in carbon nanostructures provide additional binding sites for metal particles[203] and hence promote the nucleation of the iron oxide nanoparticles compared to that on non-doped carbon nanostructures. This is due to the modification of the local electron properties of nearby carbons[204] and an asymmetric spin density[205] caused by introducing nitrogen atoms in the carbon structure. We strengthen this hypothesis by our experimental observation that non-doped rGO_x decorated with maghemite nanoparticles under similar experimental condition led to lower level of decoration and only weak signs of rolling were observed.

In line with our previous study, we also tried to explain the role of the specific nitrogen functionalities in the adsorption process of iron oxide clusters on N-rGO_x. We studied seven different nitrogen functionalities by *ab initio* calculations, which are schematically shown in figure 23. Based on our calculations, among the studied defects (figure 23) N_2Vc_1, N_3Vc_1, N_2Vc_2 and N_4Vc_2, which all contain pyridinic nitrogen functionality interact strongly with the iron oxide cluster. The adsorption energy of different nitrogen functionalities are summarized in figure 24a and Final geometrical configuration of the super cell is shown in figure 24b.

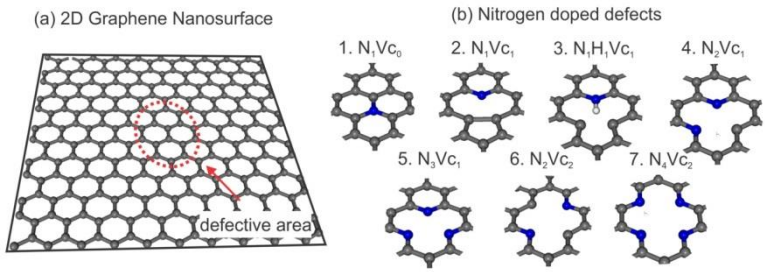

Figure 23. a) 2D supercell of graphene, the dashed line indicates the position of the nitrogen doping. b1-7) seven different nitrogen defects used in the *ab initio* calculations

To address also the rolling mechanism of the nitrogen-doped graphene sheets, we studied the formation energy of the nanoscrolls in different configurations. Figure 24c shows the formation energy of pure graphene sheets (black line) for which each rolling step (see figure 24d) requires higher and higher energy. By adding nitrogen defects and maghemite (blue line) both the energy barriers for the initial rolling step as well as the formation energy for the complete roll decreases. By further adsorption of another maghemite at the other end of the graphene nanoribbon (pink line), the formation energy of the nanoscroll decreases further. Finally, by also considering the magnetic spin-spin interaction between two neighboring maghemite (purple line), we observe a further decrease in the rolling energy, in particular for the final steps of rolling when the distance between two nanoparticles become smaller.

Based on the calculations and experimental observations we believe that the strong dipole moment of maghemite nanoparticles and their strong interaction with the nitrogen functionalities on the N-rGO$_x$ are the two most important promoting characters to initiate the nanoscrolls formation. Additionally, in contrast to previous reports on the graphene nanoscrolls[206] we are able to re-open the nanoscrolls to form flat few layer rGO$_x$ sheets. Based on our model for the formation of nanoscrolls it is plausible that they would be able to go back completely to the initial open N-rGO$_x$ structure upon removal of the maghemite nanoparticles. Indeed, analyzing TEM images of nanoscroll structures after the removal of the maghemite nanoparticles by washing M-N-rGO$_x$ in an acid mixture of HCl:HNO$_3$ (1:3 volume ratio) reveal that the sample go back to an open form of few layers N-rGO$_x$ (figure 25a and 25b).

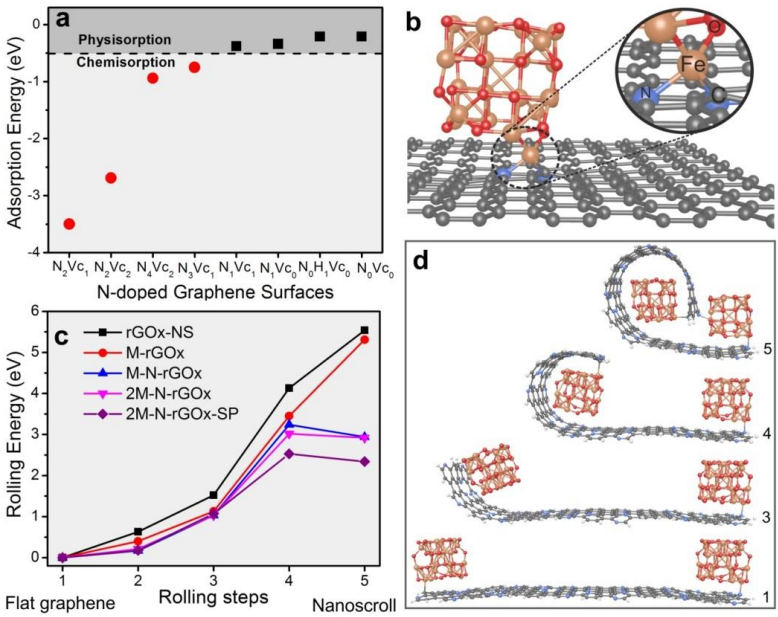

Figure 24. a) Adsorption energy of an iron oxide cluster on pristine (N_0Vc_0) and seven different nitrogen functionalities shown in figure 25b at a N-rGO$_x$ sheet where N (H) refers to the number of nitrogen (hydrogen) atoms and Vc the number of vacancies generated in the structure, b) Final geometrical configuration of the super cell, c) Rolling energy of graphene nanoribbons into nanoscrolls of pure carbon-rGO$_x$ (rGO$_x$-NS, black line), maghemite-decorated rGO$_x$ nanoscrolls (M-rGO$_x$ Red line), maghemite N-rGO$_x$ nanoscrolls (M-N-rGO$_x$ Blue line), maghemite N-rGO$_x$ nanoscrolls decorated with two maghemite nanoparticles, one at each end of the graphene nanoribbon (2-M-N-rGO$_x$ magenta line) and maghemite N-rGO$_x$ nanoscrolls decorated with two maghemite nanoparticles taking into account the spin–spin interactions of the two nanoparticles (2-M-N-rGO$_x$-SP purple line), d) Final geometrical structure at each rolling step of maghemite N-rGO$_x$ nanoscrolls decorated with two nanoparticles (2-M-N-rGO$_x$).

Interestingly, by applying the same procedure (as in *route a*) the re-opened acid treated M-N-rGO$_x$ could be rolled a second time by a similar maghemite decoration, but with a slightly larger diameter, probably originating from the defects introduced by the acid treatment (see figure 25c). Beside all the benefits with this synthesis method the only drawback was the challenges for up-scaling the product which inhibited the real test of the material for Li-ion batteries (LIBs). The amount of the produced material in each run was much below the amount necessary for battery tests.

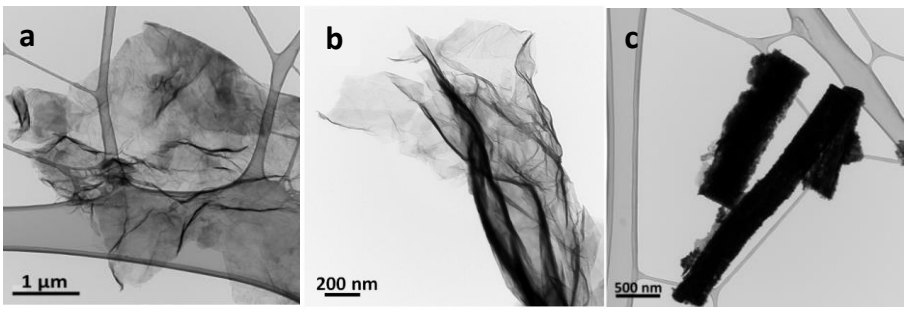

Figure 25. TEM images of a) acid washed M-N-rGO$_x$ for 24 h comprising single or few layers N-rGO$_x$, b) acid washed M-N-rGO$_x$ for 10 h in which half open structures could be found and c) re-rolled M-N-rGO$_x$-NS

One of the most important messages from this study was that the anchoring of maghemite on a carbon support could stabilize the non-stable maghemite phase of Fe_2O_3 (in nanoscale). Hematite is the most stable phase of iron oxide, while maghemite is metastable and readily transforms to hematite. However both hematite and maghemite can be found in minerals as well as in nanoparticle form naturally, but it is generally accepted that a size dependent transition from maghemite to hematite occurs around 10 nm.[207] By the promoting effect of nitrogen defects, maghemite nanoparticles can however be stabilized. This had a great influence on developing our idea to synthesize a hybrid material based on maghemite and hematite nanostructures and NCNTs. Due to the difficulty of producing electrode from this type of material, we aimed to synthesize a hybrid direct electrode composite for various applications which would be compatible with up-scaling.

6.6. Advanced negative electrodes based on hybrid iron oxide/nitrogen-doped carbon nanostructures

The novel 3D electrode composite was synthesized in a self-assembly bottom-up process, and could be used directly as an electrode without adding any binder or additive. Here we describe the results from two different types of electrodes, one with the intention to stabilize the hematite phase, and one with the intention to stabilize the maghemite phase. By varying the synthesis conditions slightly (described in section 4.3) we stabilized two different phases, which were tested for different applications, either for LIBs, or for oxygen evolution reactions. I here start to describe the results obtained for the LIBs project which is based on the results presented in paper IV.[167]

6.6.1. Hierarchical NCNTs and hybrid NCNTs/hematite electrode material for LIBs

As described in detail in section 4.3, NCNTs were grown on CP substrate using the CVD method. In the next step, iron hydroxide nanorods were grown on the surface of NCNTs during a hydrothermal self-assembly process. Figures 26a and b show the SEM images of NCNTs/CP and the as synthesized material from the hydrothermal process. It was confirmed by SEM and Raman spectroscopy that the NCNTs were covered with small iron hydroxide nanorods vertically grown on NCNTs which themselves were vertically grown on fibers of CP.

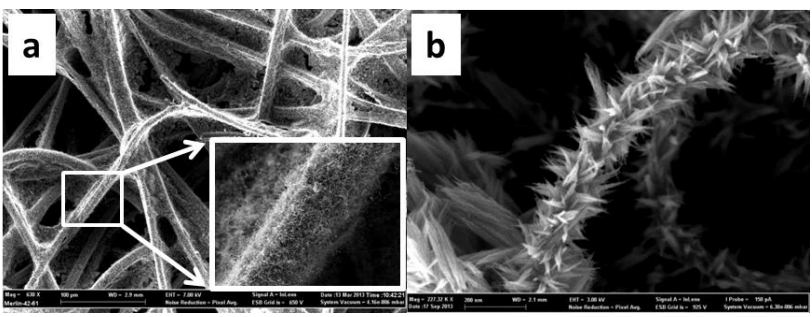

Figure 26. SEM images of a) NCNTs/CP and b) iron hydroxide nanorods/NCNTs/CP

The iron hydroxide/NCNTs/CP was then transferred to the oven and heat-treated in air at 450 °C for different time intervals (*i.e.* 10 min and 1 h) to form the hierarchical hematite nanorods (HR/NCNTs/CP). The TEM images of both iron hydroxide/NCNTs/CP and HR/NCNTs/CP are shown in figure 27. It is clear that iron hydroxide rods are formed as extremely thin needles which are aligned in bundles. After the heat treatment, by transformation of iron hydroxide into hematite the sharp needle morphology of rods are replaced by a porous, "finger-like" structure but still vertically aligned on the NCNTs. The pores, with a maximum diameter of ~4.5 nm form due the vaporization of encapsulated water which is trapped in the structure. The water is the side product of the transformation of iron hydroxide to hematite in the following reaction:

$$2FeOOH \rightarrow Fe_2O_3 + H_2O \qquad (25)$$

Figure 28 shows the Raman spectrum of HR/NCNTs/CP with the inset of the Raman spectrum of iron hydroxide/NCNTs/CP. The features in the inset spectrum match well with the Raman features of iron hydroxide.[199] Raman spectrum of HR/NCNTs/CP displays D-band and G-band at high wavenumber region which are characteristic features for NCNTs (explained

before) along with distinctive features of hematite which demonstrate the successful transformation of iron hydroxide into hematite.

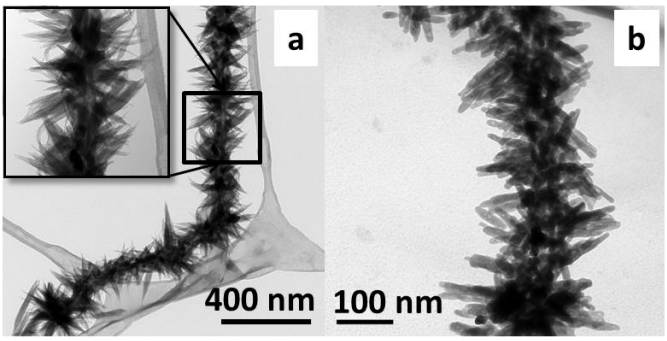

Figure 27. TEM images of a) as synthesized iron hydroxide nanorods/NCNTs/CP and b) HR/NCNTs/CP after heat treatment at 450 °C for 10 min

The features in low wavenumber region can be fitted and assigned to different vibrational modes of hematite as shown in figure 28.

The battery was then assembled and prepared for electrochemical measurements from the synthesized material. Circular electrodes with the diameter of 20 mm were punched out from their respective material. The binder-free electrodes were then embedded in Li half-cells and vacuum-sealed in polymer laminated aluminum pouches (*i.e.* 'coffee bags'). A Li foil was used as a combined reference and counter electrode and a 1 M solution of $LiPF_6$ in ethylene carbonate and diethyl carbonate (EC:DEC) mixture solution were used as electrolyte. The results obtained from cyclic voltammetry (CV) analysis on blank CP, NCNTs/CP and hierarchical HR/NCNTs/CP formed after 10 min and 1 h at 450 °C are shown in figures 29a-d. Measurements were conducted on the various electrodes at 0.05 mV/s between 0.05 and 3.0 V *vs.* Li^+/Li. It is clear from figure 29a that CP itself is electroactive and exhibits the typical red-ox features below 1.2 V *vs* Li^+/Li. The peaks marked as 'o' in all the plots is related to formation of solid-electrolyte interface (SEI) layer which appears in the first phase of cycling. As can be seen in figure 29b-d, the overall charge stored upon

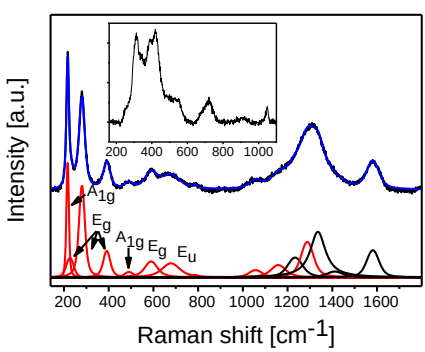

Figure 28. Raman spectrum of HR/NCNTs/CP with the assigned peaks to hematite vibrational modes, inset) Raman spectrum of as synthesized iron hydroxide/NCNTs/CP

lithiation/delithiation increases by inclusion of NCNTs and additional hematite nanorods.

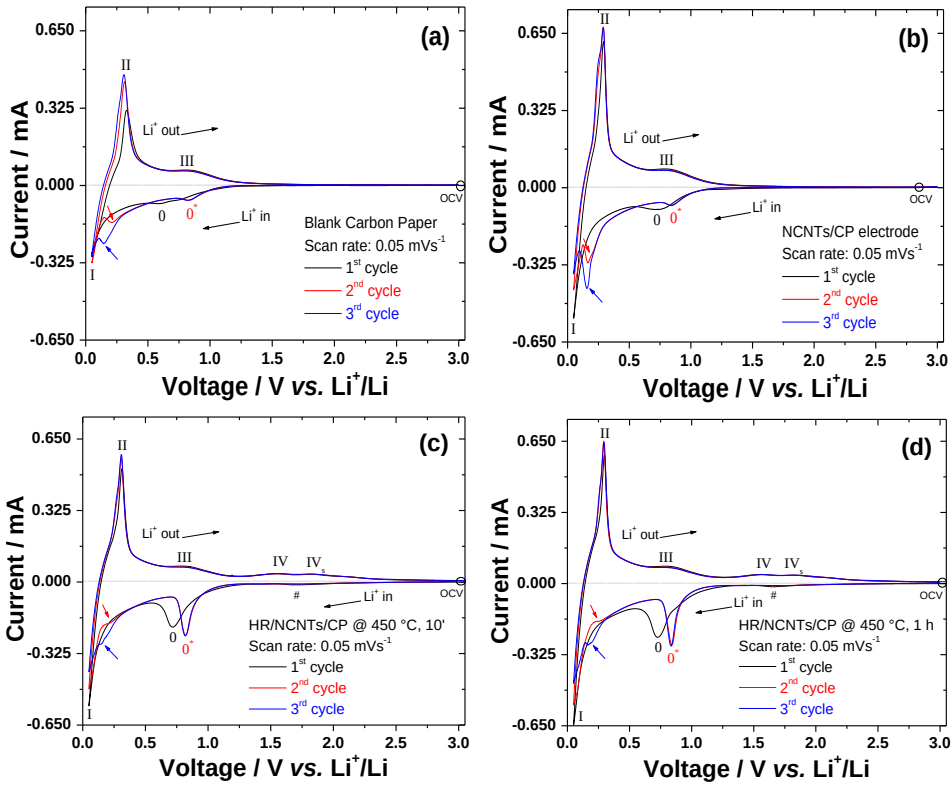

Figure 29. Cyclic voltammograms of a) blank CP substrate, b) NCNTs/CP electrode, c) HR/NCNTs/CP hierarchical structure resulting from a thermal treatment of 10 min at 450 °C and d) HR/NCNTs/CP electrode obtained after 1 h at 450 °C scanned between 0.05 and 3.0 V *vs.* Li^+/Li with a sweep rate of 0.05 mVs^{-1}

The coulombic efficiencies calculated from the areas of the respective anodic/cathodic curves in the first cycle of the different electrodes yield 83% for the CP, 87% for the NCNTs/CP, and 80% and 74% for the HR/NCNTs/CP grown with different annealing times of 10 min and 1 h. This shows that the charge recovery upon first cycling is significant in the presence of NCNTs. By comparing the CV cycles of HR/NCNTs/CP structures with those of the carbonaceous electrodes, two extra oxidative features can be noticed (denoted by IV and IV_s) which are attributed to the sequential oxidation of $Fe^0 \rightarrow Fe^{2+} \rightarrow Fe^{3+}$.[208-209] It is clear from figure 29 that the shape and intensity of the reduction peak at around 0.2 V (assigned by coloured arrow) is more pronounced for NCNTs/CP electrode which is shown to be associated to progressive Li storage in the inter-wall space of NCNTs.[159] The charge storage contribution associated to the conversion

mechanism in the hierarchical structures can be seen clearly in figure 30, when the same electrodes are subjected to successive cycles at increasing scan rates. It is clear that the electrochemical response of HR/NCNTs/CP electrode becomes more evident at higher scan rates implying a more efficient charge storage capability.

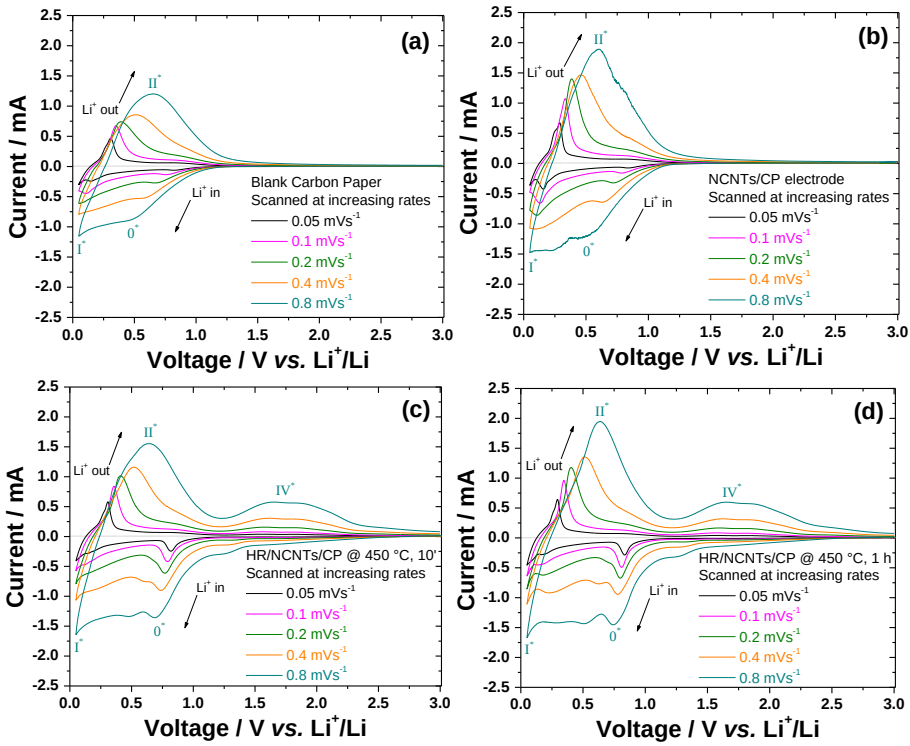

Figure 30. Cyclic voltammograms of the various electrodes scanned between 0.05 and 3.0 V *vs.* Li^+/Li at increasing sweep rates

We studied the possible performance limitation of our electrodes. According to the Ohm's law, if an *IR*-drop is associated with the electrochemical system, a linear relationship between the peak potential (E_p) and the scan rate is expected.[210] Since for all electrodes, the red-ox related peak potentials show linear relationship with the applied scan rates (square root of scan rate), we conclude that the charge transfer is the main limiting step in the process. The mechanism of conversion reactions on different electrodes was then studied further. We noticed that the peak current (I_p) behaves differently on pure carbonaceous and hybrid material based electrodes. For instance the absolute value of cathodic peak labelled by 'O^*' is

linearly proportional to the scan rate for both CP and NCNTs/CP but linearly proportional to square root of the sweep rate for HR/NCNTs/CP electrodes.

This shows that the reduction reaction (Li^+ insertion) on CP and NCNTs is a surface controlled process and occurs under electrochemical condition.[210-211] On the other hand, the reduction mechanism for HR/NCNTs/CP electrodes is limited by diffusion, as indicated by the characteristic dependence of the current to the reciprocal of the square root of time. In addition, we subjected our electrodes to galvanostatic measurements at a constant current density of 0.3 mA/cm^2. The voltage profiles of discharge (solid lines) and charge (dotted lines) for NCNTs/CP, HR/NCNTs/CP treated at 450 ºC for 10 min and 1 h are shown in figure 31a-c.

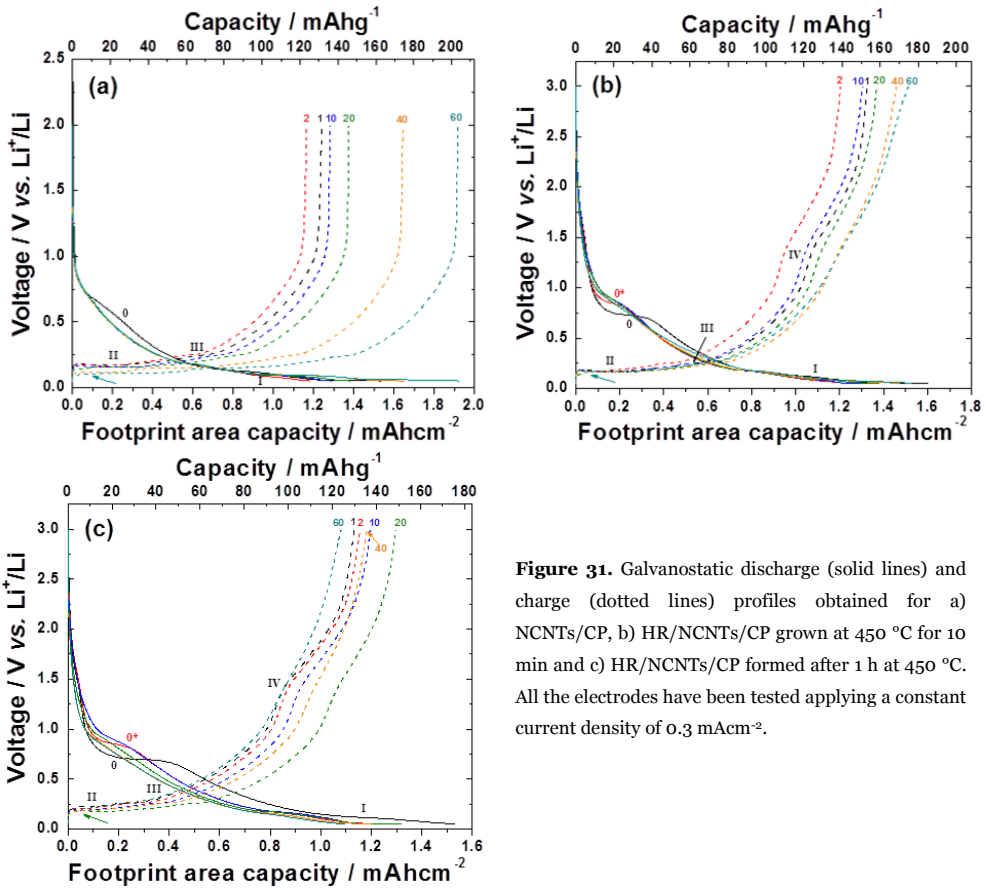

Figure 31. Galvanostatic discharge (solid lines) and charge (dotted lines) profiles obtained for a) NCNTs/CP, b) HR/NCNTs/CP grown at 450 °C for 10 min and c) HR/NCNTs/CP formed after 1 h at 450 °C. All the electrodes have been tested applying a constant current density of 0.3 mAcm^{-2}.

The coulombic efficiency for the first discharge/charge cycle is 82.0% for the NCNTs/CP, whereas it is 82.3% and 74.0 % for the HR/NCNTs/CP heat treated for 10 min and 1 h, respectively. The energy efficiencies of the first charge/discharge cycle are calculated from the associated curves and are 81.2% for NCNTs/CP, 64.3% for HR/NCNTs/CP heat treated for 10 min and

64.4% for the electrode heat treated for 1h. It is clear that continuous formation of Fe/Li_2O nanocomposite and the regeneration of Fe_2O_3 nanostructures in HR/NCNTs/CP electrodes require higher energy compare to the energy needed for the conversion reaction in NCNTs/CP.

The footprint area capacities of NCNTs/CP increase upon progressive cycling up to about 1.95 $mAhcm^{-2}$ (i.e. ≈204 $mAhg^{-1}$ referring to the mass of the entire electrode) after 60 cycles with an excellent coulombic efficiency. The discharge and charge capacities rise well beyond their initial values as a result of the defects induced by the nitrogen doping, which gradually open the way to the additional Li storage in the inter-wall regions of NCNTs. In the case of HR/NCNTs/CP electrodes, the trend of capacity with increasing the cycle's number differs significantly. The capacity increases by cycling for HR/NCNTs/CP treated for 10 min and reaches to a maximum of 1.54 $mAhcm^{-2}$ (e.g. ≈175 $mAhg^{-1}$ referred to the mass of the entire electrode) after 60 cycles. For HR/NCNTs/CP heat treated for 1 h, a charge loss was observed after a preliminary capacity enhancement during the first 20 cycles. The evolution of discharge/charge capacities on various electrodes are summarized in figure 32. The initial good performance of the CP starts fading after 35 cycles while it is clearly deviating from any charge losses for NCNTs/CP and the HR/NCNTs/CP with the shorter thermal treatment.

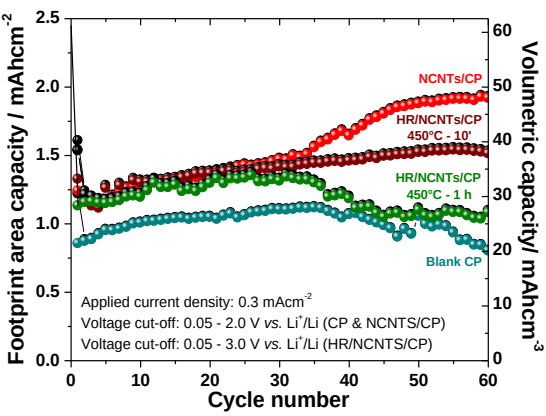

Figure 32. Cycle performance of various electrode structures upon galvanostatic cycling at 0.3 $mAcm^{-2}$.

The capacity evolution follows different paths for HR/NCNTs/CP with different treatment conditions. While capacity rises continuously for HR/NCNTs/CP with shorter treatment, it fades significantly after 35 cycles for HR/NCNTs/CP with longer treatment. It is plausible that this can be related to a difference in crystallinity of these materials due to the different thermal treatment conditions. By analysing the hematite related Raman features of two materials, we realized that the crystal domain size increases by prolongation of the heat treatment. Since the conversion mechanism

implies a radical change of the structure and the size of the hematite during the early stages of forming Fe/Li_2O nanocomposite, it is reasonable that hematite needles with smaller crystal domain size undergo these reactions in a more constructive way.

The design of HR/NCNTs/CP structures is suitable for boosting the surface reactivity of the resulting materials for applications such as supercapacitors in which the conversion reactions are not involved and the larger surface areas provided by the hierarchical structures can be exploited.

6.6.2. Hierarchical hybrid NCNTs/maghemite electrode material for electrochemical water oxidation

In this section, I describe the work associated by developing a novel electrocatalyst for oxygen evolution reaction (OER) which can be then wired to a PV cell. This is based on the results presented in paper V. We design the direct electrode material based on hybrid maghemite/NCNTs to avoid using noble metal oxides, such as IrO_2 and RuO_2. In addition, by the synthesis of nanorods instead of nanoparticles we maximized the electrocatalytic surface area and by directly integrating the electrocatalyst to the current collector the overall resistance from the reaction site to the current collector was minimized. The direct electrode material was synthesized in a similar method reported for HR/NCNTs/CP explained in 5.6.1. The only difference was the last and most crucial step which was the heat treatment step as described in section 4.3.

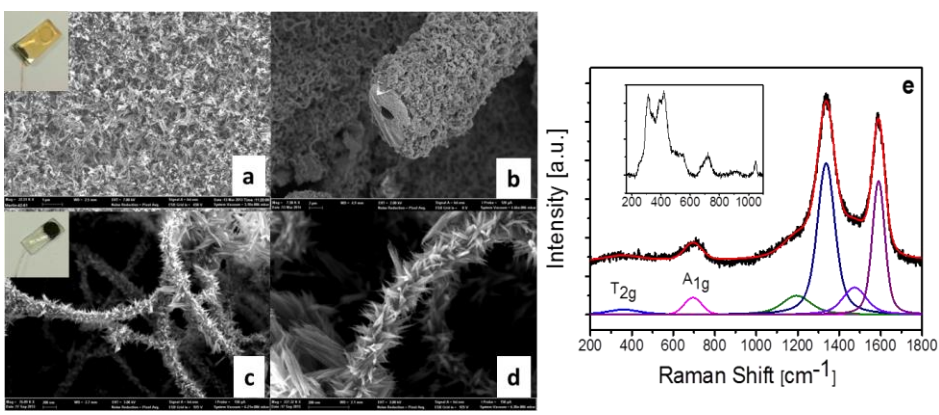

Figure 33. TEM images of a) vertically grown maghemite nanorods on FTO (MR@FTO), b) cross section of one of the fibers of CP after the growth of maghemite nanorods on NCNTs (MR@NCNTs/CP), c) high magnification of iron hydroxide nanorods vertically grown on each NCNTs, d) the same material as (c) after heat treatment in air at 350 °C for 15 min, insets: assembled electrodes out of their respective materials and e) Raman spectrum of MR@NCNTs/CP, inset: as synthesized material before heat treatment

To stabilize the maghemite phase, as grown iron hydroxide@NCNTs/CP was heat treated in air at 350 °C for only 15 min and the resulting material was called MR@NCNTs/CP. For comparison the maghemite nanorods was grown on CP (MR@CP) and fluorine doped tin oxide coated glass (FTO glass-MR@FTO) in a similar synthesis condition.

Figures 33a-d display SEM images of MR@FTO and MR@NCNTs/CP before and after heat treatment with an inset of the fabricated electrode for electrochemical testing. It is clear from SEM images that the same morphology as hematite nanorods (see figure 26b) is achieved by a shortened heat treatment. The Raman spectra of the as synthesized iron hydroxide@NCNTs/CP and MR@NCNTs/CP are shown in figure 33e. Beside the nitrogen-doped carbon nanotubes related features at high wavenumber region (explained before),[166] two distinct features are assigned to the T_{2g} and A_{1g} vibration modes of maghemite[198] which confirms the successful phase transformation to maghemite. The electrocatalytic OER activity of MR@NCNTs/CP as a direct electrode was investigated in 0.1 M KOH solution in a standard three electrode system. The electrocatalytic performance of this electrode was compared with bare CP, NCNTs/CP, MR@CP and MR@FTO. As shown in figure 34a, while CP shows small electrocatalytic OER activity addition of either NCNTs or MR has a significant effect on both the onset potential for OER and the current density (see table 2).

Table 2. The calculated values from CV measurements for bare CP, NCNT/CP, MR@CP, MR@NCNTs/CP and MR@FTO electrodes scanned at 2 mV/s in 0.1 M KOH solution

Electrode	Onset potential (V *vs.* RHE)	Overpotential (V)	Tafel slope (mV/dec)	Exchange current density (j_0-A/cm^2)
CP	1.74	0.51	318	6.7×10^{-5}
NCNTs/CP	1.68	0.45	153	8.5×10^{-4}
MR@FTO	1.622	0.392	53	1.2×10^{-8}
MR@CP	1.596	0.366	60	1.8×10^{-8}
MR@NCNTs/CP	1.576	0.346	53	2.1×10^{-7}

In a 0.1 M KOH solution at MR@NCNTs/CP electrode, OER starts at 1.576 V *vs.* RHE corresponding to an overpotential of only 0.346 V and a current density of 10 mA/cm^2 is obtained at an overpotential of 0.73 V which is comparable to the reported undoped state-of-the art OER electrocatalysts.[212,213, 116,214] To be able to explain the obtained high current density and low onset potential, we synthesized the same MR nanorods on only CP (without NCNTs) and FTO glass. From Figure 34a it is clear that by replacing the FTO with CP, a slightly better electrode characteristic is gained with a higher current density and a reduced overpotential. Based on these

observations we believe that the high current density is achieved due to a combined effect of a very large surface area for the MR@NCNTs/CP electrode and the firm anchoring of the MR to the NCNTs/CP electrode.

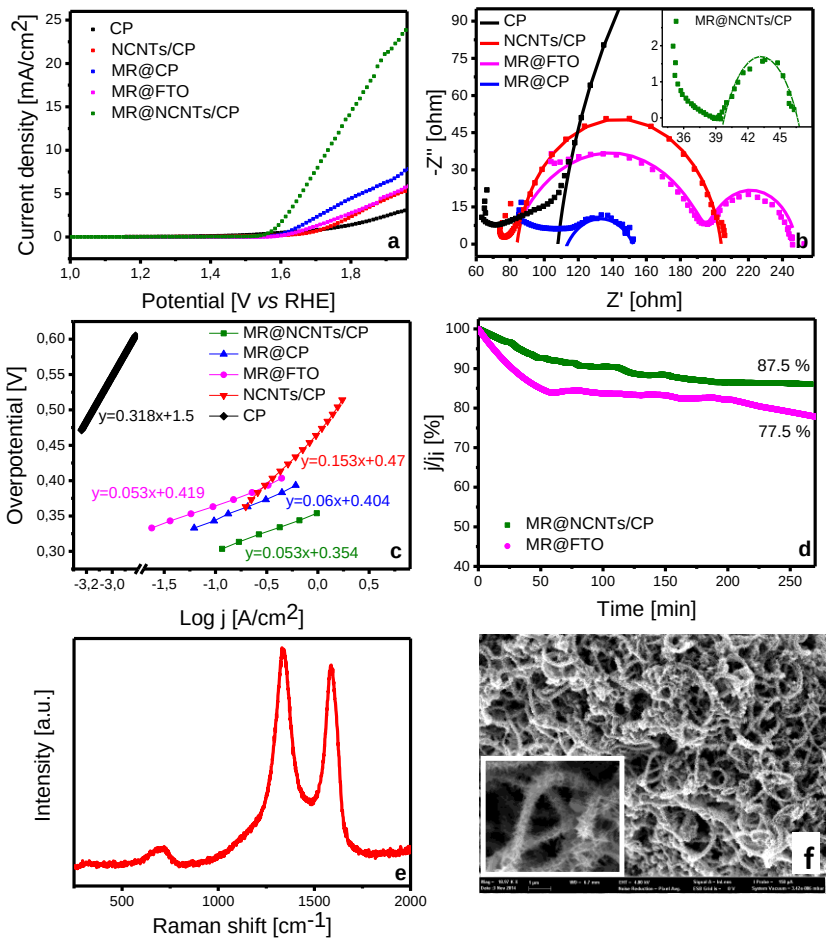

Figure 34. a) Polarization curves of bare CP, NCNT/CP, MR@CP, MR@NCNTs/CP and MR@FTO electrodes scanned at 2 mV/s in 0.1 M KOH solution, b) Electrochemical impedance spectroscopy (EIS) of CP and FTO supported electrode materials recorded at a dc potential of 1.789 V, with the EIS of MR@NCNTs/CP shown in the inset c) Tafel plots of the electrodes, d) Chronoamperometric measurement of MR@NCNTs/CP and MR@FTO shown as the normalized current density (to the initial current density) e) Raman spectrum of MR@NCNTs/CP electrode after being used in the stability test for 16000 s, and f) SEM image of MR@NCNTs/CP after electrochemical testing.

Additionally, we studied the charge transfer characteristics of our electrodes by conducting electrochemical impedance spectroscopy (EIS). The EIS data in the form of Nyquist plots are presented in figure 34b. The

Nyquist plots are fitted by equivalent electrical circuit models shown in Table 3.

Table 3. The EIS data derived by fitting using equivalent electrical circuit models

Electrode	Equivalent circuit model	R_s	R_{ct}	α	R_2	α_2
CP	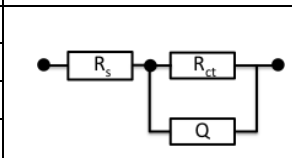	108	498	0.9	-	-
NCNTs/CP		84	120	0.89	-	-
MR@CP		113	40	0.65	-	-
MR@NCNTs/CP		39	8	0.7	-	-
MR@FTO	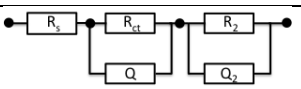	79	115	0.7	52	0.83

The oxygen evolution reaction occurs at the MR||electrolyte solution interface,[215] and is usually associated with the largest resistance (R_{ct}). R_{ct} is represented by the diameter of the semicircle in Nyquist plot. The values of R_{ct} for each of the electrodes are presented in Table 3. As can be seen in figure 34b, at an applied dc potential of 1.789 V *vs.* RHE which is 0.56 V above the water oxidation potential only one frequency-dependent segment is observed for CP based electrodes (all electrodes except MR@FTO). A significantly smaller R_{ct} is established on MR@NCNTs/CP electrode with a diameter of the semicircle in Nyquist plot being only 8 Ω (compare to that of NCNTs/CP and MR@CP electrodes being 120 Ω and 40 Ω). This highlights the beneficial outcome of our idea to replace the common FTO glass substrate by carbon paper which not only improve the performance but also make the handling and up-scaling easier.

The kinetics of OER was further investigated by studying the Tafel plots. As explained in section 3.1.1, for irreversible reactions there is a potential region (Tafel region) where the current density is exponentially dependent on overpotential. The slope (β_A) of the Tafel plot (overpotential *vs.* log j) gives valuable information about the kinetics of the electrochemical reaction.

The Tafel slopes in the order of 50-60 mV/dec was calculated for all MR loaded electrodes which are much lower than those calculated for CP and NCNTs/CP (see table 2 and figure 34c). The extracted exchange current density for MR@NCNTs/CP has the highest value between the MR loaded electrodes which indicates a better OER kinetics on this electrode. Finally, the chronoamperometric response of MR loaded electrodes were recorded at 1.71 V for 16000 s (see figure 34d). It is clear that while both MR@NCNTs/CP and MR@FTO show an initial decay of current density, the degree of decay is much lower for the MR@NCNTs/CP. The SEM and Raman spectroscopy (see figure 34e and f) confirm the morphology and phase stability of MR on the surface of NCNTs after being cycled for 16000 s.

6.7. Bifunctional 3D electrode for efficient water electrolysis in alkaline medium

Continuing our journey to build a PV-driven water electrolysis cell, in our last step we tried to develop a bifunctional electrocatalyst which can efficiently catalyze both OER and HER in the same medium. Co_3O_4 have been studied as an electrocatalyst with high stability for OER in alkaline condition.[147, 216-217] Also some studies have been reported for HER in alkaline media, but then usually for Co_3O_4 in composite form.[218-219] However, hybrid material based on Co_3O_4 for HER and OER have not been considered widely, some few studies focusing on such a material have shown a great potential to increase current density and reduce overpotential. Hence, in paper VI we aimed for the synthesis of a bifunctional 3D electrode based on NCNTs and Co_3O_4. We tried to follow our already tested successful approach to anchor the active material to the electrode surface to achieve an optimum interconnection of the active material and current collector in order to minimize the resistive loses (contact resistance) in the device.[3] The Co_3O_4@NCNTs/CP direct electrode was synthesized as described in section 4.4. Figure 35a and b show the SEM images of the synthesized Co_3O_4@NCNTs/CP. A good coverage of electrode surface with Co_3O_4 nanospheres (figure 35a) and an excellent interconnection of the different components (figure 35b) are achieved by following the synthesis procedure (explained in section 4.4).

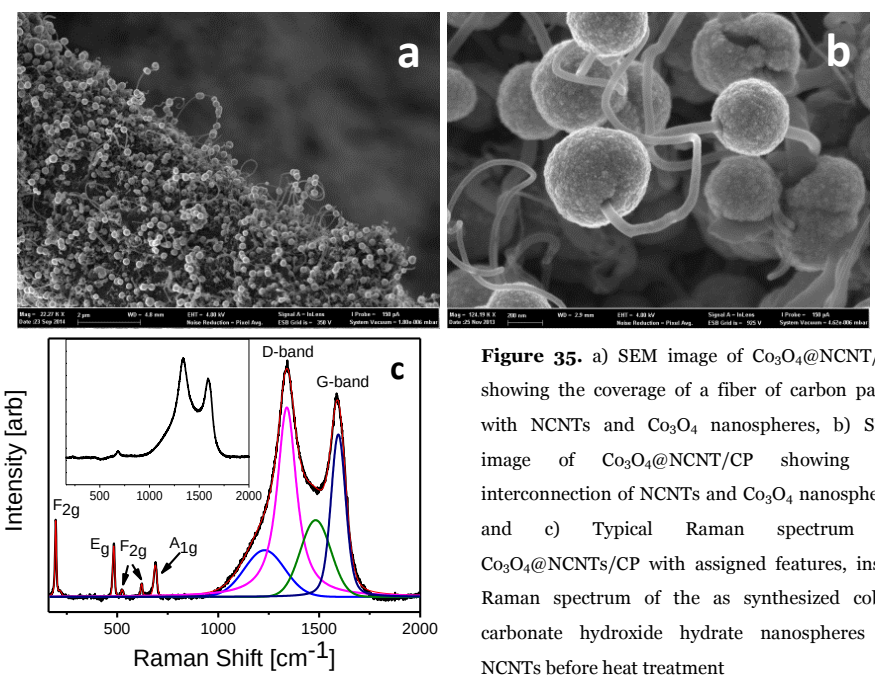

Figure 35. a) SEM image of Co_3O_4@NCNT/CP showing the coverage of a fiber of carbon paper with NCNTs and Co_3O_4 nanospheres, b) SEM image of Co_3O_4@NCNT/CP showing the interconnection of NCNTs and Co_3O_4 nanospheres and c) Typical Raman spectrum of Co_3O_4@NCNTs/CP with assigned features, inset) Raman spectrum of the as synthesized cobalt carbonate hydroxide hydrate nanospheres on NCNTs before heat treatment

Raman spectroscopy proved the successful transformation of as synthesized material (inset of figure 35c) to Co_3O_4. Figure 35c shows a typical Raman spectrum of Co_3O_4@NCNTs/CP in which the features in the low wave number region of the spectrum match well with the characteristic features of Co_3O_4. To assess sufficient information about the mass transport efficiency of our electrode, a test electrode was prepared for comparison. In a similar synthesis procedure NCNTs were grown by CVD in the powder form (described in section 4.1) and in a similar hydrothermal process and post treatment, Co_3O_4 nanospheres were formed on NCNTs but in the absence of CP substrate.

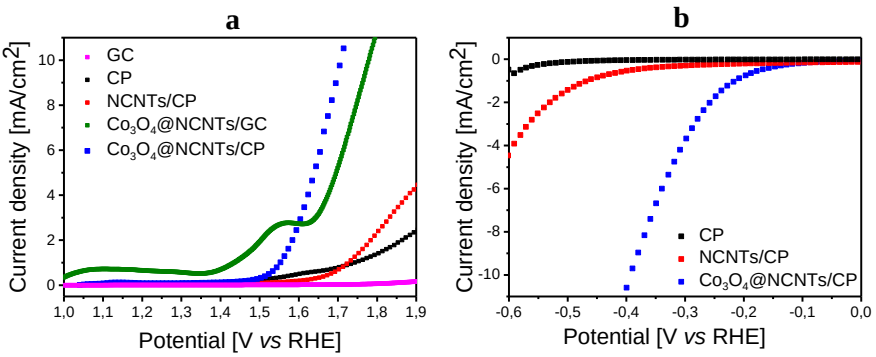

Figure 36. a) OER characteristics recorded for bare CP (carbon paper), NCNTs/CP, Co_3O_4@NCNTs/CP compared with GC (glassy carbon) and Co_3O_4@NCNTs modified GC electrodes and b) HER characteristics of CP, NCNTs/CP and Co_3O_4@NCNTs/CP in 0.1 M KOH

Following the previous reports, this material then loaded on glassy carbon electrode (Co_3O_4@NCNTs/GC) and then its electrochemical performance was tested and compared with the same material when directly anchored on CP substrate. The OER characteristic of Co_3O_4@NCNTs loaded on both CP and GC in 0.1 M KOH solution are shown in figure 36a and compared with the metal free electrodes including; CP, GC and NCNTs/CP. The OER response of these electrodes along with the catalyst loading extracted from TGA are summarized in table 4. It is interesting to note that in 0.1 M KOH solution Co_3O_4@NCNTs/CP displays a current density of 10 mA/cm^2 at an overpotential of 0.47 V while Co_3O_4@NCNTs/GC requires an overpotential of 0.54 V to reach a current density of 10 mA/cm^2. The better performance of Co_3O_4@NCNTs/CP become even more interesting by considering that the catalyst loading on this electrode is 4-fold lower than that on Co_3O_4@NCNTs/GC.

Table 4. Calculated values from CV and TGA measurements for bare CP, NCNTs/CP, Co_3O_4@NCNTs/CP and Co_3O_4@NCNTs/GC electrodes

Electrode	OER onset potential (V vs RHE)	η_{OER} at 10 mA/cm² (V)	Co_3O_4 loading (mg/cm²)
CP	1.75	-----	0
NCNTs/CP	1.71	-----	0
Co_3O_4@NCNTs/GC	1.62	0.54	0.16
Co_3O_4@NCNTs/CP	1.57	0.47	0.04

The linear sweep voltagramms (LSV) in figure 36b show the electrocatalytic HER activity of Co_3O_4@NCNTs/CP directly after being tested for OER in the same 0.1 M KOH electrolyte solution. It can be easily seen that, anchoring Co_3O_4 nanospheres on the surface of NCNTs results in a bifuctional electrode material with an excellent HER activity at an onset potential of -0.26 V *vs*. RHE. Our Co_3O_4@NCNTs/CP electrode needs an HER overpotential of only 0.38 V to reach a current density of 10 mA/cm². These results are an important final step towards the fabrication of electroactive electrode for large scale production of PV-driven water electrolysis cell.

7. Conclusion and outlook

The main aim of this thesis work was to develop electrocatalytic active carbon based nanostructures for energy conversion and storage applications. This work gives insight to the structure and properties of nitrogen-doped carbon nanostructures (nanotubes and reduced graphene oxide) and their application in electrode fabrication. The electrocatalytic activity of nitrogen-doped carbon nanotubes (NCNTs) based electrodes combined with transition metal oxides (TMOs) were tested for different electrochemical processes from Li-ion microbatteries to water electrolysis.

The first part of the work, presented as **paper I** and main part of **paper II**, concentrated on configuration of nitrogen functionalities in NCNTs. The main focus lied on the behavior of nitrogen functionalities regarding the nitrogen content and their assignment based on the X-ray photoelectron spectroscopy (XPS). XPS is the main tool in configuration of nitrogen functionalities in nitrogen containing structures. Due to close binding energies, the precise assignment of different functionalities from nitrogen peak in XPS spectrum is still a matter of debate. Interestingly, the electrocatalytic activity of nitrogen-doped carbon nanostructure strongly depends on the type of nitrogen functionality. Configuration of the most electrocatalytic active nitrogen site for oxygen reduction reaction (ORR) was investigated in the second part of **paper II**. To this, we used a different approach compared to previous studies. Instead of trying to synthesize NCNTs with different majority of nitrogen types, we started from one batch of sample and transformed particular nitrogen functionalities to others by tuning the treatment condition. In this way different "hidden" parameters which may affect the catalytic activity was reduced and the effects could be traced to the influence of only the nitrogen type.

The first attempt to synthesize a hybrid novel structure based on nitrogen-doped carbon nanostructure and maghemite (γ-Fe_2O_3) nanoparticles is presented in **paper III**. Nitrogen-doped graphene nanoscrolls were synthesized and the rolling mechanism was studied both experimentally and by using *ab initio* calculations. We concluded that, the nanoscrolls form as a combined result of magnetic interaction between the maghemite nanoparticles and a strong interaction of maghemite nanoparticles with nitrogen functionalities at the graphene sheets. We believe that this structure might be a good candidate for energy storage applications due to the appropriate layer spacing of nanoscrolls with the additional presence of iron oxides. However, due to mass inefficiency of the synthesis process we could not test this material in real application.

We then realized that the electrode fabrication is sometimes more important than that the material synthesis itself, if a real application is a goal. So from hereafter we changed our path and tried to synthesize our

electrocatalytic material directly on the surface of electrode (current collector). This opens up for up-scaling the product and also increases the efficiency per weight of active material. We introduced the synthesis route to a 3D structure relying on NCNTs and hematite nanorods in **paper IV**. NCNTs were directly grown on the carbon paper such that each fiber of carbon paper was covered with vertically aligned NCNTs. This electrode was tested directly as an advanced negative electrode in Li-ion micobattery without any further modification or any use of binders. The results were then compared with cycling performance of a similar electrode with additional hematite (α-Fe_2O_3) nanorods. Hematite nanorods were grown directly on each NCNT giving a high surface area comprising a tree-like structure. High footprint area capacities of 2.1 $mAhcm^{-2}$ and 2.25 $mAhcm^{-2}$ at 0.1 $mAcm^{-2}$ were obtained at NCNTs and hematite nanorods decorated NCNTs electrodes. However, the coulombic and energy efficiencies were much higher for NCNTs electrode.

We moved on with the same approach in the synthesis of electroactive material directly anchored on the electrode surface. With the same morphology as introduced in paper IV, we introduced maghemite as an electrocatalytic active material for oxygen evolution reaction (OER) in **paper V**. The electrode was fabricated in a similar condition but instead, the gamma phase of iron oxide (maghemite) was stabilized by changing the final heat treatment condition. By electrochemical testing of our direct electrode, we showed a good electrochemical performance at a low overpotential for OER. This was explained by the efficient electrochemical process on the surface of the maghemite nanorods due to the high surface area of the 3D electrode. To our knowledge this is the first demonstration of using maghemite as electrocatalyst for OER. Additionally, we show that the firm anchoring of each active component facilitates an efficient charge transport from the surface of the maghemite rods to the carbon paper current collector, which is an important finding for the engineering of practical electrodes.

We then tried to focus on the development of a bifunctional electrocatalyst to catalyze both water electrolysis half reactions (OER and HER) in the same electrolyte following the same approach as before. Our candidate was again a transition metal oxide but this time cobalt oxide (Co_3O_4) was chosen. We synthesized Co_3O_4 nanospheres which are anchored on NCNTs which were themselves grown on the current collector. In **paper VI** we presented the bifunctional catalytic activity of this material. Our introduced electrode needs an HER overpotential of only 0.38 V and an OER overpotential of 0.47 V to reach a current density of 10 mA/cm^2.

With the knowledge we gained from every component of our material we believe that the developed structure relying on NCNTs directly grown on carbon paper can be a candidate for future energy conversion technology.

For hydrogen production technology, the nature of the hybrid material can be modified further to reduce the overpotential of electrochemical reaction. Doping with a guest element such as Ni can be an excellent approach. In addition, double coating to increase the catalyst loading as well as the surface area, can be considered. We foresee that the assembly of a complete PV-driven artificial photosynthesis cell can be realized based on the achievements presented in this thesis.

8. Summary of appended articles

Paper I: Nitrogen doped multi walled carbon nanotubes produced by CVD-correlating XPS and Raman spectroscopy for the study of nitrogen inclusion
T. Sharifi, F. Nitze, H. R. Barzegar, C.W. Tai, M. Mazurkiewicz, A. Malolepszy, L. Stobinski, T. Wågberg, Carbon 2012, 50 (10), 3535-3541.

Contribution: all experimental results, Raman spectroscopy, electron microscopy measurements excluding HRTEM and SEM, analysis and manuscript preparation.

In this study, nitrogen doped carbon nanotubes (NCNTs) were successfully synthesized using pyridine as the single C/N precursor in chemical vapour deposition (CVD) method. The growth parameters such as growth duration and temperature were tuned to find the optimum condition. The presence and abundance of nitrogen functionalities in different samples were studied by X-ray photoelectron spectroscopy (XPS). Specifically the atomic concentration of pyridinic and pyrrolic nitrogen sites in NCNTs at different nitrogen contents was investigated. These results were correlated with the Raman spectra of samples with different contents of nitrogen. The overall trend of pyridinic-N/pyrrolic-N (atomic concentration ratio from XPS) showed a similar behavior to the I_D/I_G (integrated area ratio of D-band to G-band from Raman spectroscopy). The simultaneous transition of these ratios around 5% suggests a dissimilar nitrogen incorporation mechanism at higher nitrogen levels compared to at lower nitrogen levels.

Paper II: Formation of active sites for oxygen reduction reaction by transformation of nitrogen functionalities in nitrogen-doped carbon nanotubes
T. Sharifi, G. Hu, X. Jia, and T. Wågberg, ACS Nano 2012, 6 (10), 8904-8912.

Contribution: material synthesis, Raman spectroscopy, analysis and interpretation of XPS results and manuscript preparation.

In this study, we tried to interpret carefully the XPS results of nitrogen-doped carbon nanotubes (NCNTs) to assign the deconvoluted N 1s peaks to corresponding nitrogen functionalities. By this, we aimed to investigate the catalytic nitrogen active sites for oxygen reduction reaction (ORR). To have a better control over those parameters which may influence the catalytic activity, instead of changing the growth parameter to achieve various nitrogen functionalities in the NCNTs, we tried to transform nitrogen functionalities in already synthesized sample. The nitrogen functionalities

transformation was achieved with a simple high temperature treatment in argon environment. In the next step, by correlating XPS data with electrochemical measurements, we conclude that certain types of quaternary nitrogen, N-Q_{valley} located at the edge of graphene planes, exhibit the highest catalytic ORR activity.

Paper III: Formation of nitrogen-doped graphene nanoscrolls by adsorption of magnetic γ-Fe_2O_3 nanoparticles
T. Sharifi, E. Gracia-Espino, H.R. Barzegar, X. Jia, F. Nitze, G. Hu, P. Nordblad, C.W. Tai, T. Wågberg, Nature Communications 2013, 4.

Contribution: all experimental results, Raman spectroscopy, TEM except HRTEM, analysis and interpretation of XPS results and manuscript preparation.

In this study, nitrogen-doped graphene nanoscrolls (N-rGO_x) was synthesized by adsorption of magnetic maghemite (γ-Fe_2O_3) nanoparticles onto reduced graphene oxide sheets. A simple reflux method at a moderate temperature was employed and rolling was achieved by tuning the solvent condition. Only the condition leading to formation of maghemite nanoparticles (instead of hematite α-Fe_2O_3) during reflux resulted in the formation of nanoscrolls. This experimental observation in combination with magnetization measurements showing stronger magnetization for maghemite nanoparticles compared to hematite emphasized the key role of magnetic interaction of nanoparticles which was further confirmed by *ab initio* calculations. In addition, the strong interaction of maghemite nanoparticles with nitrogen functionalities at the graphene sheets was shown to have a major impact on the success of an efficient rolling process. In line with our proposed model, the rolling process was completely reversible and upon removal of maghemite nanoparticles the nanoscrolls returned back to their original structure.

Paper IV: Hierarchical self-assembled structures based on nitrogen-doped carbon nanotubes as advanced negative electrodes for Li-ion batteries and 3D microbatteries
T. Sharifi[*], M. Valvo[*], E. Gracia-Espino, R. Sandström, K. Edström, T. Wågberg ([*]authors equally contributed to the manuscript), Journal of Power Sources 279 (2015) 581-592

Contribution: material synthesis, Raman spectroscopy, TEM, analysis and interpretation of XPS results and manuscript preparation.

A hierarchical self-assembled structure based on nitrogen-doped carbon nanotubes (NCNTs) was directly synthesized on the electrode surface (carbon paper) and tested as negative electrodes for Li-ion microbatteries. This structure was further functionalized with hematite nanorods attached on their outer walls. The electrochemical behavior and the footprint area capacities of these 3D architectures were also investigated to probe their applicability in Li-ion microbatteries. NCNTs showed excellent coulombic and energy efficiencies and footprint area capacities as high as 2.1 $mAhcm^{-2}$ at 0.1 $mAcm^{-2}$ after 20 cycles and up to 1.95 $mAhcm^{-2}$ after 60 cycles at 0.3 $mAcm^{-2}$. On the other hand, hematite nanorods modified NCNTs displayed footprint area capacity up to 2.25 $mAhcm^{-2}$ at 0.1 $mAcm^{-2}$. However, their coulombic and energy efficiencies were not as good as NCNTs electrode. This is due the difference in the nature of conversion reaction occurring in these two structures. A continuous rearrangement of the phase boundaries in hematite structures causes progressive electrochemical milling which lowers the efficiencies.

Paper V: Efficient electrochemical water oxidation by maghemite nanorods anchored on a 3D nitrogen-doped carbon electrode
T. Sharifi, W.L. Kwong, H-M Berends, C. Larsen, J. Messinger, T. Wågberg, submitted

Contribution: material synthesis, Raman spectroscopy, electron microscopy (TEM & SEM), analysis and interpretation of XPS results, part of electrochemical testing and manuscript preparation.

In this study we tested a 3D electrode for oxygen evolution reaction (OER), comprising maghemite nanorods firmly anchored to nitrogen-doped carbon nanotubes (NCNTs). The electrocatalytic OER activity of the synthesized direct electrode was investigated in 0.1 M KOH solution. Our measurements demonstrated that at a current density of 1 $mAcm^{-2}$ an overpotential of only 362 mV is needed for OER, which is comparable to state-of-the art non-doped OER electrocatalysts. The electrochemical impedance spectroscopy (EIS) measurements revealed an excellent interfacial charge transfer which is due to firm anchoring of each active component. As a result, a good stability was achieved on our electrode compared to common deposited transition metal oxides on FTO glass which is a common conducting support in electrochemical testing.

Paper VI: Earth-abundant bifunctional 3D electrode for efficient water electrolysis in alkaline medium
Tiva Sharifi, Xueen Jia, Robin Sandström, Thomas Wågberg, Submitted

Contribution: all experimental results, Raman spectroscopy, electron microscopy (SEM), electrochemical testing and manuscript preparation.

In this study we developed a 3D bifunctional electrode for catalyzing both water electrolysis half reactions (OER and HER) in the same medium of 0.1 M KOH electrolyte solution. In the similar approach as before our catalyst nanostructure was self-assembled on the surface of nitrogen-doped carbon nanotubes (NCNTs) which were grown on carbon paper (CP) substrate. For efficient catalyzing the water electrolysis we used cobalt oxide (Co_3O_4) as an earth abundant material. Our electrode material firmly anchored on CP performed a high stability compared to the similar material which was drop casted on glassy carbon electrode. In addition, we observed that Co_3O_4@NCNTs/CP displays current density of 10 mA/cm^2 at overpotential of 0.47 V for OER and at overpotential of 0.38 V for HER.

9. Acknowledgements

I would like to express my gratitude to my supervisor, Thomas Wågberg, whose expertise and understanding added considerably to my graduate experience. Thank you for supporting me throughout my thesis whilst allowing me the room to work in my own way. A special thanks to my co-supervisor, Ludvig Edman for his support.

I spent most of my time in the last years at physics department with its great environment. I would like to thank all the members of physics department and express my special appreciation and thanks to Katarina Hassler, Lena Burström and Jörgen Eriksson for their welcoming and helpful attitude. I would also like to thank Lena Åström and Peter Wikström for all their patience to build the equipments that I needed. Thanks Karin Rinnefeldt for helping me to speak Swedish, I learnt a lot from you. Thank you, Hans Forsman and Gabriella Allansson for organizing patiently my teaching related issues. Krister Wiklund, thanks for all the positive energies you gave me during our discussions, I always enjoyed talking to you.

I would like to express my sincere gratitude to my colleagues in Thomas Wågberg's group; Guangzhi Hu, thanks for all the helps and collaborations and specially thanks for answering my chemistry related questions. Xueen Jia, you taught me a lot about electrochemistry, it was a pleasure working with you. Eduardo, you were not only my colleague but also a friend, I always enjoyed our scientific discussions and your great ideas. Hamid Barzegar, we started the journey of education together from bachelor to PhD, thanks for all the supports and helps, it was a great opportunity to make this journey along with you. Florian Nitze, thanks for all the details you taught me and Robin Sandström, thanks for all the helps and measurements you did for me.

I would like to thank our collaborators at Ångstöm laboratory at Uppsala University; Prof. Kristina Edström and Mario Valvo. I express my appreciation to collaborators in artificial leaf project especially Prof. Johannes Messinger and Wai Ling Kwong.

I also like to thank all those who helped me to learn different characterization techniques. Lenore Johansson, Andras Gorzsas, Cheng Choo Lee and Cheuk-Wai Tai, your vast knowledge and skill influenced a lot my understanding of many processes related to this work. Especial thanks to Andrey Shchukarev, your welcoming behavior always encouraged me to start up discussions which directly affected this work.

A very especial thanks to Christian Larsen, Amir Asadpoor, Alexandra Johansson, Amir Khodabakhsh, and Alexey Klechikov who made my teaching experience at Umeå University unforgettable.

I don't have enough words to thank my friends in Umeå; you were always with me making a warm second family during the hard times of being far from home. I would like to express the deepest appreciation to Atieh

Mirshahvalad, Narges Mortezaei, Avazeh Hashemloo, Fariba Karimi, Ramin Ghorbani, Azadeh Farshidi and Vania Colmenares.

A special thanks to my family, words cannot express how grateful I am to my mother, father and my sisters; Tina and Mina.

I dedicate this thesis to a person whose presence was the reason I could achieve this goal. Alireza, I am truly grateful for your love and support. Without you, I have not been able to balance my research with everything else. Thanks for joining me in this adventure.

And my final words, I love you Amin.

10. References

1.Walter, M. G.; Warren, E. L.; McKone, J. R.; Boettcher, S. W.; Mi, Q.; Santori, E. A.; Lewis, N. S., *Chemical Reviews* **2010,** *110* (11), 6446-6473.

2.Luo, J.; Im, J.-H.; Mayer, M. T.; Schreier, M.; Nazeeruddin, M. K.; Park, N.-G.; Tilley, S. D.; Fan, H. J.; Grätzel, M., *Science* **2014,** *345* (6204), 1593-1596.

3.Surendranath, Y.; Bediako, D. K.; Nocera, D. G., *Proceedings of the National Academy of Sciences* **2012,** *109* (39), 15617-15621.

4.McCrory, C. C. L.; Jung, S.; Peters, J. C.; Jaramillo, T. F., *Journal of the American Chemical Society* **2013,** *135* (45), 16977-16987.

5.Fabbri, E.; Habereder, A.; Waltar, K.; Kotz, R.; Schmidt, T. J., *Catalysis Science & Technology* **2014,** *4* (11), 3800-3821.

6.Reier, T.; Oezaslan, M.; Strasser, P., *ACS Catalysis* **2012,** *2* (8), 1765-1772.

7.Morozan, A.; Jousselme, B.; Palacin, S., *Energy & Environmental Science* **2011,** *4* (4), 1238-1254.

8.Bing, Y.; Liu, H.; Zhang, L.; Ghosh, D.; Zhang, J., *Chemical Society Reviews* **2010,** *39* (6), 2184-2202.

9.Daems, N.; Sheng, X.; Vankelecom, I. F. J.; Pescarmona, P. P., *Journal of Materials Chemistry A* **2014,** *2* (12), 4085-4110.

10.Etacheri, V.; Marom, R.; Elazari, R.; Salitra, G.; Aurbach, D., *Energy & Environmental Science* **2011,** *4* (9), 3243-3262.

11.Kratschmer, W.; Lamb, L. D.; Fostiropoulos, K.; Huffman, D. R., *Nature* **1990,** *347* (6291), 354-358.

12.Iijima, S., *Nature* **1991,** *354* (6348), 56-58.

13.Xiong, G.-Y.; Wang, D. Z.; Ren, Z. F., *Carbon* **2006,** *44* (5), 969-973.

14.Liu, L.; Yang, C.; Zhao, K.; Li, J.; Wu, H.-C., *Nat Commun* **2013,** *4*.

15.Lee, C. J.; Park, J., *Applied Physics Letters* **2000,** *77* (21), 3397-3399.

16.Tang, N.; Wen, J.; Zhang, Y.; Liu, F.; Lin, K.; Du, Y., *ACS Nano* **2010,** *4* (1), 241-250.

17.Nitze, F.; Abou-Hamad, E.; Wågberg, T., *Carbon* **2011,** *49* (4), 1101-1107.

18.Riedl, C.; Coletti, C.; Starke, U., *Journal of Physics D: Applied Physics* **2010,** *43* (37), 374009.

19.Novoselov, K. S.; Geim, A. K.; Morozov, S. V.; Jiang, D.; Zhang, Y.; Dubonos, S. V.; Grigorieva, I. V.; Firsov, A. A., *Science* **2004,** *306* (5696), 666-669.

20.Dresselhaus, M. S.; Dresselhaus, G.; Saito, R.; Jorio, A., *Physics Reports* **2005,** *409* (2), 47-99.

21.Reina, A.; Son, H.; Jiao, L.; Fan, B.; Dresselhaus, M. S.; Liu, Z.; Kong, J., *The Journal of Physical Chemistry C* **2008,** *112* (46), 17741-17744.

22.Matsui, K.; Inaba, A.; Oshidari, Y.; Takei, Y.; Takahashi, H.; Takahata, T.; Kometani, R.; Matsumoto, K.; Shimoyama, I. In *Mechanical properties of few layer graphene cantilever*, Micro Electro Mechanical Systems (MEMS),

2014 IEEE 27th International Conference on, 26-30 Jan. 2014; 2014; pp 1087-1090.
23.Kim, J.; Cote, L. J.; Huang, J., *Accounts of Chemical Research* **2012,** *45* (8), 1356-1364.
24.Zhu, Y.; Murali, S.; Cai, W.; Li, X.; Suk, J. W.; Potts, J. R.; Ruoff, R. S., *Advanced Materials* **2010,** *22* (35), 3906-3924.
25.Kuila, T.; Mishra, A. K.; Khanra, P.; Kim, N. H.; Lee, J. H., *Nanoscale* **2013,** *5* (1), 52-71.
26.Dimiev, A. M.; Tour, J. M., *ACS Nano* **2014,** *8* (3), 3060-3068.
27.Gómez-Navarro, C.; Weitz, R. T.; Bittner, A. M.; Scolari, M.; Mews, A.; Burghard, M.; Kern, K., *Nano Letters* **2007,** *7* (11), 3499-3503.
28.Dreyer, D. R.; Park, S.; Bielawski, C. W.; Ruoff, R. S., *Chemical Society Reviews* **2010,** *39* (1), 228-240.
29.Zhu, Y.; James, D. K.; Tour, J. M., *Advanced Materials* **2012,** *24* (36), 4924-4955.
30.Baughman, R. H.; Zakhidov, A. A.; de Heer, W. A., *Science* **2002,** *297* (5582), 787-792.
31.Imran Jafri, R.; Rajalakshmi, N.; Ramaprabhu, S., *Journal of Materials Chemistry* **2010,** *20* (34), 7114-7117.
32.Gao, M.-R.; Cao, X.; Gao, Q.; Xu, Y.-F.; Zheng, Y.-R.; Jiang, J.; Yu, S.-H., *ACS Nano* **2014,** *8* (4), 3970-3978.
33.Higgins, D. C.; Meza, D.; Chen, Z., *The Journal of Physical Chemistry C* **2010,** *114* (50), 21982-21988.
34.Stephan, O.; Ajayan, P. M.; Colliex, C.; Redlich, P.; Lambert, J. M.; Bernier, P.; Lefin, P., *Science* **1994,** *266* (5191), 1683-1685.
35.Terrones, M.; Ajayan, P. M.; Banhart, F.; Blase, X.; Carroll, D. L.; Charlier, J. C.; Czerw, R.; Foley, B.; Grobert, N.; Kamalakaran, R.; Kohler-Redlich, P.; Rühle, M.; Seeger, T.; Terrones, H., *Appl Phys A* **2002,** *74* (3), 355-361.
36.Kudashov, A. G.; Okotrub, A. V.; Bulusheva, L. G.; Asanov, I. P.; Shubin, Y. V.; Yudanov, N. F.; Yudanova, L. I.; Danilovich, V. S.; Abrosimov, O. G., *The Journal of Physical Chemistry B* **2004,** *108* (26), 9048-9053.
37.Choi, H. C.; Park, J.; Kim, B., *The Journal of Physical Chemistry B* **2005,** *109* (10), 4333-4340.
38.Wang, H.; Maiyalagan, T.; Wang, X., *ACS Catalysis* **2012,** *2* (5), 781-794.
39.Pels, J. R.; Kapteijn, F.; Moulijn, J. A.; Zhu, Q.; Thomas, K. M., *Carbon* **1995,** *33* (11), 1641-1653.
40.van Dommele, S.; Romero-Izquirdo, A.; Brydson, R.; de Jong, K. P.; Bitter, J. H., *Carbon* **2008,** *46* (1), 138-148.
41.Srivastava, D.; Menon, M.; Daraio, C.; Jin, S.; Sadanadan, B.; Rao, A. M., *Physical Review B* **2004,** *69* (15), 153414.
42.Feng, L.; Yang, L.; Huang, Z.; Luo, J.; Li, M.; Wang, D.; Chen, Y., *Sci. Rep.* **2013,** *3*.

43.Lu, A.-H.; Hao, G.-P.; Sun, Q.; Zhang, X.-Q.; Li, W.-C., *Macromolecular Chemistry and Physics* **2012,** *213* (10-11), 1107-1131.
44.Yoshinori, A.; Sumio, I., *Japanese Journal of Applied Physics* **1993,** *32* (1A), L107.
45.Szabó, A.; Perri, C.; Csató, A.; Giordano, G.; Vuono, D.; Nagy, J. B., *Materials* **2010,** *3* (5), 3092-3140.
46.Zhao, N.; He, C.; Jiang, Z.; Li, J.; Li, Y., *Materials Letters* **2006,** *60* (2), 159-163.
47.Chen, X.; Wang, R.; Xu, J.; Yu, D., *Micron* **2004,** *35* (6), 455-460.
48.Robertson, J., *Journal of nanoscience and nanotechnology* **2008,** *8* (7), 6105-6111.
49.Barzegar, H. R.; Nitze, F.; Sharifi, T.; Ramstedt, M.; Tai, C. W.; Malolepszy, A.; Stobinski, L.; Wågberg, T., *The Journal of Physical Chemistry C* **2012,** *116* (22), 12232-12239.
50.Jourdain, V.; Bichara, C., *Carbon* **2013,** *58* (0), 2-39.
51.Liao, X. Z., *Applied Physics Letters* **2003,** *82*, 2694-2696.
52.Nxumalo, E. N.; Coville, N. J., *Materials* **2010,** *3* (3), 2141-2171.
53.Huang, J.-Q.; Zhao, M.-Q.; Zhang, Q.; Nie, J.-Q.; Yao, L.-D.; Su, D. S.; Wei, F., *Catalysis Today* **2012,** *186* (1), 83-92.
54.Ruoff, R., *Nat Nano* **2008,** *3* (1), 10-11.
55.Schniepp, H. C.; Li, J.-L.; McAllister, M. J.; Sai, H.; Herrera-Alonso, M.; Adamson, D. H.; Prud'homme, R. K.; Car, R.; Saville, D. A.; Aksay, I. A., *The Journal of Physical Chemistry B* **2006,** *110* (17), 8535-8539.
56.Niyogi, S.; Bekyarova, E.; Itkis, M. E.; McWilliams, J. L.; Hamon, M. A.; Haddon, R. C., *Journal of the American Chemical Society* **2006,** *128* (24), 7720-7721.
57.Stankovich, S.; Piner, R. D.; Chen, X.; Wu, N.; Nguyen, S. T.; Ruoff, R. S., *Journal of Materials Chemistry* **2006,** *16* (2), 155-158.
58.Hummers, W. S.; Offeman, R. E., *Journal of the American Chemical Society* **1958,** *80* (6), 1339-1339.
59.Hontoria-Lucas, C.; López-Peinado, A. J.; López-González, J. d. D.; Rojas-Cervantes, M. L.; Martín-Aranda, R. M., *Carbon* **1995,** *33* (11), 1585-1592.
60.Si, Y.; Samulski, E. T., *Nano Letters* **2008,** *8* (6), 1679-1682.
61.Stankovich, S.; Dikin, D. A.; Piner, R. D.; Kohlhaas, K. A.; Kleinhammes, A.; Jia, Y.; Wu, Y.; Nguyen, S. T.; Ruoff, R. S., *Carbon* **2007,** *45* (7), 1558-1565.
62.Chakraborty, S.; Guo, W.; Hauge, R. H.; Billups, W. E., *Chemistry of Materials* **2008,** *20* (9), 3134-3136.
63.Sun, H.; Wang, Y.; Liu, S.; Ge, L.; Wang, L.; Zhu, Z.; Wang, S., *Chemical Communications* **2013,** *49* (85), 9914-9916.
64.Bag, S.; Roy, K.; Gopinath, C. S.; Raj, C. R., *ACS Applied Materials & Interfaces* **2014,** *6* (4), 2692-2699.

65.Li, X.; Wang, H.; Robinson, J. T.; Sanchez, H.; Diankov, G.; Dai, H., *Journal of the American Chemical Society* **2009,** *131* (43), 15939-15944.
66.Shi, W.; Rui, X.; Zhu, J.; Yan, Q., *The Journal of Physical Chemistry C* **2012,** *116* (51), 26685-26693.
67.Tuček, J.; Kemp, K. C.; Kim, K. S.; Zbořil, R., *ACS Nano* **2014,** *8* (8), 7571-7612.
68.Yan, Z.; Ma, L.; Zhu, Y.; Lahiri, I.; Hahm, M. G.; Liu, Z.; Yang, S.; Xiang, C.; Lu, W.; Peng, Z.; Sun, Z.; Kittrell, C.; Lou, J.; Choi, W.; Ajayan, P. M.; Tour, J. M., *ACS Nano* **2012,** *7* (1), 58-64.
69.Youn, D. H.; Jang, J.-W.; Kim, J. Y.; Jang, J. S.; Choi, S. H.; Lee, J. S., *Sci. Rep.* **2014,** *4*.
70.Mazloumi, M.; Shadmehr, S.; Rangom, Y.; Nazar, L. F.; Tang, X., *ACS Nano* **2013,** *7* (5), 4281-4288.
71.Xu, X.; Huang, D.; Cao, K.; Wang, M.; Zakeeruddin, S. M.; Grätzel, M., *Sci. Rep.* **2013,** *3*.
72.Zhang, W.-D.; Xu, B.; Jiang, L.-C., *Journal of Materials Chemistry* **2010,** *20* (31), 6383-6391.
73.Feng, B.; Wang, H.; Wang, D.; Yu, H.; Chu, Y.; Fang, H.-T., *Nanoscale* **2014**.
74.Cheng, Y.; Liu, C.; Cheng, H.-M.; Jiang, S. P., *ACS Applied Materials & Interfaces* **2014,** *6* (13), 10089-10098.
75.Artiles, M. S.; Rout, C. S.; Fisher, T. S., *Advanced Drug Delivery Reviews* **2011,** *63* (14–15), 1352-1360.
76.Wang, W.; Guo, S.; Lee, I.; Ahmed, K.; Zhong, J.; Favors, Z.; Zaera, F.; Ozkan, M.; Ozkan, C. S., *Sci. Rep.* **2014,** *4*.
77.Hu, G.; Nitze, F.; Gracia-Espino, E.; Ma, J.; Barzegar, H. R.; Sharifi, T.; Jia, X.; Shchukarev, A.; Lu, L.; Ma, C.; Yang, G.; Wågberg, T., *Nat Commun* **2014,** *5*.
78.Wang, Y.; Xing, G.; Han, Z. J.; Shi, Y.; Wong, J. I.; Huang, Z. X.; Ostrikov, K.; Yang, H. Y., *Nanoscale* **2014,** *6* (15), 8884-8890.
79.Chaikittisilp, W.; Torad, N. L.; Li, C.; Imura, M.; Suzuki, N.; Ishihara, S.; Ariga, K.; Yamauchi, Y., *Chemistry – A European Journal* **2014,** *20* (15), 4217-4221.
80.Gomez-Marin, A. M., *Beilstein journal of nanotechnology* **2013,** *4*, 956-967.
81.Lim, D.-H.; Wilcox, J., *The Journal of Physical Chemistry C* **2012,** *116* (5), 3653-3660.
82.Song, C.; Tang, Y.; Zhang, J. L.; Zhang, J.; Wang, H.; Shen, J.; McDermid, S.; Li, J.; Kozak, P., *Electrochimica Acta* **2007,** *52* (7), 2552-2561.
83.Damjanovic, A., *Journal of Electroanalytical Chemistry* **1993,** *355* (1–2), 57-77.
84.Yeager, E., *Electrochimica Acta* **1984,** *29* (11), 1527-1537.

85.Suntivich, J.; Gasteiger, H. A.; Yabuuchi, N.; Nakanishi, H.; Goodenough, J. B.; Shao-Horn, Y., *Nat Chem* **2011,** *3* (7), 546-550.
86.Ishihara, A.; Yin, S.; Suito, K.; Uehara, N.; Okada, Y.; Kohno, Y.; Matsuzawa, K.; Mitsushima, S.; Chisaka, M.; Ohgi, Y.; Matsumoto, M.; Imai, H.; Ota, K.-i., *ECS Transactions* **2013,** *58* (1), 1495-1500.
87.Ishihara, A.; Ohgi, Y.; Matsuzawa, K.; Mitsushima, S.; Ota, K.-i., *Electrochimica Acta* **2010,** *55* (27), 8005-8012.
88.Yan, Z.; Zhang, M.; Xie, J.; Wang, H.; Wei, W., *Journal of Power Sources* **2013,** *243* (0), 48-53.
89.Kim, J.; Lee, S. W.; Carlton, C.; Shao-Horn, Y., *The Journal of Physical Chemistry Letters* **2011,** *2* (11), 1332-1336.
90.Hwang, S. J.; Kim, S.-K.; Lee, J.-G.; Lee, S.-C.; Jang, J. H.; Kim, P.; Lim, T.-H.; Sung, Y.-E.; Yoo, S. J., *Journal of the American Chemical Society* **2012,** *134* (48), 19508-19511.
91.Kariuki, N. N.; Khudhayer, W. J.; Karabacak, T.; Myers, D. J., *ACS Catalysis* **2013,** *3* (12), 3123-3132.
92.Wang, W.; Wang, R.; Ji, S.; Feng, H.; Wang, H.; Lei, Z., *Journal of Power Sources* **2010,** *195* (11), 3498-3503.
93.Zhang, L.; Iyyamperumal, R.; Yancey, D. F.; Crooks, R. M.; Henkelman, G., *ACS Nano* **2013,** *7* (10), 9168-9172.
94.Kongkanand, A.; Kuwabata, S., *The Journal of Physical Chemistry B* **2005,** *109* (49), 23190-23195.
95.Wei, W.; Tao, Y.; Lv, W.; Su, F.-Y.; Ke, L.; Li, J.; Wang, D.-W.; Li, B.; Kang, F.; Yang, Q.-H., *Sci. Rep.* **2014,** *4*.
96.Yang, Z.; Nie, H.; Chen, X. a.; Chen, X.; Huang, S., *Journal of Power Sources* **2013,** *236* (0), 238-249.
97.Liu, R.; Wu, D.; Feng, X.; Müllen, K., *Angewandte Chemie International Edition* **2010,** *49* (14), 2565-2569.
98.Xue, Y.; Yu, D.; Dai, L.; Wang, R.; Li, D.; Roy, A.; Lu, F.; Chen, H.; Liu, Y.; Qu, J., *Physical Chemistry Chemical Physics* **2013,** *15* (29), 12220-12226.
99.Wen, Q.; Wang, S.; Yan, J.; Cong, L.; Chen, Y.; Xi, H., *Bioelectrochemistry* **2014,** *95* (0), 23-28.
100.Liang, H.-W.; Zhuang, X.; Brüller, S.; Feng, X.; Müllen, K., *Nat Commun* **2014,** *5*.
101.Bouwkamp-Wijnoltz, A. L.; Visscher, W.; van Veen, J. A. R.; Tang, S. C., *Electrochimica Acta* **1999,** *45* (3), 379-386.
102.Wiesener, K., *Electrochimica Acta* **1986,** *31* (8), 1073-1078.
103.Jasinski, R., *Journal of The Electrochemical Society* **1965,** *112* (5), 526-528.
104.Chung, H. T.; Won, J. H.; Zelenay, P., *Nat Commun* **2013,** *4*, 1922.
105.Tang, C.; Zhang, Q.; Zhao, M.-Q.; Huang, J.-Q.; Cheng, X.-B.; Tian, G.-L.; Peng, H.-J.; Wei, F., *Advanced Materials* **2014,** *26* (35), 6100-6105.

106.Ayala, P.; Arenal, R.; Rümmeli, M.; Rubio, A.; Pichler, T., *Carbon* **2010,** *48* (3), 575-586.
107.Lv, R.; Li, Q.; Botello-Méndez, A. R.; Hayashi, T.; Wang, B.; Berkdemir, A.; Hao, Q.; Elías, A. L.; Cruz-Silva, R.; Gutiérrez, H. R.; Kim, Y. A.; Muramatsu, H.; Zhu, J.; Endo, M.; Terrones, H.; Charlier, J.-C.; Pan, M.; Terrones, M., *Sci. Rep.* **2012,** *2*.
108.Lazar, P.; Zboril, R.; Pumera, M.; Otyepka, M., *Physical Chemistry Chemical Physics* **2014,** *16* (27), 14231-14235.
109.Kim, H.; Lee, K.; Woo, S. I.; Jung, Y., *Physical Chemistry Chemical Physics* **2011,** *13* (39), 17505-17510.
110.Zhang, Y.; Ge, J.; Wang, L.; Wang, D.; Ding, F.; Tao, X.; Chen, W., *Sci. Rep.* **2013,** *3*.
111.Yu, L.; Pan, X.; Cao, X.; Hu, P.; Bao, X., *Journal of Catalysis* **2011,** *282* (1), 183-190.
112.Okamoto, Y., *Applied Surface Science* **2009,** *256* (1), 335-341.
113.Yuan, W.; Zhou, Y.; Li, Y.; Li, C.; Peng, H.; Zhang, J.; Liu, Z.; Dai, L.; Shi, G., *Sci. Rep.* **2013,** *3*.
114.Morcos, I.; Yeager, E., *Electrochimica Acta* **1970,** *15* (6), 953-975.
115.Bard, A. J.; Fox, M. A., *Accounts of Chemical Research* **1995,** *28* (3), 141-145.
116.Kanan, M. W.; Nocera, D. G., *Science* **2008,** *321* (5892), 1072-1075.
117.Ferreira, K. N.; Iverson, T. M.; Maghlaoui, K.; Barber, J.; Iwata, S., *Science* **2004,** *303* (5665), 1831-1838.
118.Fujishima, A.; Honda, K., *Nature* **1972,** *238* (5358), 37-38.
119.Khaselev, O.; Turner, J. A., *Science* **1998,** *280* (5362), 425-427.
120.Reece, S. Y.; Hamel, J. A.; Sung, K.; Jarvi, T. D.; Esswein, A. J.; Pijpers, J. J. H.; Nocera, D. G., *Science* **2011,** *334* (6056), 645-648.
121.Brillet, J.; Yum, J.-H.; Cornuz, M.; Hisatomi, T.; Solarska, R.; Augustynski, J.; Graetzel, M.; Sivula, K., *Nat Photon* **2012,** *6* (12), 824-828.
122.Pinaud, B. A.; Benck, J. D.; Seitz, L. C.; Forman, A. J.; Chen, Z.; Deutsch, T. G.; James, B. D.; Baum, K. N.; Baum, G. N.; Ardo, S.; Wang, H.; Miller, E.; Jaramillo, T. F., *Energy & Environmental Science* **2013,** *6* (7), 1983-2002.
123.Cook, T. R.; Dogutan, D. K.; Reece, S. Y.; Surendranath, Y.; Teets, T. S.; Nocera, D. G., *Chemical Reviews* **2010,** *110* (11), 6474-6502.
124.Zeng, K.; Zhang, D., *Progress in Energy and Combustion Science* **2010,** *36* (3), 307-326.
125.Rocheleau, R. E.; Miller, E. L.; Misra, A., *Energy & Fuels* **1998,** *12* (1), 3-10.
126.Jacobsson, T. J.; Fjallstrom, V.; Sahlberg, M.; Edoff, M.; Edvinsson, T., *Energy & Environmental Science* **2013,** *6* (12), 3676-3683.
127.Edri, E.; Kirmayer, S.; Cahen, D.; Hodes, G., *The Journal of Physical Chemistry Letters* **2013,** *4* (6), 897-902.

128.Fang, Y.-H.; Liu, Z.-P., *Journal of the American Chemical Society* **2010,** *132* (51), 18214-18222.
129.Bockris, J. O.; Otagawa, T., *The Journal of Physical Chemistry* **1983,** *87* (15), 2960-2971.
130.Reier, T.; Teschner, D.; Lunkenbein, T.; Bergmann, A.; Selve, S.; Kraehnert, R.; Schlögl, R.; Strasser, P., *Journal of The Electrochemical Society* **2014,** *161* (9), F876-F882.
131.Li, G.; Yu, H.; Wang, X.; Sun, S.; Li, Y.; Shao, Z.; Yi, B., *Physical Chemistry Chemical Physics* **2013,** *15* (8), 2858-2866.
132.Trotochaud, L.; Young, S. L.; Ranney, J. K.; Boettcher, S. W., *Journal of the American Chemical Society* **2014,** *136* (18), 6744-6753.
133.Gao, M.; Sheng, W.; Zhuang, Z.; Fang, Q.; Gu, S.; Jiang, J.; Yan, Y., *Journal of the American Chemical Society* **2014,** *136* (19), 7077-7084.
134.Cobo, S.; Heidkamp, J.; Jacques, P.-A.; Fize, J.; Fourmond, V.; Guetaz, L.; Jousselme, B.; Ivanova, V.; Dau, H.; Palacin, S.; Fontecave, M.; Artero, V., *Nat Mater* **2012,** *11* (9), 802-807.
135.Liu, Y.; Nocera, D. G., *The Journal of Physical Chemistry C* **2014,** *118* (30), 17060-17066.
136.Wang, Y.; Ding, W.; Chen, S.; Nie, Y.; Xiong, K.; Wei, Z., *Chemical Communications* **2014**.
137.Jin, K.; Park, J.; Lee, J.; Yang, K. D.; Pradhan, G. K.; Sim, U.; Jeong, D.; Jang, H. L.; Park, S.; Kim, D.; Sung, N.-E.; Kim, S. H.; Han, S.; Nam, K. T., *Journal of the American Chemical Society* **2014,** *136* (20), 7435-7443.
138.Gong, M.; Li, Y.; Wang, H.; Liang, Y.; Wu, J. Z.; Zhou, J.; Wang, J.; Regier, T.; Wei, F.; Dai, H., *Journal of the American Chemical Society* **2013,** *135* (23), 8452-8455.
139.Ma, T. Y.; Dai, S.; Jaroniec, M.; Qiao, S. Z., *Angewandte Chemie* **2014,** *126* (28), 7409-7413.
140.Tian, G.-L.; Zhao, M.-Q.; Yu, D.; Kong, X.-Y.; Huang, J.-Q.; Zhang, Q.; Wei, F., *Small* **2014,** *10* (11), 2251-2259.
141.Xin, S.; Guo, Y.-G.; Wan, L.-J., *Accounts of Chemical Research* **2012,** *45* (10), 1759-1769.
142.Wang, K.; Wu, H.; Meng, Y.; Wei, Z., *Small* **2014,** *10* (1), 14-31.
143.Shen, L.; Che, Q.; Li, H.; Zhang, X., *Advanced Functional Materials* **2014,** *24* (18), 2630-2637.
144.Jiang, J.; Li, Y.; Liu, J.; Huang, X.; Yuan, C.; Lou, X. W., *Advanced Materials* **2012,** *24* (38), 5166-5180.
145.Dong, C.-D.; Chen, C.-W.; Chen, C.-F.; Hung, C.-M., *Sci. Rep.* **2014,** *4*.
146.Liang, Y.; Li, Y.; Wang, H.; Zhou, J.; Wang, J.; Regier, T.; Dai, H., *Nat Mater* **2011,** *10* (10), 780-786.
147.Mao, S.; Wen, Z.; Huang, T.; Hou, Y.; Chen, J., *Energy & Environmental Science* **2014,** *7* (2), 609-616.

148.Ma, T. Y.; Dai, S.; Jaroniec, M.; Qiao, S. Z., *Journal of the American Chemical Society* **2014,** *136* (39), 13925-13931.
149.Li, M.; Zhang, L.; Xu, Q.; Niu, J.; Xia, Z., *Journal of Catalysis* **2014,** *314* (0), 66-72.
150.Zhao, Y.; Nakamura, R.; Kamiya, K.; Nakanishi, S.; Hashimoto, K., *Nat Commun* **2013,** *4*.
151.Wang, H.; Dai, H., *Chemical Society Reviews* **2013,** *42* (7), 3088-3113.
152.Gong, Y.; Yang, S.; Zhan, L.; Ma, L.; Vajtai, R.; Ajayan, P. M., *Advanced Functional Materials* **2014,** *24* (1), 125-130.
153.Vlad, A.; Singh, N.; Rolland, J.; Melinte, S.; Ajayan, P. M.; Gohy, J. F., *Sci. Rep.* **2014,** *4*.
154.Poizot, P.; Laruelle, S.; Grugeon, S.; Dupont, L.; Tarascon, J. M., *Nature* **2000,** *407* (6803), 496-499.
155.Dey, A. N., *Journal of The Electrochemical Society* **1971,** *118* (10), 1547-1549.
156.Huggins, R. A., *Journal of Power Sources* **1999,** *81–82* (0), 13-19.
157.Yoo, E.; Kim, J.; Hosono, E.; Zhou, H.-s.; Kudo, T.; Honma, I., *Nano Letters* **2008,** *8* (8), 2277-2282.
158.Ren, W.; Li, D.; Liu, H.; Mi, R.; Zhang, Y.; Dong, L., *Electrochimica Acta* **2013,** *105* (0), 75-82.
159.Li, X.; Liu, J.; Zhang, Y.; Li, Y.; Liu, H.; Meng, X.; Yang, J.; Geng, D.; Wang, D.; Li, R.; Sun, X., *Journal of Power Sources* **2012,** *197* (0), 238-245.
160.Shin, W. H.; Jeong, H. M.; Kim, B. G.; Kang, J. K.; Choi, J. W., *Nano Letters* **2012,** *12* (5), 2283-2288.
161.Jiang, K.; Eitan, A.; Schadler, L. S.; Ajayan, P. M.; Siegel, R. W.; Grobert, N.; Mayne, M.; Reyes-Reyes, M.; Terrones, H.; Terrones, M., *Nano Letters* **2003,** *3* (3), 275-277.
162.Gracia-Espino, E.; Jia, X.; Wågberg, T., *The Journal of Physical Chemistry C* **2014,** *118* (5), 2804-2811.
163.Balaya, P., *Energy and Environmental Science* **2008,** *1* (6), 645-654.
164.Ellis, B.; Subramanya Herle, P.; Rho, Y. H.; Nazar, L. F.; Dunlap, R.; Perry, L. K.; Ryan, D. H., *Faraday Discussions* **2007,** *134*, 119-141.
165.Nitze, F.; Andersson, B. M.; Wågberg, T., *physica status solidi (b)* **2009,** *246* (11-12), 2440-2443.
166.Sharifi, T.; Nitze, F.; Barzegar, H. R.; Tai, C.-W.; Mazurkiewicz, M.; Malolepszy, A.; Stobinski, L.; Wågberg, T., *Carbon* **2012,** *50* (10), 3535-3541.
167.Sharifi, T.; Valvo, M.; Gracia-Espino, E.; Sandström, R.; Edström, K.; Wågberg, T., *Journal of Power Sources* **2015,** *279* (0), 581-592.
168.GWON, Y.-H.; PENG, B.; CHOI, Y.-J.; HA, J.-H.; KIM, K.-W.; CHO, K.-K.; RYU, K.-S., THE EFFECTS OF TiO2 BUFFER LAYER IN CARBON NANOTUBES GROWTH ON Ti SUBSTRATE BY THERMAL CHEMICAL

VAPOR DEPOSITION AND THEIR ELECTROCHEMICAL PROPERTIES. In *Advanced Materials and Processing 2010*, pp 223-226.
169.Gwon, Y.; Ha, J.; Cho, K.; Kim, H., *Nanoscale Res Lett* **2012,** *7* (1), 1-5.
170.Lin, Z.; Song, M.-k.; Ding, Y.; Liu, Y.; Liu, M.; Wong, C.-p., *Physical Chemistry Chemical Physics* **2012,** *14* (10), 3381-3387.
171.He, C.; Zhao, N.; Shi, C.; Du, X.; Li, J., *Journal of Alloys and Compounds* **2007,** *433* (1–2), 79-83.
172.Zhu, J.; Jia, J.; Kwong, F.-l.; Ng, D. H. L., *Carbon* **2012,** *50* (7), 2504-2512.
173.Lu, Y.; Zhu, Z.; Su, D.; Wang, D.; Liu, Z.; Schlögl, R., *Carbon* **2004,** *42* (15), 3199-3207.
174.Ding, F.; Bolton, K.; Rosén, A., *Journal of Elec Materi* **2006,** *35* (2), 207-210.
175.Sharifi, T.; Hu, G.; Jia, X.; Wågberg, T., *ACS Nano* **2012,** *6* (10), 8904-8912.
176.Kundu, S.; Nagaiah, T. C.; Xia, W.; Wang, Y.; Dommele, S. V.; Bitter, J. H.; Santa, M.; Grundmeier, G.; Bron, M.; Schuhmann, W.; Muhler, M., *The Journal of Physical Chemistry C* **2009,** *113* (32), 14302-14310.
177.Rao, C. V.; Cabrera, C. R.; Ishikawa, Y., *The Journal of Physical Chemistry Letters* **2010,** *1* (18), 2622-2627.
178.Chen, Z.; Higgins, D.; Tao, H.; Hsu, R. S.; Chen, Z., *The Journal of Physical Chemistry C* **2009,** *113* (49), 21008-21013.
179.Maldonado, S.; Stevenson, K. J., *The Journal of Physical Chemistry B* **2005,** *109* (10), 4707-4716.
180.Biniak, S.; Szymański, G.; Siedlewski, J.; Świątkowski, A., *Carbon* **1997,** *35* (12), 1799-1810.
181.Casanovas, J.; Ricart, J. M.; Rubio, J.; Illas, F.; Jiménez-Mateos, J. M., *Journal of the American Chemical Society* **1996,** *118* (34), 8071-8076.
182.Maldonado, S.; Morin, S.; Stevenson, K. J., *Carbon* **2006,** *44* (8), 1429-1437.
183.Glerup, M.; Castignolles, M.; Holzinger, M.; Hug, G.; Loiseau, A.; Bernier, P., *Chemical Communications* **2003,** (20), 2542-2543.
184.Tuinstra, F.; Koenig, J. L., *The Journal of Chemical Physics* **1970,** *53* (3), 1126-1130.
185.Angoni, K., *Carbon* **1993,** *31* (4), 537-547.
186.Rouzaud, J. N.; Oberlin, A.; Beny-Bassez, C., *Comptes Rendus des Seances - Academie des Sciences, Serie II* **1983,** *296* (5), 369-372.
187.Sjöström, H.; Stafström, S.; Boman, M.; Sundgren, J. E., *Physical Review Letters* **1995,** *75* (7), 1336-1339.
188.Stańczyk, K.; Dziembaj, R.; Piwowarska, Z.; Witkowski, S., *Carbon* **1995,** *33* (10), 1383-1392.
189.Gong, K.; Du, F.; Xia, Z.; Durstock, M.; Dai, L., *Science* **2009,** *323* (5915), 760-764.

190.Li, H.; Liu, H.; Jong, Z.; Qu, W.; Geng, D.; Sun, X.; Wang, H., *International Journal of Hydrogen Energy* **2011,** *36* (3), 2258-2265.
191.Lai, L.; Potts, J. R.; Zhan, D.; Wang, L.; Poh, C. K.; Tang, C.; Gong, H.; Shen, Z.; Lin, J.; Ruoff, R. S., *Energy & Environmental Science* **2012,** *5* (7), 7936-7942.
192.Niwa, H.; Horiba, K.; Harada, Y.; Oshima, M.; Ikeda, T.; Terakura, K.; Ozaki, J.-i.; Miyata, S., *Journal of Power Sources* **2009,** *187* (1), 93-97.
193.Schaper, A. K.; Wang, M. S.; Xu, Z.; Bando, Y.; Golberg, D., *Nano Letters* **2011,** *11* (8), 3295-3300.
194.Chen, Y.; Lu, J.; Gao, Z., *The Journal of Physical Chemistry C* **2007,** *111* (4), 1625-1630.
195.Mpourmpakis, G.; Tylianakis, E.; Froudakis, G. E., *Nano Letters* **2007,** *7* (7), 1893-1897.
196.Zhao, J.; Yang, B.; Zheng, Z.; Yang, J.; Yang, Z.; Zhang, P.; Ren, W.; Yan, X., *ACS Applied Materials & Interfaces* **2014,** *6* (12), 9890-9896.
197.Sharifi, T.; Gracia-Espino, E.; Reza Barzegar, H.; Jia, X.; Nitze, F.; Hu, G.; Nordblad, P.; Tai, C.-W.; Wågberg, T., *Nat Commun* **2013,** *4*.
198.Jubb, A. M.; Allen, H. C., *ACS Applied Materials & Interfaces* **2010,** *2* (10), 2804-2812.
199.Oh, S.; Cook, D. C.; Townsend, H. E., *Hyperfine Interactions* **1998,** *112* (1-4), 59-66.
200.Bersani, D.; Lottici, P. P.; Montenero, A., *Journal of Raman Spectroscopy* **1999,** *30* (5), 355-360.
201.Santato, C.; Odziemkowski, M.; Ulmann, M.; Augustynski, J., *Journal of the American Chemical Society* **2001,** *123* (43), 10639-10649.
202.Tronc, E.; Prene, P.; Jolivet, J. P.; d'Orazio, F.; Lucari, F.; Fiorani, D.; Godinho, M.; Cherkaoui, R.; Nogues, M.; Dormann, J. L., *Hyperfine Interactions* **1995,** *95* (1), 129-148.
203.Zamudio, A.; Elías, A. L.; Rodríguez-Manzo, J. A.; López-Urías, F.; Rodríguez-Gattorno, G.; Lupo, F.; Rühle, M.; Smith, D. J.; Terrones, H.; Díaz, D.; Terrones, M., *Small* **2006,** *2* (3), 346-350.
204.Zhao, L.; He, R.; Rim, K. T.; Schiros, T.; Kim, K. S.; Zhou, H.; Gutiérrez, C.; Chockalingam, S. P.; Arguello, C. J.; Pálová, L.; Nordlund, D.; Hybertsen, M. S.; Reichman, D. R.; Heinz, T. F.; Kim, P.; Pinczuk, A.; Flynn, G. W.; Pasupathy, A. N., *Science* **2011,** *333* (6045), 999-1003.
205.Zhang, L.; Xia, Z., *The Journal of Physical Chemistry C* **2011,** *115* (22), 11170-11176.
206.Zheng, J.; Liu, H.; Wu, B.; Guo, Y.; Wu, T.; Yu, G.; Liu, Y.; Zhu, D., *Advanced Materials* **2011,** *23* (21), 2460-2463.
207.Machala, L.; Tuček, J.; Zbořil, R., *Chemistry of Materials* **2011,** *23* (14), 3255-3272.
208.Morales, J.; Sánchez, L.; Martín, F.; Berry, F.; Ren, X., *Journal of The Electrochemical Society* **2005,** *152* (9), A1748-A1754.

209.Valvo, M.; Lindgren, F.; Lafont, U.; Björefors, F.; Edström, K., *Journal of Power Sources* **2014,** *245* (0), 967-978.
210.Nordlinder, S.; Nyholm, L.; Gustafsson, T.; Edström, K., *Chemistry of Materials* **2005,** *18* (2), 495-503.
211.Hjelm, A.-K.; Lindbergh, G.; Lundqvist, A., *Journal of Electroanalytical Chemistry* **2001,** *509* (2), 139-147.
212.Jiang, S. P.; Tseung, A. C. C., *Journal of The Electrochemical Society* **1991,** *138* (5), 1216-1222.
213.Yongye, L.; Yanguang, L.; Hailiang, W.; Jigang, Z.; Jian, W.; Tom, R.; Hongjie, D., *Nature Materials* **2011,** *10* (10), 780-786.
214.Lyons, M. E. G.; Brandon, M. P., *J Electroanal Chem* **2010,** *641* (1-2), 119-130.
215.Kim, J. Y.; Magesh, G.; Youn, D. H.; Jang, J.-W.; Kubota, J.; Domen, K.; Lee, J. S., *Sci. Rep.* **2013,** *3*.
216.Bajdich, M.; García-Mota, M.; Vojvodic, A.; Nørskov, J. K.; Bell, A. T., *Journal of the American Chemical Society* **2013,** *135* (36), 13521-13530.
217.Zhang, M.; de Respinis, M.; Frei, H., *Nat Chem* **2014,** *6* (4), 362-367.
218.Chandrasekaran, S.; Choi, W. M.; Chung, J. S.; Hur, S. H.; Kim, E. J., *Materials Letters* **2014,** *136* (0), 118-121.
219.Mirkova, L.; Pashova, V. P.; Monev, M., *Meeting Abstracts* **2011,** *MA2011-01* (26), 1553.